

## ABSTRACT

Title of dissertation: **SHOCKS AND COLD FRONTS  
IN GALAXY CLUSTERS —  
PROBING THE MICROPHYSICS  
OF THE INTRACLUSTER MEDIUM**

**QIAN WANG**  
Doctor of Philosophy, 2019

Dissertation directed by: **Professor Richard Mushotzky**  
Department of Astronomy

Shocks and cold fronts in galaxy clusters, the largest gravitationally bound systems in the universe, are astrophysical laboratories where we can study the microphysics of the intracluster medium (ICM), a very hot ( $T \sim 10^7$ – $10^8$  K) plasma. Being the main baryon content of galaxy clusters, the ICM plays an important role in mediating the energy cascade from gravitational collapse during cosmological structure formation. It is also intricately linked to the evolution of the galaxies within. The scientific enquiries concerning the ICM range from fundamental physics questions to cosmological measurements.

In this dissertation, I demonstrate probing ICM microphysics by studying deep X-ray observations of two galaxy clusters, A520 and A2142. For A520, tests for thermal conduction, electron–ion equilibration timescale, and particle acceleration at the shock were carried out. For A2142, a test for the effective viscosity was performed using two apparent Kelvin-Helmholtz eddies along its southern cold front. Other interesting features were discovered and analyzed, such as a low gas fraction subcluster in the A520 outskirts, and X-ray deficient channels that could be plasma depletion sheets in both clusters.

SHOCKS AND COLD FRONTS IN GALAXY CLUSTERS  
— PROBING THE MICROPHYSICS OF THE  
INTRACLUSTER MEDIUM

by

Qian Wang

Dissertation submitted to the Faculty of the Graduate School of the  
University of Maryland, College Park in partial fulfillment  
of the requirements for the degree of  
Doctor of Philosophy  
2019

Advisory Committee:  
Professor Richard Mushotzky, Chair  
Professor James Drake  
Dr. Maxim Markevitch, Advisor  
Professor Massimo Ricotti  
Professor Sylvain Veilleux

© Copyright by  
Qian Wang  
2019

## Preface

This work mostly concerns the study of the hot thermal plasma — the intracluster medium — that fills the volume of galaxy clusters and accounts for most of its baryonic content. In particular, two merging clusters with very deep exposures, Abell 520 and Abell 2142, are examined in great detail, with emphasis on learning more about the microphysics of the intracluster medium at merger shocks and cold fronts. The merger of A520 is phenomenologically described in [Chapter 2](#), with an estimate of thermal conduction along its disrupted cool core remnant. Its famous bow shock is the focus of [Chapter 3](#), where a test of the electron–proton equilibration timescale is carried out by examining the post-shock electron temperature. In tandem with high angular resolution radio data, the origin of the radio edge coincident with the shock in the X-ray is also examined. The cold fronts of A2142 are studied in [Chapter 4](#), with an effort to constrain the ICM effective viscosity using the apparent large scale Kelvin-Helmholtz eddies along its southern cold front. In both clusters, there are curious quasi-linear narrow channels in the X-ray image that could be plasma depletion layers. Those three chapters have been accepted for publication (A520: [Wang et al. 2016, 2018](#); A2142: [Wang & Markevitch 2018](#)) and are reproduced here with minor reorganization of text and layout, and relabelling of certain self-references. [Chapter 1](#) amalgamates introductory texts from the aforementioned publications with some additional background information for the topics at large. In [Chapter 5](#), we present our temperature maps for three more clusters: A521, which is going through a major merger; A2319, which has a prominent cold front; and RX J1347, which has a sloshing cold front. Finally, a summary is given in [Chapter 6](#).

I am grateful to M. Markevitch, who taught me the ropes, whose insight and acumen have been indispensable. I also thank S. Giacintucci for reanalyzing the radio data of A520, on which the analysis of the radio edge of A520 in [§ 3.4.4](#) is based. The anonymous referees of the three publications that make up this thesis deserve credit for making this work better with their valuable criticism and useful comments. I want to thank R. Mushotzky for being supportive throughout my time in graduate school, from the time you took me on a mini-tour of the floor on my very first afternoon in the department. I am grateful to members of my committee J. Drake, M. Ricotti, and S. Veilleux for their valuable time reading this thesis and convening to question me in order to fulfil the requirements of my degree. I also thank C. Reynolds, who dutifully participated in committee meetings while still at UMD. I appreciate several members of the faculty offering to serve on the defense committee with short notice. I am glad to have met many people in the department, some who enriched my knowledge through teaching, some through serendipitous interactions, and my classmates in our shared class struggles. I thank M. Phillips, E. McKenzie, A. Newman, D. Kimbrell, and many department staff old and new with whom I may not have interacted personally, but would have helped me behind the scene; similarly I also thank the CRESST staff. I thank S. Kim at ISSS for your help over the years. Many people have kindly expended time and effort on me during my time in graduate school, helping me develop, if not this thesis, then intellectually and personally. I was supported by *Chandra* grants GO3-14144Z, GO5-16147Z, AR5-16013X, and GO8-19114.

I would not have made it this far without the support of T. Hung, whose intelligence I constantly benefit from, and whose guidance to my personal development merits a lengthy aside, but that would detract from the purpose of this document. Together with family and friends whom I hold close to heart, I am blessed to have you in my life. It is only for our privacy that I resist writing your name, but we both know.

*To my parents*

---

## Table of Contents

Preface	ii
List of Tables	viii
List of Figures	ix
List of Abbreviations	xi
1 Introduction	1
1.1 X-ray observations of the ICM with <i>Chandra</i>	2
1.2 Merger shocks	4
1.2.1 Electron–ion equilibration	9
1.2.2 Particle acceleration	11
1.3 Cold fronts	12
1.3.1 Thermal conductivity	14
1.3.2 Kelvin-Helmholtz instabilities and constraint on effective viscosity	16
1.3.3 Plasma depletion layer	17
1.4 Imaging analysis techniques	18
1.4.1 Images of X-ray surface brightness	18
1.4.2 Image reconstruction using wavelet decomposition	20
1.4.3 Temperature maps	21
1.4.4 Adaptive smoothing using variable-width Gaussian kernel	22
1.4.5 Wavelet reconstruction temperature maps	22
2 The merging galaxy cluster Abell 520	24
2.1 Introduction	25
2.2 X-ray data analysis	26
2.2.1 Sky background	31
2.2.2 Spectral analysis	33
2.3 Temperature maps	34
2.3.1 Smoothing with variable-width Gaussian kernel	34
2.3.2 Wavelet-smoothed temperature map	36
2.4 Results	37

2.4.1	Shock front (or fronts?) . . . . .	37
2.4.2	Break up of the cool core remnant . . . . .	38
2.4.3	Splashes, bumps and islands . . . . .	43
2.5	Discussion . . . . .	44
2.5.1	Scene of a ‘train wreck’ . . . . .	44
2.5.2	X-ray channel . . . . .	45
2.5.3	Dark subclusters in the northeast . . . . .	48
2.5.3.1	Specific entropy of the clump . . . . .	51
2.5.3.2	Total mass of the “dark clump” and its possible origin . . . . .	55
2.5.4	Constraints on thermal conduction . . . . .	59
2.6	Summary . . . . .	63
3	The bow shock and radio halo in Abell 520 . . . . .	66
3.1	Introduction . . . . .	67
3.2	X-ray data analysis . . . . .	68
3.3	Radio data analysis . . . . .	69
3.4	Discussion . . . . .	73
3.4.1	Bow shock . . . . .	73
3.4.2	Electron–ion equilibration timescale . . . . .	77
3.4.2.1	Geometrical systematic uncertainty . . . . .	85
3.4.2.2	Comparison with other shocks . . . . .	87
3.4.3	Radio halo features . . . . .	88
3.4.4	Origin of the radio edge . . . . .	89
3.4.4.1	Modeling radio emissivity profile . . . . .	91
3.4.4.2	Comparison with adiabatic compression . . . . .	95
3.5	Summary . . . . .	97
4	Deep X-ray look at Abell 2142 . . . . .	101
4.1	Introduction . . . . .	102
4.2	X-ray data analysis . . . . .	103
4.2.1	Temperature map of the small-scale structure . . . . .	106
4.3	Cold fronts . . . . .	108
4.3.1	Southern front . . . . .	109
4.3.2	Gas velocity at the southern front . . . . .	114
4.3.3	The displaced gas peak and the inner front . . . . .	116
4.3.4	Northwest front . . . . .	120
4.4	Constraints on plasma viscosity . . . . .	122
4.5	X-ray channel . . . . .	129
4.6	Summary . . . . .	133
5	Temperature maps of Abell 521, Abell 2319, and RX J1347 . . . . .	137
5.1	Abell 521 . . . . .	137
5.2	Abell 2319 . . . . .	140
5.3	RX J1347 . . . . .	142

6 Summary	145
Bibliography	149

---

## List of Tables

2.1	Thermal conduction timescale estimates using adjacent pieces of the stripped cool core remnant in A520. . . . .	62
3.1	Details of archival <i>VLA</i> observations of A520 . . . . .	70
3.2	Details of X-ray modeling of shock sectors . . . . .	78
4.1	Best fit model parameters for the southern and northwestern cold fronts of A2142 . . . . .	113

---

## List of Figures

1.1	X-ray surface brightness image of 1E 0657, the “Bullet” cluster . . . . .	6
1.2	Composite of the Bullet cluster overlaying X-ray and weak lensing mass surface density on optical image . . . . .	6
1.3	Magnetic draping in front of a cold front in simulations . . . . .	19
1.4	A plasma depletion region inside a simulated sloshing cold front . . . . .	19
2.1	The dark matter distribution in A520 from study of weak lensing surface density . . . . .	27
2.2	<i>Chandra</i> 0.8–4 keV surface brightness images of A520 (4 panels) . . . . .	28
2.2	— <i>continued</i> . . . . .	29
2.3	Temperature maps of A520 (2 panels) . . . . .	35
2.4	Zooming in X-ray image and temperature map of the stripped cool core remnant (2 panels) . . . . .	40
2.5	Spectral fitting regions and plots of measured projected temperatures (2 panels) . . . . .	41
2.6	X-ray brightness and temperature profile across the channel . . . . .	49
2.7	X-ray image of the tail clump with lensing mass contours overlaid . . . . .	52
2.8	Surface brightness profile across the cool trail just above the foot . . . . .	62
3.1	Plot showing coverage of the $uv$ plane of spatial frequencies by the four combined <i>VLA</i> datasets . . . . .	72
3.2	1.4 GHz image of the radio halo before and after the removal of unrelated sources (2 panels) . . . . .	74
3.3	<i>Chandra</i> 0.8–4 keV image showing the sectors in which the shock was modelled, and a plot of the best-fit model in the bow of the shock (2 panels) . . . . .	76
3.4	Plot of deprojected post-shock temperatures compared with model profiles in the central sector of the shock . . . . .	82
3.5	Plots of projected temperatures across the shock compared with model profiles in the off-center sectors (3 panels) . . . . .	83
3.6	X-ray image with radio contours overlaid, and a plot of the radio brightness profile across the shock (2 panels) . . . . .	90
4.1	0.8–4 keV X-ray surface brightness of A2142 . . . . .	107

4.2	Temperature map and X-ray surface brightness image of the inner region of A2142 showing its inner and southern cold fronts (2 panels) . . . . .	110
4.2	— <i>continued.</i> X-ray surface brightness profiles of the southern and inner cold fronts (2 panels) . . . . .	111
4.3	Residual X-ray emission after subtracting the inner cold front by wavelet decomposition, overlaying its contours on an optical image of the same region (2 panels) . . . . .	118
4.4	X-ray surface brightness image of the northwest cold front and a plot of its radial profile (2 panels) . . . . .	121
4.5	Enhanced images showing the southern cold front using wavelet decomposition and unsharpmasking (2 panels) . . . . .	123
4.6	KH eddies in simulations with Spitzer viscosity . . . . .	126
4.7	X-ray image of the channel extending from the southern cold front, and a plot of surface brightness profile across it (2 panels) . . . . .	130
5.1	<i>Chandra</i> X-ray image and temperature map of A521 (4 panels) . . . . .	139
5.2	<i>Chandra</i> X-ray image and temperature map of A2319 (2 panels) . . . . .	141
5.3	<i>Chandra</i> X-ray image, temperature map, and optical composite image of RXJ1347 (3 panels) . . . . .	144

---

## List of Abbreviations

ACIS	Advanced CCD Imaging Spectrometer ( <i>Chandra</i> instrument)
AGN	active galactic nucleus
ARF	auxiliary response file ( <i>Chandra</i> spectral analysis product)
BCG	brightest cluster galaxy
BI	back-illuminated (CCD chip)
CCD	charge-coupled device
<i>Chandra</i>	Chandra X-ray Observatory
FI	front-illuminated (CCD chip)
FOV	field of view
GMRT	Giant Metrewave Radio Telescope
HST	Hubble Space Telescope
ICM	intracluster medium
KH	Kelvin-Helmholtz
KHI	Kelvin-Helmholtz instability
LAB	Leiden/Argentine/Bonn (Survey)
LOFAR	the Low-Frequency Array radio telescope network
l.o.s.	line-of-sight
MHD	magnetohydrodynamics
PDL	plasma depletion layer
PHA	pulse height amplitude ( <i>Chandra</i> spectral analysis product)
RMF	redistribution matrix file ( <i>Chandra</i> spectral analysis product)
<i>Subaru</i>	Subaru Telescope
VLA	Very Large Array radio telescopes
XRISM	X-Ray Imaging and Spectroscopy Mission (formerly XARM)

# CHAPTER 1

---

## Introduction

Galaxy clusters are the largest gravitationally bound structures in the universe. A typical cluster contains hundreds to thousands of galaxies in a volume that is a few megaparsecs across. It had long been known that cluster galaxies were moving too fast and that some yet unobserved mass was causing them to remain bound. Only in the early 1970's, with the *Uhuru* satellite, was the extended X-ray emission of the ICM discovered (Gursky et al. 1971; Forman et al. 1972; Kellogg et al. 1972). Now we know that most of the baryonic mass within the cluster is in the form of hot ( $T \sim 10^7$ – $10^8$  K or 1–10 keV) and tenuous ( $n \sim 10^{-5}$  in the outskirts rising to as high as  $\sim 10^{-2}$  cm $^{-3}$  in the central region) fully ionized gas, the intracluster medium (ICM). This is in turn dwarfed by non-luminous “dark matter”, of which there is an order of magnitude more mass.

Galaxy clusters form and grow via mergers of less massive systems in a hierarchical process governed by gravity (e.g., Press & Schechter 1974; Springel et al. 2006). In the course of each merger, approximately speaking, the kinetic energy carried by the gas of the colliding clusters dissipates into thermal energy via shocks and turbulence and, in the absence of further disturbances, the hotter gas comes into approximate hydrostatic equi-

librium with the deeper gravitational potential of the resulting bigger cluster (e.g., [Bahcall & Sarazin 1977](#)) on a  $\sim$ Gyr timescale. What happens during that Gigayear of violent gas motions is very interesting, because it can illuminate several aspects of the physics of the intracluster plasma (e.g., [Markevitch & Vikhlinin 2007](#)). Ram pressure of the gas flows may strip the subclusters of their gas (e.g., [Clowe et al. 2006](#)) and disturb and even destroy their cool cores either directly (e.g., [Fabian & Daines 1991](#); [Markevitch et al. 2000](#)) or by facilitating mixing with the surrounding gas ([ZuHone et al. 2010](#)). Temperature gradients in the gas generated by shock heating and mixing of different gas phases should be quickly erased by thermal conduction, if it is not suppressed (e.g., [Markevitch et al. 2003b](#); [Eckert et al. 2012](#)). All of this makes observations of merging clusters in the X-ray, where we can map the density and temperature of the hot intracluster plasma, extremely interesting.

## **1.1 X-ray observations of the ICM with *Chandra***

The Chandra X-ray Observatory was launched in July 1999, and is operated by the Smithsonian Astrophysical Observatory at the Chandra X-ray Center. Now well beyond its design lifetime of 5 years, it continues to operate as the highest resolution imaging facility for X-ray astronomy. One of the onboard instruments, the Advanced CCD Imaging Spectrometer (ACIS), simultaneously records high-resolution images with medium-resolution spectra by measuring both position and energy of incoming photons. This makes it very suitable for studying the extended ICM, where we are interested in the spatial variations of both gas density and temperature across the cluster.

The ACIS instrument is an array of 10 CCD chips, comprised of two adjacent arrangements of a 2×2 array and a strip of 6 chips. Each CCD covers 8.4 by 8.4 arcmin of sky with a platescale of 0.492'' per pixel. The configuration for a typical galaxy cluster observation has 5 chips turned on, with a FOV of approximately 17 arcmin in extent. The angular resolution of the telescope is dependent on the photon energy and the off-axis angle from the optical axis. At 1.5 keV, this is approximately 1'' on-axis, increasing to approximately 12'' when a source is 10 arcminutes off-axis. This leads to images of clusters having point sources with different apparent sizes, for example later in [Fig. 2.2a](#) and [Fig. 4.1](#).

The ICM radiates in the X-ray predominantly via thermal bremsstrahlung. By measuring the continuum spectrum using *Chandra*, we can derive its gas density and temperature. The plasma emissivity depends on the density and temperature as (e.g. [Sarazin 1988](#))

$$\epsilon_{ff} \propto n_e n_i T_e^{-1/2}, \quad (1.1)$$

where  $n_i$  and  $n_e$  are the number densities of the ions and electrons,  $T_e$  is the electron temperature, and  $E$  is the photon energy. The combination of mirror effective area and instrument quantum efficiency results in *Chandra* being most sensitive in the 0.5–2 keV range, and the photon count rate depends mostly on just the density with only a few percent variation due to temperature. Together with geometry assumptions for the underlying gas distribution, they form the basis with which we derive densities from broadband flux measurements. The shape of the spectrum tells us the temperature and chemical abundance.

Since the launch of the Chandra Space Observatory two decades ago, our picture of the ICM has been greatly refined. Thanks to its ability to resolve  $1''$ , distinctly hydrodynamic phenomena are revealed with remarkable detail. The Advanced CCD Imaging Spectrometer (ACIS) instrument records both the position and energy of incoming photons, so we perform both an imaging and a spectral analysis of the extended ICM. The dominance of the peak in effective area in the soft band limits the range of temperatures for which we can derive tight constraints to  $\sim 1\text{--}10$  keV. Fortunately, the ICM in the central regions of most clusters is in this range of temperatures.

The remainder of this chapter outlines some of the ICM physics tests that can be done by examining galaxy clusters in the X-ray, with a focus on merger shocks and cold fronts.

## 1.2 Merger shocks

Shocks in the ICM can be found in three different phenomena. In the central regions of clusters ( $<1$  Mpc), active galactic nuclei can inject relativistic and very hot thermal plasma into their surroundings, resulting in shocks where this pushes into the ambient ICM. These are weak shocks ( $M \sim 1$ ) that have low density contrast, situated in an environment of messy hydrodynamic phenomena, making it very difficult to derive density and temperature profiles. Several megaparsecs from the cluster center in the far outskirts, there are accretion shocks as cool intergalactic gas from the cosmic voids fall into the cluster potential. These are very strong shocks ( $M \sim 10\text{--}100$ ), but the density there is so low that observing them in the X-ray is beyond current capabilities. The shocks that

this work is concerned with are those that result from a third kind, encounters between subclusters.

In a merger, the dark matter halos of the subclusters fly by with no other interactions beside gravity. The galaxies behave like particles and also move with the subcluster halos. However, the ICM component of the subclusters undergo hydrodynamic interactions. This is best illustrated with the quintessential cluster shock, that of 1E 0657 in [Fig. 1.1](#) (the “Bullet” cluster, [Markevitch et al. 2005](#)). In this merger along the E-W direction, a bow shock has formed in front of the core of the subcluster heading west. The dark matter halos, inferred from both the surface brightness of galaxy light and weak lensing, have moved on ([Fig. 1.2](#)) while the ICM lags. As they rushed into each other’s ICM atmospheres, ram pressure peeled away at the increasingly dense gas. The “bullet” that we see is a survivor of this process. It is the remnant of the denser core of the two, and had gone through the infalling subcluster’s less dense core, which was completely disrupted in the process.

In A520 we find a less symmetric core remnant, presenting a more advanced showcase ([Fig. 2.2a](#)). Here the merger happened along the NE-SW direction. The prominent bow shock can be seen just ahead of the cool core remnant. In both 1E 0657 and A520, the subcluster halo had moved beyond the cool core altogether, and the configuration is then Rayleigh-Taylor unstable ([Fig. 2.2c](#) overlays A520 with contours of lensing mass map, and the red cross marks the BCG, most likely coincident with the center of the subcluster’s mass). A520 shows the next stage where the densest part of the core has broken out and is heading towards the subcluster center, leaving a trail of cool gas very likely still connected via stretched magnetic fields.

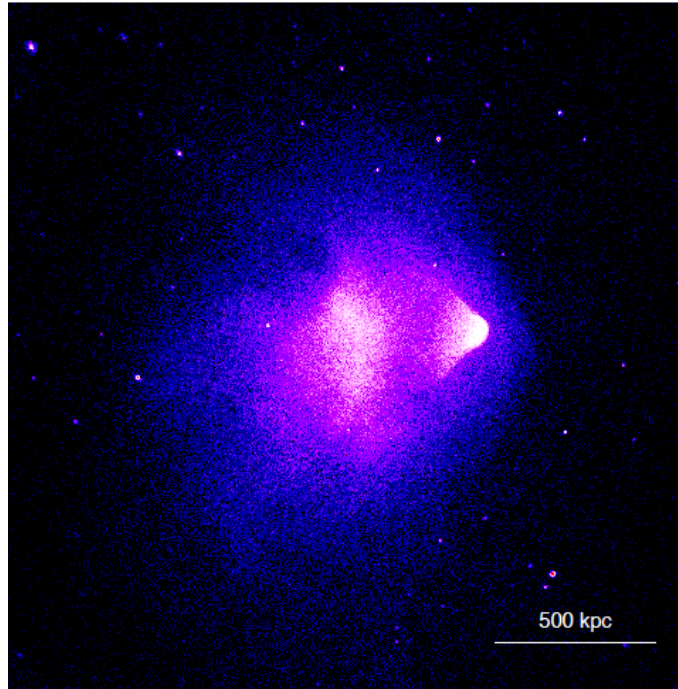


Figure 1.1: X-ray surface brightness image of 1E 0657, the “Bullet” cluster. (From Fig. 1 of [Markevitch & Vikhlinin 2007](#).)

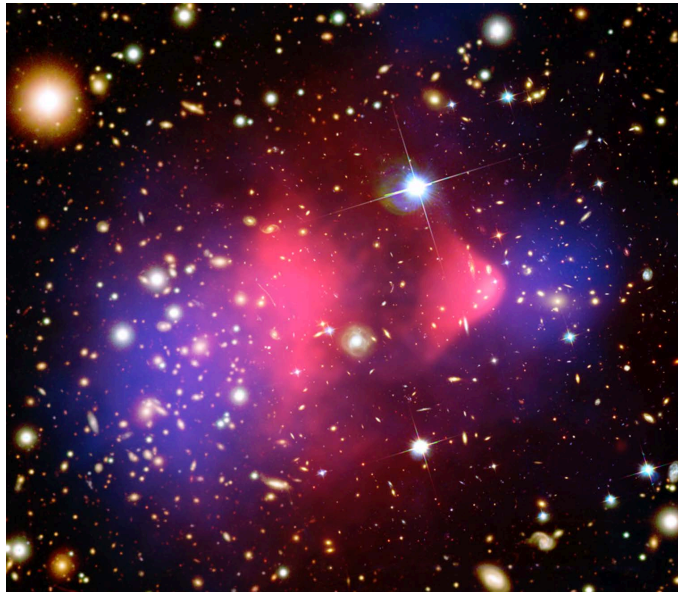


Figure 1.2: X-ray surface brightness (red) and lensing mass map (blue) overlaid on optical image. The colliding ICM lag behind the mass clumps of the subclusters. (X-ray: NASA/CXC/CfA/M.Markevitch et al.; Optical: NASA/STScI; Magellan/U.Arizona/D.Clowe et al.; Lensing Map: NASA/STScI; ESO WFI; Magellan/U.Arizona/D.Clowe et al.)

The Rankine-Hugoniot jump conditions apply across the shock. For a plane-parallel shock, three equations specify the conservation of mass, momentum, and energy, respectively:

$$\rho_1 u_1 = \rho_2 u_2, \quad (1.2)$$

$$P_1 + \rho_1 u_1^2 = P_2 + \rho_2 u_2^2, \quad (1.3)$$

$$\frac{1}{2} u_1^2 + \frac{\gamma_1}{\gamma_1 - 1} \frac{P_1}{\rho_1} = \frac{1}{2} u_2^2 + \frac{\gamma_2}{\gamma_2 - 1} \frac{P_2}{\rho_2}. \quad (1.4)$$

$P$ ,  $\rho$ , and  $u$  are gas pressure, density, and flow velocity in the shock rest frame, respectively, with the subscripts 1 and 2 denoting their upstream and downstream values. For merger shocks we assume  $\gamma = 5/3$  for monatomic gas and is the same on both sides of the shock.

The Mach number of the shock is defined as the ratio of flow velocity to the sound speed. In this work, we refer exclusively to the upstream Mach number, i.e.

$$M \equiv u_1/c_1, \quad (1.5)$$

where  $c_1$  is the sound speed, given by

$$c^2 = \gamma P/\rho = \gamma k_B T. \quad (1.6)$$

From the jump conditions, we can derive the shock Mach number from either the

density jump (to obtain Eq. 3.1 in § 3.4.1) or the temperature jump (if we invert Eq. 3.1 and substitute  $M$  for  $x$  in Eq. 3.3, in § 3.4.2). However, in practice the latter is less viable because while *Chandra* can constrain density very well (since the soft X-ray emissivity is a good proxy), it cannot do the same for temperatures above the peak in mirror effective area at around 2 keV. For moderate shocks, such as those expected of merger shocks in the denser central parts of clusters, there is a density contrast of 2–3 that is easily discernable in the X-ray surface brightness profile. For strong shocks, the density jump tends to an asymptotic value (for monatomic gas with  $\gamma = 5/3$ , this is 4), in which case the shock Mach number must be derived using the temperature jump instead. Such strong shocks are expected to be found further from the cluster center where the upstream ICM is cooler, but this also reduces the likelihood of observing them in the X-rays because of the lower gas density, therefore X-ray surface brightness. In § 3.4.1, we model the bow shock of A520 ( $M = 2.4$  with a density contrast of 2.6) in detail to derive its properties.

For the tests that we seek, the main hurdle is the rarity of the occurrence of well-shaped bow shocks such as that seen in the Bullet cluster and A520. Not only are they rare due to the relatively short timescale of this merger stage, they must also be oriented in just the right viewing direction to see the strongest part of the shock edge-on. Thus far, only a handful of shock fronts with clear geometry have been found and studied in the X-ray (e.g., Bullet, Markevitch et al. 2002; A520, Markevitch et al. 2005; A2146, Russell et al. 2010; A754, Macario et al. 2011; A521, Bourdin et al. 2013; A2034, Owers et al. 2014; RX J0751.3+5012, Russell et al. 2014; A665, Dasadia et al. 2016a; RX J0334.2–0111, Dasadia et al. 2016b). Among these, only Bullet cluster and A665 have high Mach numbers  $M \sim 3$ , and A520, A521, and A2146 have  $M \gtrsim 2$ .

### 1.2.1 Electron–ion equilibration

An interesting possibility to observe the process of energy equilibration of the plasma electrons and protons is afforded by shock fronts. In a simple picture, for shocks with low Mach numbers  $M$  typical for cluster mergers, the shock passage heats ions dissipatively, while electrons, whose thermal velocity is much higher than that of the shock, are only compressed adiabatically. They then equilibrate via Coulomb collisions with protons. If this indeed is how the electron temperature  $T_e$  behaves in clusters, this would have far-reaching consequences — for example, total mass estimates at large cluster radii, based on the hydrostatic assumption and the electron temperature (e.g., [Sarazin 1988](#)), would be biased low because of an underestimate of the average temperature in the low-density cluster outskirts (e.g., [Markevitch et al. 1996](#); [Takizawa 1999](#)). This effect has astrophysical implications far beyond galaxy clusters — e.g., certain models of accretion disks rely on the electron–ion equilibration timescale ([Rees et al. 1982](#)).

In the X-ray, we directly observe only the electron temperature  $T_e$ , but at an intracluster shock, we can deduce the equilibrium plasma temperature from the directly observable gas density jump, which gives the Mach number. Luckily, the cluster Mach numbers are low enough for the density jump to be far from its asymptotic value. We can then determine the gas flow velocities on both sides of the shock:  $u_1$  from  $M$  and upstream sound speed ([Eq. 1.5](#) and [Eq. 1.6](#)), and  $u_2$  by mass conservation at the density jump ([Eq. 1.2](#)). We are further lucky that the typical ICM densities and temperatures are such that the product of the Coulomb electron–proton equilibration timescale and the sound speed is of the order of tens of kiloparsecs, which is resolvable by *Chandra*. This allows

us to derive an electron temperature profile across the shock and see if it follows the prediction for collisional equilibration in the narrow zone downstream from the shock. This test has first been applied to the Bullet Cluster (Markevitch 2006, hereafter M06; see also Markevitch & Vikhlinin 2007, hereafter MV07), who obtained a tantalizing conclusion (though only at a 95% significance) that the equilibration timescale is much shorter than Coulomb. If seen systematically in other cluster shocks, this may suggest the presence of a faster equilibration mechanism in the hot magnetized ICM. While shock fronts are also observed in supernova remnants and even in situ in the solar wind, in these scenarios we may only observe out-of-equipartition *at the shock* (e.g., supernova remnants Ghavamian et al. 2007; solar wind Hull et al. 2001). In cluster shocks, because of the favorable combination of the linear scales and the Mach numbers (e.g., MV07) we may be able to directly observe the time evolution of electron temperature along the downstream flow, to study the electron–proton equilibration timescale.

An analysis of A520’s shock is presented in § 3.4.2, where the portion of the shock with the highest Mach number is modelled to derive the deprojected density and temperature profiles. We found that the electron temperature immediately behind the shock is higher than the adiabatic compression scenario at 95% confidence, suggesting that an equilibration mechanism that is faster than Coulomb collision is at work. Given the rarity of shocks that are seen from an optimal viewing angle like the ones in the Bullet cluster and A520, expanding the sample would require searching at higher redshifts using more sensitive instruments.

### 1.2.2 Particle acceleration

Cosmic rays are a non-thermal component of the ICM whose energy density is a small fraction of the thermal gas, but can substantially alter its physics. The ultrarelativistic electrons reveal themselves through synchrotron radio emission in the shape of radio halos and relics (e.g., [Markevitch et al. 2005](#); [Giacintucci et al. 2008](#); [van Weeren et al. 2010](#); [Feretti et al. 2012](#); [Brunetti & Jones 2014](#)). Some well-known sources of cosmic rays are supernovae, star formation, and AGNs. The hydrodynamic flows of the ICM are also thought to contribute significantly to particle acceleration. One mechanism is through shocks and turbulence generated by cluster mergers that would not only heat the intracluster gas, but also accelerate ultrarelativistic particles and amplify magnetic fields that coexist with the thermal plasma. The nature of the acceleration mechanism by merger shocks is not well-known.

Radio relics are elongated features seen in many clusters, and can sometimes be directly associated with a shock surface in the X-ray. There are several contributions to the radio brightness jump across the shock. Always present is adiabatic compression, which increases the electron density and also the magnetic field strength, thus directly increasing the intensity of the synchrotron emission. Another mechanism that should be present at the shock is first-order Fermi acceleration (also known as diffusive shock acceleration), which increases energy of the electrons. The candidates for acceleration are thermal electrons, and pre-existing “fossil” relativistic electrons that have cooled too much to be seen by radio telescopes (synchrotron cooling time is  $\sim 10^8$  yr at this energy, shorter than the merger timescale). The fossil electrons could have originated from any of the

sources of ultrarelativistic electrons mentioned earlier, or perhaps even from the thermal population through multiple encounters with shocks and turbulence. All the effects may be present and it is unclear which is more significant. For adiabatic compression and re-acceleration of fossil electrons, there should be some radio emission in the pre-shock region that is some factors lower than in the post-shock region that can be estimated from theory. If significant amount of electrons could be accelerated from the thermal pool, then there need not be much fossil electrons present in the pre-shock region, so there would be no lower limit on the level of pre-shock radio emission.

In § 3.4.4, such a test is performed for the A520 shock. There is a coincidence of the shock in the X-ray and the radio relic associated with it along a wide section of the shock. With a reanalysis of VLA 1.4 GHz data, we were very close to ruling out the adiabatic compression-only scenario, thereby demonstrating the presence of particle acceleration or re-acceleration at shocks. We concluded that this interesting test is within reach using observations with better interferometric coverage and at lower frequencies, such as with GMRT or LOFAR.

### **1.3 Cold fronts**

The phenomenon known as a “cold front” was first discovered with *Chandra* data in the galaxy clusters A2142 (Markevitch et al. 2000) and A3667 (Vikhlinin et al. 2001a,b). Cold fronts are contact discontinuities in the density and temperature of the intracluster gas, seen in the sky plane as sharp edges (discontinuities of the gradient) of the X-ray brightness, usually unresolved even with the *Chandra* angular resolution (for a review

see [Markevitch & Vikhlinin 2007](#), hereafter MV07). Cold fronts may look similar to shocks in cluster X-ray images, but the gas temperature jump has the opposite sign — in the cold front, the temperature is lower on the denser side, so the two sides are near (though not exactly in) pressure equilibrium. The high-contrast edge of the gas “bullet” in the Bullet cluster in [Fig. 1.1](#) is a cold front. Unlike in shock fronts, there is no flow of gas across the cold front, but there is often a shear velocity at the cold front arising from the cold front having a different tangential motion than the gas outside.

Cold fronts can form during a merger as a result of ram pressure stripping of the infalling subcluster (the original proposal for A2142 in [Markevitch et al. 2000](#)). Clear examples of such fronts are the Bullet subcluster ([Markevitch et al. 2002](#)) and the infalling galaxy NGC 1404 ([Machacek et al. 2005](#); [Su et al. 2017](#)). Another class of cold fronts is observed in or near most cool cores, often as multiple concentric edges in a spiral pattern. These edges are caused by an off-axis subcluster merger and the resulting displacement of the dense core gas from the minimum of the gravitational potential, which sets off long-lasting sloshing of that gas in the potential well ([Markevitch et al. 2001](#); [Ascasibar & Markevitch 2006](#), hereafter A06; [MV07](#)). Such fronts are found in most cool cores ([Ghizzardi et al. 2010](#)), even in otherwise relaxed clusters; examples are RXJ1720.1+26 ([Mazzotta et al. 2001](#)), A2029 ([Clarke et al. 2004](#)), Ophiuchus ([A06](#); [Million et al. 2010](#); [ZuHone et al. 2010](#); [Werner et al. 2016b](#)), A496 ([Dupke et al. 2007](#)), Perseus ([Churazov et al. 2003](#); [Simionescu et al. 2012](#)), Virgo ([Simionescu et al. 2010](#); [Roediger et al. 2011](#); [Werner et al. 2016a](#)), and, as we now believe ([Tittley & Henriksen 2005](#); [MV07](#)), A2142.

Both types of cold fronts can be used for interesting tests of the microphysics of the intracluster plasma ([MV07](#)). In particular, the abruptness of the temperature and

density changes across the front strongly limits thermal conductivity and diffusion (Ettori & Fabian 2000; Vikhlinin et al. 2001a; MV07), suggesting that the magnetic field drapes around the front surface and insulates the front.

### 1.3.1 Thermal conductivity

Thermal conductivity is one of the important but poorly known properties of the ICM. It is determined by the topology of the tangled magnetic field frozen into the ICM and by plasma microphysics. The heat transport should be completely suppressed across the field lines (because the electron gyroradii are many orders of magnitude smaller than other relevant linear scales in the ICM, Sarazin 1988), while heat may flow along the lines between those regions of the ICM for which such a path along the lines exists. However, even *along* the field lines, the heat transport may be strongly suppressed in a high- $\beta_P$  plasma (such as the ICM) because of micro-scale plasma instabilities (e.g., Schekochihin et al. 2008).

Observationally, few definitive measurements have been done. Across cold fronts, where the temperature jumps abruptly, thermal conductivity has been shown to be suppressed by at least a couple of orders of magnitude compared to the Spitzer value (Ettori & Fabian 2000, and later works). The likely explanation is the magnetic field “draping” along the cold front surface as a result of the gas flowing around it, which effectively isolates the two sides of the front from each other (Vikhlinin et al. 2001b; Markevitch & Vikhlinin 2007; ZuHone et al. 2011). Some constraints outside the special regions of cold fronts have been reported, based on the existence of spatial temperature variations in the ICM. For example, Markevitch et al. (2003b) derived an order of magnitude sup-

pression of conductivity between regions of different temperature in the body of a hot merging cluster A754, and [Eckert et al. \(2012\)](#) derived a large suppression factor based on the survival of a tail of cool gas stripped from a group infalling into the hot cluster A2142. In both cases, the physical significance of the constraints is ambiguous because the topology of the magnetic fields is unclear — for example, it is possible (and in the case of the infalling group, likely) that the observed regions of the different temperature come from separate subclusters whose magnetic field structures remained topologically disconnected even after the merger, so there are simply no pathways for heat exchange (as suggested in [Markevitch et al. 2003b](#)). Indirect upper limits on the effective isotropic conduction based on the analysis of ICM density fluctuations have also been derived (e.g., [Gaspari & Churazov 2013](#)).

In [Chapter 2](#), the disrupted cool core remnants of A520 is analyzed. Its stretched appearance and sharp edges against the hotter post-shock gas suggests that the aforementioned magnetic draping over a cold front applies, preventing mixing and thermal conduction across the edge. Inside the trail of cool gas, one might expect the magnetic field to be more aligned with the flow and therefore not inhibitive to diffusion and thermal conduction. We measured the projected temperatures of several adjacent blobs of gas that appear to have different temperatures, and compared the timescales to erase their temperature difference with their estimated age based on their distances to the tip of the remnants (see [§ 2.5.4](#)).

### 1.3.2 Kelvin-Helmholtz instabilities and constraint on effective viscosity

In sloshing cold fronts, because the gas tangential velocity is discontinuous across the front, cold fronts should develop Kelvin-Helmholtz (KH) instabilities. As indeed observed in, e.g., A3667, Bullet and NGC 1404, these instabilities lead to eventual dissolution of the sharp interface. The growth of the KH instability depends on — and therefore can be used to constrain — the plasma viscosity and the structure and strength of the magnetic fields (Vikhlinin et al. 2001b; MV07; Roediger et al. 2013b, hereafter R13), though separating these two stabilizing effects may not be straightforward (ZuHone et al. 2015). Evidence for cold fronts developing KH instabilities has been seen indirectly in the form of multi-edge structure of the radial brightness profile and “boxy” shape of the fronts, both consistent with being KH eddies seen in projection (e.g., Virgo, A496, Roediger et al. 2013a, Roediger et al. 2012; NGC 1404, Su et al. 2017; A3667, Ichinohe et al. 2017). Their existence has been used to place an upper limit on the plasma *isotropic* viscosity (that is, disregarding the effect of the magnetic fields) to be  $\sim 10\%$  of the Spitzer value. As shown by MHD simulations (ZuHone et al. 2015), in the context of sloshing cold fronts, the suppression of KH instabilities in a plasma with a magnetic field draping around the cold front, with anisotropic Braginskii viscosity that describes magnetized plasma, should be qualitatively similar to the effect of a 1/10 Spitzer isotropic viscosity.

In Chapter 4, the southern cold front of A2142 is analyzed. The physical scale of the apparent KH eddies are used to estimate the effective viscosity there.

### 1.3.3 Plasma depletion layer

The ICM typically has a high  $\beta \sim 100$ , the ratio of thermal pressure to magnetic field pressure, with magnetic field strength in the range of a few microgauss. Thermal energy density dominates, and magnetic fields are advected with the plasma motion, i.e. field lines are frozen in with the plasma. In certain scenarios where there is coherent ICM flow, the magnetic field strengthens as field lines are stretched along the flow and bunch together. Such a situation is believed to be found in front of cold fronts, where the outer gas flows around, in the form of magnetic draping (Fig. 1.3). Simulations of sloshing cold fronts show that even inside the sloshing cool gas, magnetic field pressure can become significant (Fig. 1.4). As magnetic pressure rises, gas is squeezed out of the region so that the thermal pressure lowers to maintain overall pressure equilibrium with the surrounding gas. If sufficient amount of gas is squeezed out of the region, it will have a deficit of X-ray emission. In favorable projections, these may appear to be dim channels in the X-ray surface brightness.

In each of A520 and A2142, we noticed and examined such an X-ray channel (§ 2.5.2, § 4.5). In both cases, we ascertained they were not instrument artifacts and their appearances seem to be related to the large scale features. Their origin are probably very different; in A520 it is in a likely turbulent central region of the cluster, and could be a tube of hot gas from subcluster passage or a squashed AGN bubble; in A2142 it is just offset from the southern cold front and may be related to magnetic draping. Based on the amount of dimming, their geometry is that of a sheet seen edge-on. Presently, there are few examples of such X-ray channels to compare. Because they are narrow ( $\sim 10$  kpc)

and dim, long exposures requiring *Chandra*'s spatial resolution are needed. The plasma depletion layer phenomenon has been measured in-situ at the sunward side of the Earth's magnetopause and studied extensively (e.g., Øieroset et al. 2004 showed the presence of a depletion layer in front of the magnetosphere of the Earth's bow shock), in the cluster context it has neither been observed nor excluded for the most promising place to find it — in front of a cold front. While observationally difficult, such a measurement could potentially shed more light on the magnetic field strength in the ICM.

## 1.4 Imaging analysis techniques

In the subsequent chapters, we show many images of X-ray surface brightness and maps of gas temperature. In this section, we outline the method used to derive these images, leaving specific details to later. We also describe the two image enhancement techniques we used to derive adaptively smoothed temperature maps.

### 1.4.1 Images of X-ray surface brightness

*Chandra* records the position and energy of each photon detection. By projecting the spatial coordinates of these events onto a grid, we can derive an image of photon counts, as well as apply an energy filter to the events. After correcting for the quiescent background (consisting of the soft cosmic X-ray background and cosmic rays) and the readout artifact (see later, § 2.2), we divide the counts image by an exposure map that captures the spatial variations of the detector response function convolved with the dithering of telescope pointing position, as well as the energy dependent response to an assumed

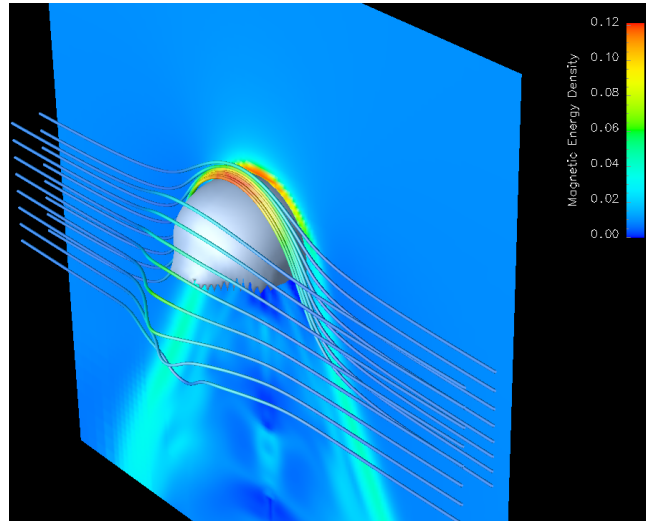


Figure 1.3: Magnetic draping in front of a cold front in simulations. (From [Dursi & Pfrommer 2008](#).)

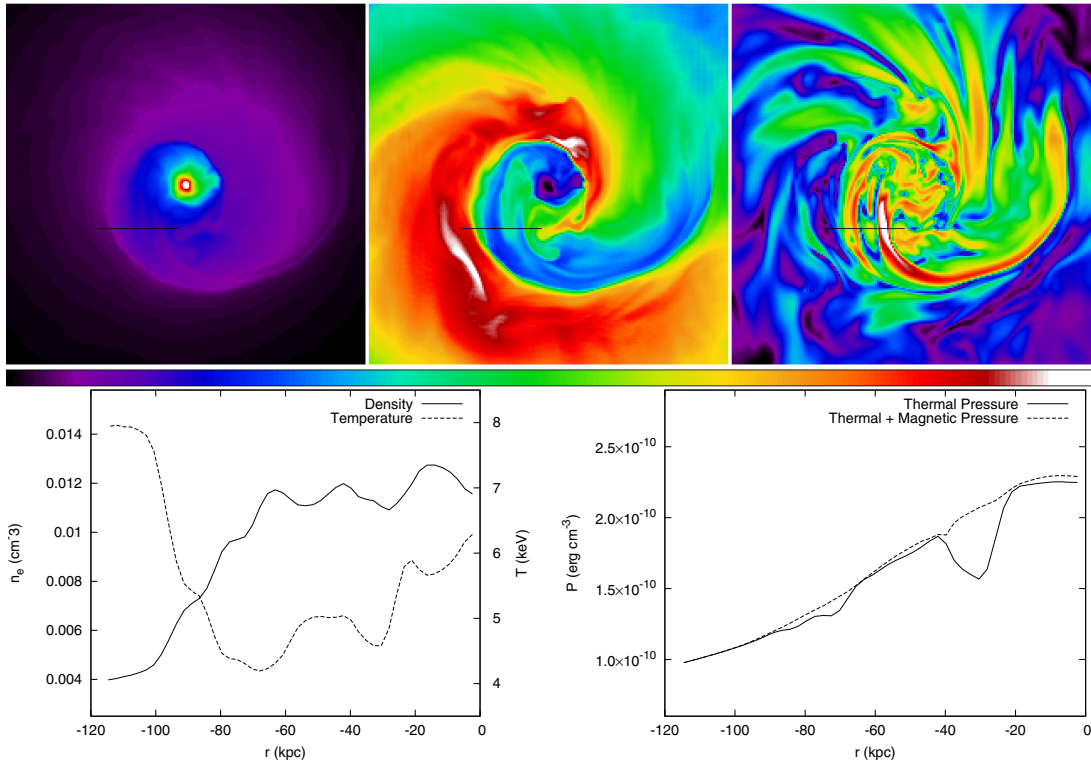


Figure 1.4: A simulated sloshing cold front with a region of significant magnetic pressure, where thermal pressure drops by 25%. The figures show density, temperature, and magnetic pressure slices. (From [ZuHone et al. 2011](#).)

source spectrum. This exposure map has units of effective exposure time, and corrects for the detector quantum efficiency, vignetting, and effective area. We do not include the effective area itself in our exposure maps. The resulting flux images are divided by the angular size of an image pixel to have units of [photons s<sup>-1</sup> arcsec<sup>-2</sup>]. Due to the energy dependence of the detector response and of the mirror effective area, a source spectrum is required to calculate the exposure map. For this, we use the best-fit single temperature model of the whole cluster. In the subsequent analysis using X-ray brightness as proxy for the gas density, we check whether differences in gas temperature has a significant (but typically small) effect on the X-ray emissivity and make the necessary corrections in our density modelling.

Unless otherwise noted, north is up and east is left in all of our images.

#### **1.4.2 Image reconstruction using wavelet decomposition**

Wavelet decomposition is an image analysis technique that has been applied to astronomical images to identify statistically meaningful structures at different scales. X-ray images of the ICM are typically noisy, since it is extended and dim. In this context, wavelet decomposition can be used to pick out statistically significant sources in the presence of noise, for example to identify point sources in low signal-to-noise images, or to analyze small scale structure (e.g. [Grebenev et al. 1995](#)). Another application for it is in reconstructing an image without the noise (e.g. [Slezak et al. 1994](#)). We can also go further and selectively reconstruct the image using only the scales of interest — a qualitative deprojection of the larger scale emission. In this work, we use the full wavelet reconstruction for a better qualitative presentation of structures in the ICM (e.g. [Fig. 2.2b](#))

and as the basis for controlling the smoothing radius when creating temperature maps (§ 1.4.4). We also make use of selective reconstruction to derive qualitative temperature maps of structures on smaller scales (§ 1.4.5). Unlike a smoothing scheme such as Gaussian smoothing, which blurs everything with a symmetric kernel, the wavelet components better preserve the shapes and brightness contrast of interesting small-scale features while at the same time having a basis in the statistical significance of the structures selected by the algorithm.

We perform wavelet decomposition using Alexey Vikhlinin’s `wvdecomp` tool in ZHTOOLS.<sup>1</sup> Using a method described in Vikhlinin et al. (1994, 1998), wavelet components are extracted with the *a trous* kernel (e.g. Starck & Murtagh 1994) with scales increasing in geometric progression, by a factor of 2. The component scales used are described in the text for each of our wavelet analysis.

### 1.4.3 Temperature maps

We create temperature maps of the ICM using best-fit gas temperatures at each pixel, using heavily binned spectral information (both in the energy dimension, and in spatial coordinates by smoothing). In general, we follow the procedure described in Markevitch et al. (2000). First, we extract several narrow band flux images between 0.8–9 keV, and when necessary exclude certain energy ranges (e.g. 1.7–1.9 keV edge and 7.3–7.6 keV, possibly affected by poor subtraction of the instrumental lines). We also calculate the corresponding error images. Next, these narrow band images are smoothed using one of the two adaptive smoothing methods in the following sections. Finally, a

---

<sup>1</sup><http://hea-www.harvard.edu/RD/zhtools/>

single temperature MEKAL model is fitted to the set of flux values at each pixel of the image. For the fit, the absorption column and metal abundance are fixed to the cluster best fit values.

#### **1.4.4 Adaptive smoothing using variable-width Gaussian kernel**

For this approach, narrow-band images are first smoothed using a Gaussian kernel whose width at each image pixel is determined by surface brightness in the 0.8–4 keV band, with the goal of preserving detail in bright regions. As a reference for this smoothing method, we use a wavelet reconstruction of the 0.8–4 keV image, as described in § 1.4.2. This way, the smoothing radius is unaffected by photon noise and point sources. Based on this reference image, the narrow-band images and their corresponding error images (with point sources excised) are identically smoothed by a Gaussian whose width is some function of the surface brightness value in the reference image. By inspecting the error in the derived temperature map, we then select empirically a function of the form  $r_{\text{smooth}} \propto S_X^{-a}$  where  $S_X$  is the surface brightness, and  $a$  is some constant typically between 0.3 and 0.7, while also setting the minimum and maximum smoothing scales, to achieve a balance between revealing the temperature variations and suppressing noise.

#### **1.4.5 Wavelet reconstruction temperature maps**

The second method uses wavelet image decomposition to identify structures at different angular scales, and leave only the wavelet components on the scales of interest in the narrow-band images used for temperature fitting, instead of simple Gaussian smoothing. This method allows us, for example, to subtract the structures on large angular scales

and recover the temperature contrast of features on the interesting small scales by reducing the projection effects. Of course, such “deprojection” can only be qualitative, as we do not know the gas distribution along the line-of-sight (l.o.s.) and have to assume that structures on different scales are simply projected. Nevertheless, for the interesting high-contrast features in A520 and in A2142, this assumption should be close to reality.

This method has the greatest utility to recover the small-scale, cool, and bright structures that have large brightness gradients (e.g. at the “foot” and “leg” of A520 shown in Fig. 2.2). These high-contrast structures are mostly lost in the adaptive Gaussian smoothing. By using the wavelet decomposition instead of smoothing, the shape of these brightness features are better preserved.

Using the 0.8–4 keV image, we determine the appropriate wavelet reconstruction, selecting the thresholds of statistical significance in order to achieve balance between retaining small-scale details and minimizing noise and artifacts. The wavelet decomposition coefficients calculated for the 0.8–4 keV image are then used for the narrow-band images and their corresponding error images (that is, the same smoothing was applied in all energy bands, as in §1.4.4). Point sources in the small scale component are removed from those images before coadding the different scales. This results in, e.g., the temperature map shown in Fig. 2.3*b*; it reveals the small-scale structure much better than the one in panel *a* at the expense of being only qualitative.

## CHAPTER 2

---

### The merging galaxy cluster A520 — A broken-up cool core, a dark subcluster, and An X-ray channel

*This chapter has been adapted from the published version in *The Astrophysical Journal*, Vol. 833, p. 99 ([Wang et al. 2016](#)).*

We present results from a deep *Chandra* X-ray observation of a merging galaxy cluster A520. A high-resolution gas temperature map reveals a long trail of dense, cool clumps — apparently the fragments of a cool core that has been stripped from the infalling subcluster by ram pressure. The clumps should still be connected by the stretched magnetic field lines. The observed temperature variations imply that thermal conductivity is suppressed by a factor  $> 100$  across the presumed direction of the magnetic field (as found in other clusters), and is also suppressed *along* the field lines by a factor of several. Two massive clumps in the periphery of A520, visible in the weak lensing mass map and the X-ray image, have apparently been completely stripped of gas during the merger, but then re-accreted the surrounding high-entropy gas upon exit from the cluster central region. The mass clump that hosted the stripped cool core is also reaccreting hot-

ter gas. An X-ray hydrostatic mass estimate for the clump that has the simplest geometry agrees with the lensing mass. Its current gas mass to total mass ratio is very low, 1.5–3%, which makes it a “dark subcluster”. We also found a curious low X-ray brightness channel (likely a low-density sheet in projection) going across the cluster along the direction of an apparent secondary merger. The channel may be caused by plasma depletion in a region of an amplified magnetic field (with plasma  $\beta \sim 10 - 20$ ). The shock in A520 will be studied in [Chapter 3](#).

## 2.1 Introduction

The hot ( $T \simeq 7$  keV, [Govoni et al. 2004](#)) galaxy cluster Abell 520 at  $z = 0.203$  ([Westphal et al. 1975](#)) is one of only a handful of merging systems with a shock front clearly visible in the sky plane ([Markevitch et al. 2005](#), hereafter M05), which makes the merger geometry quite unambiguous. The cluster has a detailed map of the projected total mass distribution derived from weak gravitational lensing data ([Mahdavi et al. 2007](#); [Okabe & Umetsu 2008](#); [Jee et al. 2012](#); [Clowe et al. 2012](#); [Jee et al. 2014](#)). [Fig. 2.1](#) shows the weak lensing mass map from [Clowe et al. \(2012\)](#) against a HST image, *Chandra* X-ray contours, and galaxy luminosity. In our figures, we show contours for an uncropped version of the mass map from [Clowe et al. \(2012\)](#), provided by D. Clowe (private communication), e.g. in [Fig. 2.2c](#). While the above authors disagree on the details (in particular, [Mahdavi et al.](#) and [Jee et al.](#) reported the presence of a “dark clump” with an anomalously high  $M/L$  ratio in the middle of the cluster, marked by a green cross in [Fig. 2.2c](#), while [Clowe et al.](#) contested its statistical significance), the lensing maps agree qualitatively quite well. The overall picture is a “train wreck” of several mass clumps mostly

aligned in a chain along the NE-SW direction. This is consistent with the merger direction indicated by the X-ray shock front.

In this chapter, we analyze in detail an extra-deep 0.5 Ms *Chandra* observation of A520. It will allow us to gain insights into many of the above physical processes, such as the cool core stripping and the suppression of thermal conductivity. Analysis of the shock front based on the same X-ray data, supplemented by the archival radio data, will be given in [Chapter 3 \(Wang et al. 2018\)](#).

We assume a flat cosmology with  $H_0 = 70 \text{ km s}^{-1} \text{ Mpc}^{-1}$  and  $\Omega_m = 0.3$ , in which  $1''$  is 3.34 kpc at  $z = 0.203$ . Errors are quoted at 90% confidence in text, and at  $1-\sigma$  in figures, unless otherwise stated.

## 2.2 X-ray data analysis

We analyzed observations of A520 with *Chandra* Advanced CCD Imaging Spectrometer (ACIS) between December 2007 and January 2008 for a total of 447 ks (ObsIDs 9424, 9425, 9426, 9430). This gave 423 ks after cleaning for flares as described in the next paragraph. We chose not to combine these with earlier observations (ObsIDs 528, 4215, and 7703 with exposure times 9.47 ks, 66.27 ks, and 5.08 ks, respectively). The two short observations will not meaningfully improve our results so we omitted them for simplicity. ObsID 4215 is affected by a long low-level background flare, which [M05](#) modelled as an excess over the quiescent background and propagated the error for spectral modelling. Seeing this would increase our total exposure time by at most 15%, yet potentially introduce more uncertainty to background subtraction (see [§ 2.2.1](#)) we chose

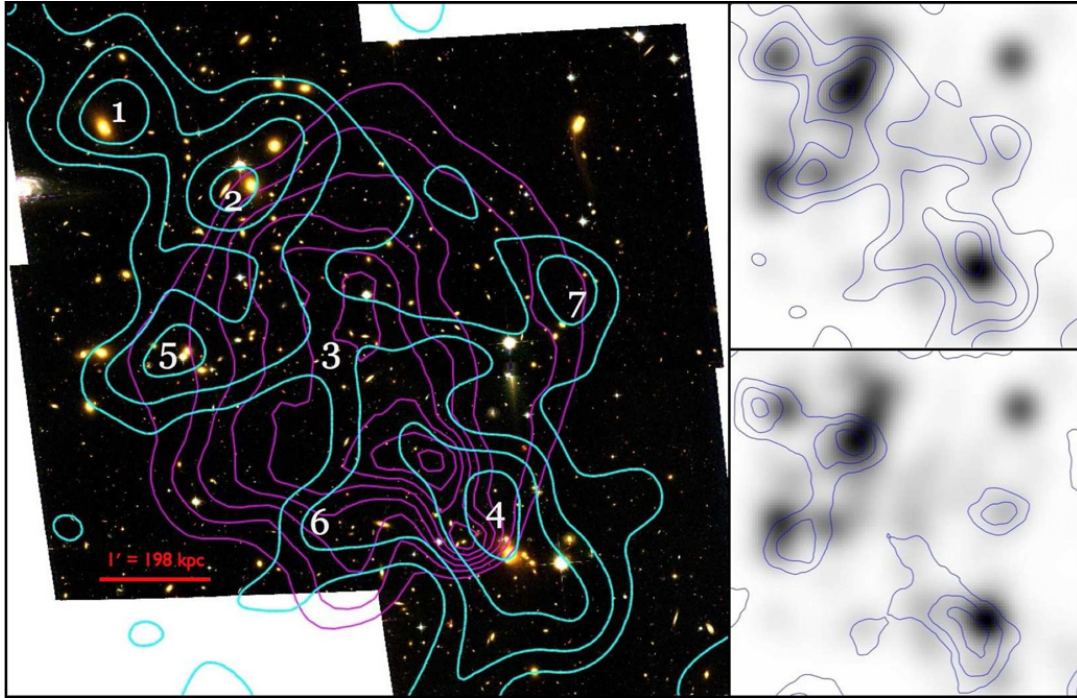


Figure 2.1: Left: a mosaic color composite image from HST ACS, with weak-lensing surface density reconstruction contours in cyan, and *Chandra* X-ray surface brightness contours in purple overlaid. An uncropped version of the mass contours is used in this chapter. The top right image shows the same mass contours overlaid on smoothed cluster galaxy luminosity distribution. The bottom right image shows the same, but with contours of statistical significance of the mass density map, in steps of  $1\sigma$ . (From [Clowe et al. 2012](#).)

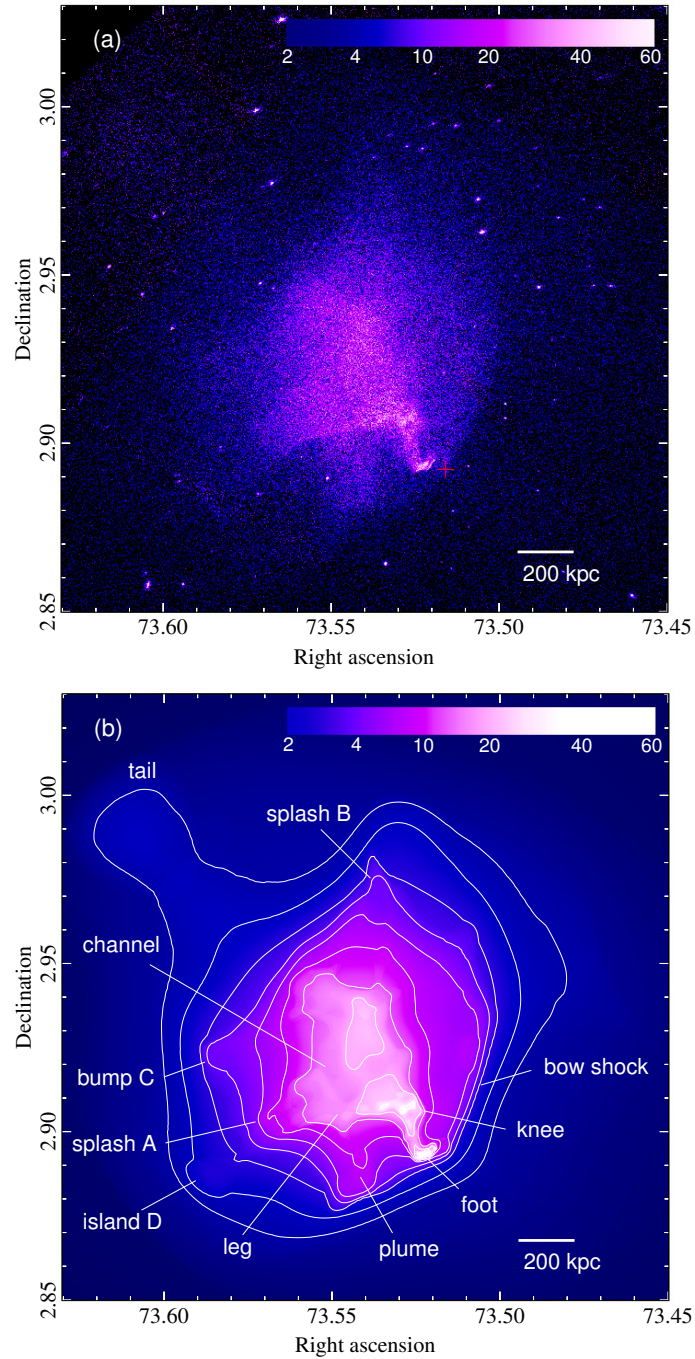


Figure 2.2: (a) *Chandra* 0.8–4 keV surface brightness binned to 1'' pixels, without smoothing or source removal. The color scale is in units of  $10^{-6}$  counts  $s^{-1}$  arcsec $^{-2}$ . The red cross marks the center of the BCG, offset from the bright tip by about  $20'' = 67$  kpc. (b) Wavelet smoothing of the image in panel *a*, with point sources removed, with brightness contours spaced by factor 1.5. Prominent features discussed in this chapter are marked in panels *b* and *d*.

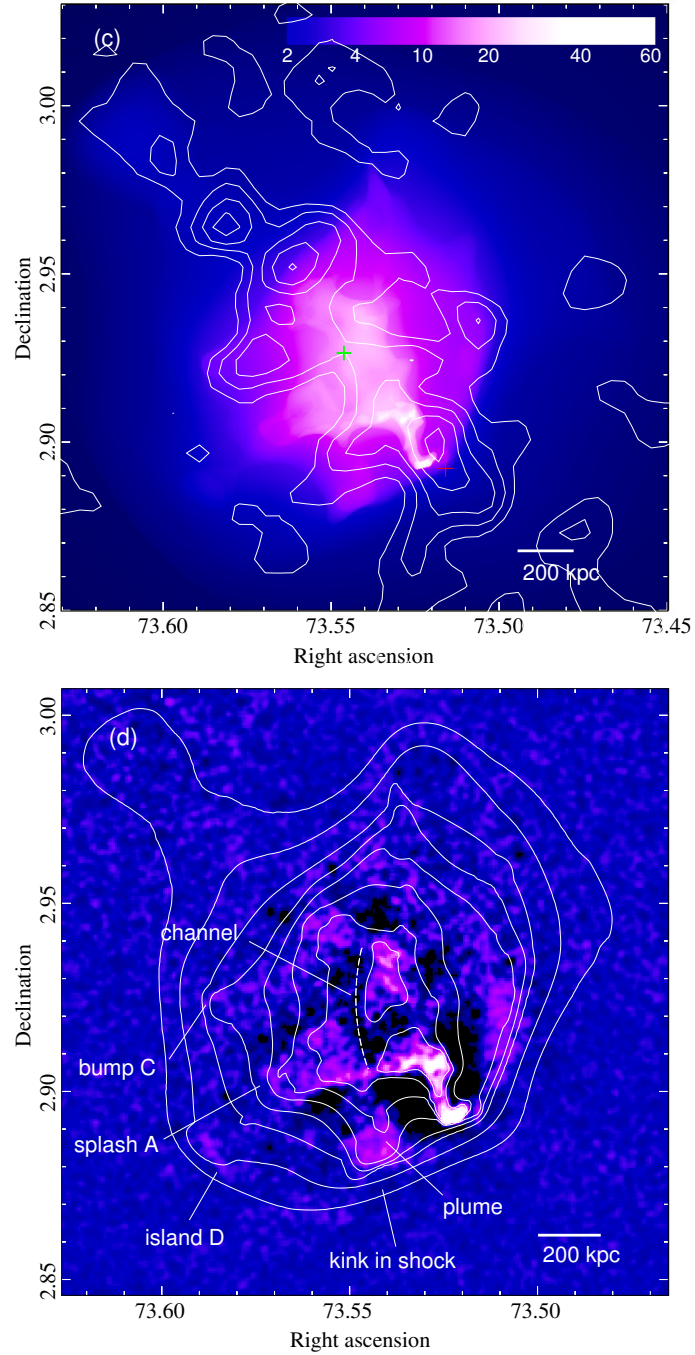


Figure 2.2: (*—continued.*) (c) Weak lensing mass contours from D. Clowe (private communication), overlaid on the wavelet X-ray image from panel *b*. The contour levels (mass surface density, linear step) are same as in Clowe et al. (2012). Green cross marks the position of the contested “dark clump”, the red cross marks the BCG. (d) Residual X-ray image after subtracting the  $> 210$  kpc scale wavelets components, slightly smoothed. Prominent features discussed in this chapter are marked in panels *b* and *d*.

not to complicate our subsequent analysis.

We reprocessed Level=1 event files using `acis_process_events` of the *Chandra* X-ray Center (CXC) software, CIAO (4.6).<sup>1</sup> We applied the standard event filtering procedure of masking bad pixels, grade filtering, removal of cosmic ray afterglow and streak events and the detector background events identified using the VFaint mode data. Periods of elevated background were identified using the 2.5–7 keV light curve in a background region free of cluster emission on the ACIS-I chips (by excluding a circle of  $r = 7'$  centered on A520 and another circle of  $r = 1.5'$  on a small extended source to the SW). Time bins of 1 ks were used, and bins whose count rates were more than 20% different from the mean value were discarded, resulting in 423 ks of total clean exposure. During the clean exposure, no gradual changes in the quiescent background level were apparent during any of the observations; the mean rates varied with time by less than 10%. We also checked that there was no time variability in the ratio of the 2.5–7 keV to 9.5–12 keV counts using time bins of 10 ks. The mean value of this ratio was also in good agreement (within 2%) of that in the blank-sky background dataset. The latter two checks ensure the absence of faint residual background flares and the accuracy of modeling the detector background using the blank-sky dataset (Hickox & Markevitch 2006) that we describe below.

The ACIS readout artifact was modeled using `make_readout_bg`<sup>2</sup> and treated as an additional background component in our analysis (as in Markevitch et al. 2000).

To create flux images, exposure maps were created using Alexey Vikhlinin's tools.<sup>3</sup>

---

<sup>1</sup><http://cxc.harvard.edu/ciao>

<sup>2</sup>[http://cxc.harvard.edu/contrib/maxim/make\\_readout\\_bg](http://cxc.harvard.edu/contrib/maxim/make_readout_bg)

<sup>3</sup><http://hea-www.harvard.edu/~alexey/CHAV>

The exposure maps account for the position- and energy-dependent variation in effective area and detector efficiency. The exposure maps for different observations were co-added in sky coordinates. Then, the co-added background-subtracted counts images were divided by the total exposure map to produce a flux image. The four observations of A520 were set up with small relative offsets in the sky to minimize the effect of chip gaps on the final total image.

We excluded point sources from our analysis by visually inspecting the 0.8–4 keV and 2–7 keV images at different image binning and smoothing scales.

### 2.2.1 Sky background

To model the detector and sky background, we used the ACIS blank-sky background dataset from the corresponding epoch (“period E”) as described in [Markevitch et al. \(2003b\)](#) and [Hickox & Markevitch \(2006\)](#). The VFaint mode filter was applied; the events were projected to the sky for each observation using `make_acisbg`.<sup>4</sup> The count rate derived from the background data was then scaled so that it had the same 9.5–12 keV counts as the observed data. This was further reduced by 1.32% to accommodate the amount of background contained in the readout artifact. For flux images, this was done by multiplying the background counts image by a rescaling factor. For spectral analysis, this was effected by setting the `BACKSCAL` keyword in the spectra FITS files.

After subtracting the ACIS background normalized by the 9.5–12 keV rate, the 90% uncertainty of the 0.8–9 keV quiescent background normalization is 3% ([Hickox & Markevitch 2006](#)). We will vary the background normalization by this amount to estimate

---

<sup>4</sup><http://cxc.harvard.edu/contrib/maxim/acisbg/>

its contribution to the overall uncertainties. This is particularly important for the low surface brightness cluster outskirts for which the temperature uncertainties are dominated by the background; hence our decision to exclude ObsID 4215 in our analysis due to the presence of a flare.

After subtracting the blank-sky and readout artifact backgrounds, the spectrum of the cluster-free background region revealed a small positive residual flux mostly at  $E \sim 2$  keV. Some residual (positive or negative) is expected, as the soft CXB varies across the sky and the blank-sky dataset comes from other regions of the sky. We modeled this residual in the 0.5–9 keV band with an empirical spectral model consisting of two APEC components, a power law and a Gaussian to emulate an emission line. The thermal components were set to temperatures of 0.2 keV and 0.4 keV and their normalizations were allowed to vary, based on the study of the soft CXB ([Markevitch et al. 2003a](#)). The Gaussian component best fit was at  $E = 0.92 \pm 0.02$  keV with zero width ( $\sigma < 0.04$  keV). The power law component was added to account for the residuals above 2 keV, and it was found that a photon index of 0.6 made a qualitative improvement to the best fit. Of course, there is no physical significance to this empirical model, as it describes a difference between the true CXB (and possibly a very faint residual flare emission) and the CXB components included in the blank-sky dataset. An alternative is to use the “stowed” ACIS background dataset, which contains only the detector background, and add physically-motivated CXB components. However, the available stowed background dataset has a much shorter exposure than the blank-sky dataset, which is critically important for our extra-deep A520 observation. We assumed that our empirical residual background was constant across the FOV (before the telescope vignetting), and

included this model, adjusted for sky area and exposure time, when doing spectral fits for the cluster regions. For the narrow-band flux images, the residual was accounted for by subtracting a constant value such that the flux in the background region was zero. A520 is sufficiently small and there is enough cluster-free area within the FOV to make this additional background modeling step possible.

### 2.2.2 Spectral analysis

The instrument responses for spectral analysis were generated as described in [Vikhlinin et al. \(2005\)](#). We used the CHAV tool `runextspec` to generate the PHA, ARF and RMF files for each pointings. The PHA files (observed data, blank-sky background and readout background) were co-added using `addspec` from FTOOLS package. The `addarf` and `addrmf` from FTOOLS were used to add ARFs and RMFs. They were weighed by 0.5–2 keV counts in the applicable spectral extraction region.

Spectral analysis was performed in XSPEC (version 12.8.2). A single-temperature fit to the cluster in a 3' circle (0.6 Mpc) centered on soft band flux centroid at  $(\alpha, \delta) = (04:54:09.7, +02:55:25)$  (FK5, J2000) gives  $T = 8.3 \pm 0.3$  keV, metal abundance  $0.21 \pm 0.02$  (relative to [Anders & Grevesse 1989](#)) and absorption column  $N_{\text{H}} = (6.3 \pm 0.7) \times 10^{20} \text{ cm}^{-2}$ . Factored into the error are formal error from fitting, effect of the modeled soft residual background and the 3% uncertainty of the blank-sky background (§2.2.1); these were added in quadrature. We fitted all spectra in the 0.8–9 keV band, excluding the 1.7–1.9 keV and 7.3–7.6 keV intervals that are occasionally affected by detector artifacts. The best-fit Galactic  $N_{\text{H}}$  is consistent with  $5.7 \times 10^{20} \text{ cm}^{-2}$  from the LAB survey ([Kalberla et al. 2005](#)); with  $N_{\text{H}}$  fixed at the LAB value, we obtain  $T = 8.5 \pm 0.3$  keV, while the abundance

is the same. It is also in good agreement with the galactic HI+H2 column density of  $6.9 \times 10^{20} \text{ cm}^{-2}$  (Willingale et al. 2013)<sup>5</sup>. In subsequent spatially-resolved analysis, we chose to use our best-fit value of  $n_{\text{H}}$  in order to compensate for any inaccuracies in the calibration of the time-dependent ACIS low-energy response (while our choice of the 0.8 keV lower energy cutoff should minimize their effect). We also fixed the abundance at its best-fit value, as many of our fitting regions do not have enough counts to constrain either  $N_{\text{H}}$  or abundance.

## 2.3 Temperature maps

Temperature maps shown in Fig. 2.3 were derived following the method described in § 1.4.3. For A520, we extracted 6 narrow band flux images between 0.8–9 keV, excluding the 1.7–1.9 keV edge and 7.3–7.6 keV (possibly affected by poor subtraction of the instrumental lines). The absorption column and metal abundance were fixed to the cluster best fit values.

### 2.3.1 Smoothing with variable-width Gaussian kernel

For this approach, we followed the method described in § 1.4.2 to obtain the wavelet reconstruction images, and the method described in § 1.4.4 to derive the variable-width Gaussian smoothed temperature map. For the wavelet reconstruction, we extracted wavelet components (with the *atrous* kernel and scales increasing in geometric progression) on scales of 53, 105, 210 and 420 kpc (or 15.7", 31.5", 63.0" and 126"). Point sources are contained in wavelet components on smaller scales than the first scale above, thus not in-

---

<sup>5</sup>Online tool: <http://www.swift.ac.uk/analysis/nhtot/index.php>

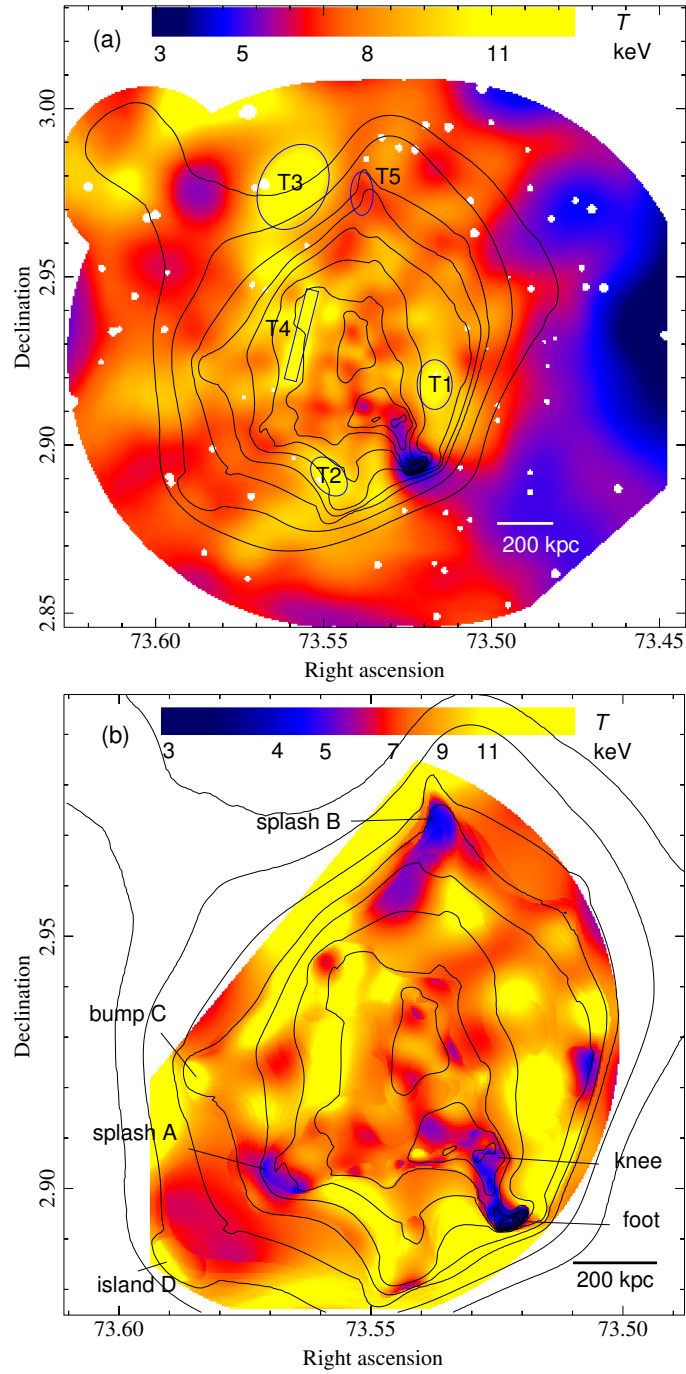


Figure 2.3: (a) Variable smoothing temperature map with X-ray contours. The holes in the map are masked point sources. (b) Wavelet temperature map. The fitted images were reconstructed from component wavelet scales of 6.6, 13, 26, 53, 105 and 210 kpc.

cluded. These image components were then co-added with the residual image smoothed by the 840 kpc scale wavelet. This procedure retains most of the statistically-significant extended structures on various angular scales. The resulting image is shown in [Fig. 2.2b](#) next to the original unsmoothed image; we will use it as reference when discussing various features in this cluster.

Based on this reference image, the narrow-band images and their corresponding error images (with point sources excised) were identically smoothed by a variable-width Gaussian. By inspecting the error in the derived temperature map, we empirically determined this scaling of surface brightness and width of the Gaussian kernel,  $r_{\text{smooth}} \propto S_X^{-0.7}$ , and smoothing radius between 13 kpc and 200 kpc. We found that this achieved a balance between revealing the temperature variations and suppressing noise. The resulting temperature map is shown in [Fig. 2.3a](#).

To check the validity of values shown in the map, we extracted the spectra in a few hot spots ( $T > 10$  keV) and a cooler spot (regions T1-T4 and T5 in [Fig. 2.3a](#), respectively) and fitted their projected temperatures in XSPEC. For T1, we obtain  $12.1^{+3.4}_{-2.4}$  keV; for T2,  $11.3^{+4.1}_{-2.6}$  keV; for T3, we could only obtain a lower bound of 11.9 keV. For T4, the fit is  $12.2^{+2.5}_{-1.9}$  keV, and for T5,  $6.4^{+2.2}_{-1.4}$  keV — all values close to those derived from the smoothed map.

### 2.3.2 Wavelet-smoothed temperature map

We also derived a wavelet-smoothed temperature map following the method described in [§ 1.4.5](#). We extracted wavelet components from the 0.8–4 keV image binned to 1'' pixels, using 6.6, 13, 26, 53 and 105 kpc scale wavelets, selecting the thresholds of

statistical significance in order to achieve balance between retaining small-scale details and minimizing noise and artifacts. Point sources in the 6.6 kpc wavelet component were removed from those images before coadding different scales. The resulting temperature map is shown in Fig. 2.3b; it reveals the small-scale structure much better than the one in panel *a* at the expense of being only qualitative.

## 2.4 Results

### 2.4.1 Shock front (or fronts?)

The bow shock to the SW of the cluster center, first reported in M05, is readily apparent in the 0.8–4 keV image (Fig. 2.2) and in the temperature map (Fig. 2.3). The latter shows a region of about 5 keV in front of the shock and 9–10 keV behind the shock. We extracted spectra from 4 sectors in 2 annular regions in front of the shock (S3-S10), and 3 sectors (S0-S2) including the shock (Fig. 2.5). In the pre-shock region, temperatures are  $\sim 5$  keV and are remarkably similar over this large area. Overall it appears that pre-shock region is cool and undisturbed, with temperature falling with radius slightly from  $T = 5.7 \pm 0.8$  keV (S3-S6 combined,  $r \sim 650$  kpc from the cluster center) to  $T = 4.5 \pm 0.8$  keV (S7-S10 combined,  $r \sim 900$  kpc). Behind the shock, in regions S0-S2, the temperatures span 8–14 keV. The values are consistent with M05 analysis of a shorter dataset, who found  $T = 4.8^{+1.2}_{-0.8}$  keV in front of the shock and  $T = 11.5^{+6.7}_{-3.1}$  keV behind (the latter value is deprojected, therefore not directly comparable to that here). In region S2, a cool blob of gas appears to be projected onto the shock. This feature is coincident with a small but discernible brightness enhancement in the soft-band image. It could be

a splash or a broken off blob of the cool core inside the shocked gas. Regardless of its origin, it is masked in the analysis of the shock, in [Chapter 3](#).

There is a kink in the shock surface (marked in [Fig. 2.2](#)), behind which (downstream from the shock) is a region of enhanced X-ray brightness (“plume” in [Fig. 2.2](#)). The gas in the plume (region S0) is as hot as the post-shock gas elsewhere, though the temperature map ([Fig. 2.3](#)) suggests a mixture of different temperatures there. It appears that a local gas inflow from the south is crossing the shock at that location.

There is an apparent steepening of the surface brightness profile along the NE-SW merger direction, northeast of the cluster center (located between splashes B and C in [Fig. 2.2b](#)) that looks like a counterpart (“reverse”) shock to the main shock front. However, we do not detect a significant difference in projected temperature between regions C3 and C4 ([Fig. 2.5](#)) ahead and behind that brightness feature. The presence of other features (splash B, bump C, the tail) makes this a crowded location compared to the clean SW bow shock, and it is unlikely we can deproject the emission correctly.

#### **2.4.2 Break up of the cool core remnant**

Behind the shock is a twisted structure resembling a leg (labelled in [Fig. 2.2b](#) and [Fig. 2.4](#)). There are dense clumps, as inferred from their high surface brightness, at the foot and at the knee, and more along the ridge extending east from the knee (most pronounced in the unsharp-masked image of [Fig. 2.2d](#)). The foot (zoomed onto in inset of [Fig. 2.5](#)) is particularly striking. It consists of two bright, very elongated ( $50 \times 10$  kpc and  $50 \times 20$  kpc in projection) clumps separated by a gap with an X-ray brightness contrast of  $> 2$ . Their projected temperatures are 1.5–2.5 keV ([Fig. 2.5](#)); the narrower

finger on the outside is the colder of the two. There is no apparent galaxy coincident with the foot, but the fingers are displaced from the center of the BCG of one of the infalling subclusters by only  $16''=50$  kpc.

The wavelet temperature map in Fig. 2.4 shows that cool clumps trace the structure extending north from the foot to the knee, which then turns east, continuing toward “splash A” and “splash D” (Fig. 2.3; splashes will be discussed in § 2.4.3). At the knee, a small X-ray brightness cavity does not show a significant deviation in projected temperature from the bright blobs above it. Not all the surface brightness enhancements correspond to cool spots (as one would expect if the structure were in pressure equilibrium), suggesting that projection effects are significant.

The overall picture strongly suggests that the “foot” and the bent “leg” formed as a result of the disruption of a cool core, once hosted by the subcluster centered on the BCG that is now ahead of the foot (Fig. 2.2). The cool core have been swept off its host by strong ram pressure of the merger, but has not yet been completely mixed with the hot surrounding gas. This is similar to the cool “bullet” in the Bullet cluster, shown in Fig. 1.1, displaced from the former subcluster host (Markevitch et al. 2002; Clowe et al. 2006), but, while the cool core in the Bullet cluster remains a coherent shuttlecock structure, in A520 the disruption has gone much further.

To see if this picture is consistent with the properties of the cool clumps, we estimate the gas specific entropy and check if it is similar to that in typical undisturbed cool cores. We calculate the specific entropy using the following definition (widely used in X-ray cluster work):

$$K = T n_e^{-2/3} \tag{2.1}$$

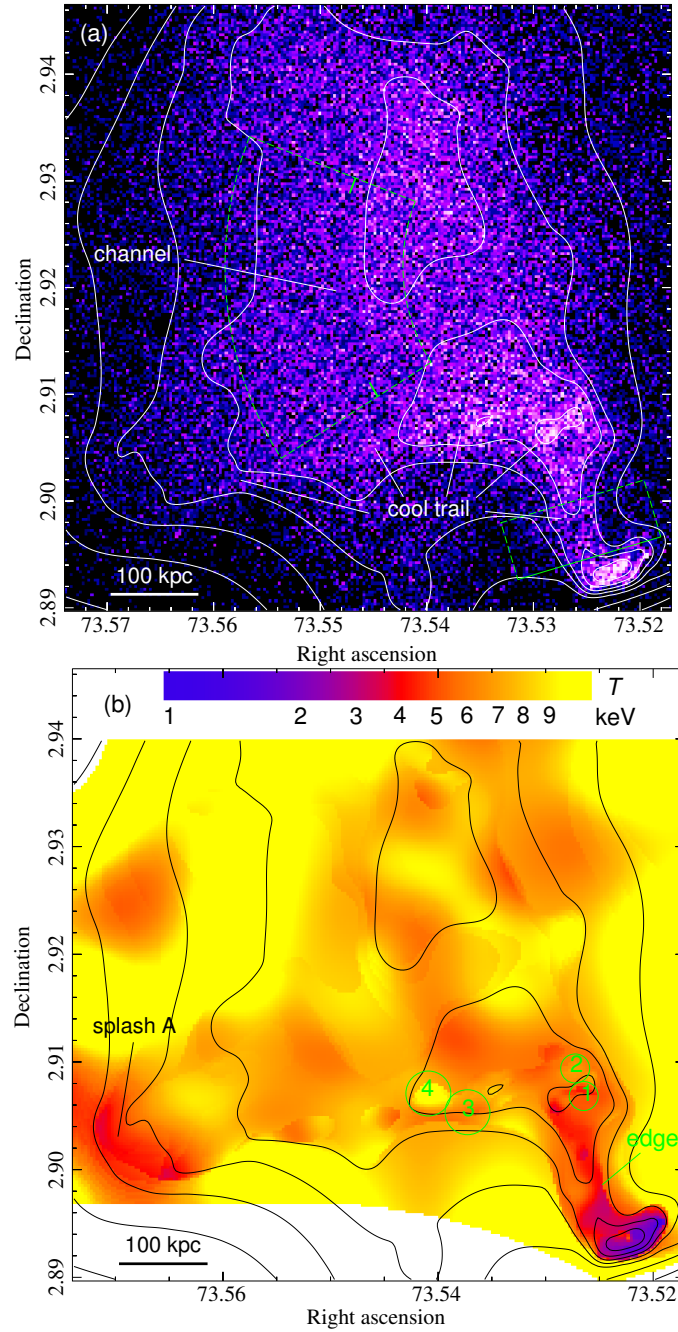


Figure 2.4: (a) 0.8–4 keV image binned to 1'' pixels. A radial profile within the dashed annular sector is shown in § 2.5.2, Fig. 2.6. A profile in the rectangular region across the cool trail just above the foot is shown in § 2.5.4, Fig. 2.8. (b) similar to Fig. 2.3b, but derived without the largest wavelet scale 210 kpc. Overlaid are X-ray contours. Note the color scale is different from that in Fig. 2.3. The green labels are related to our discussion of thermal conductivity in § 2.5.4.

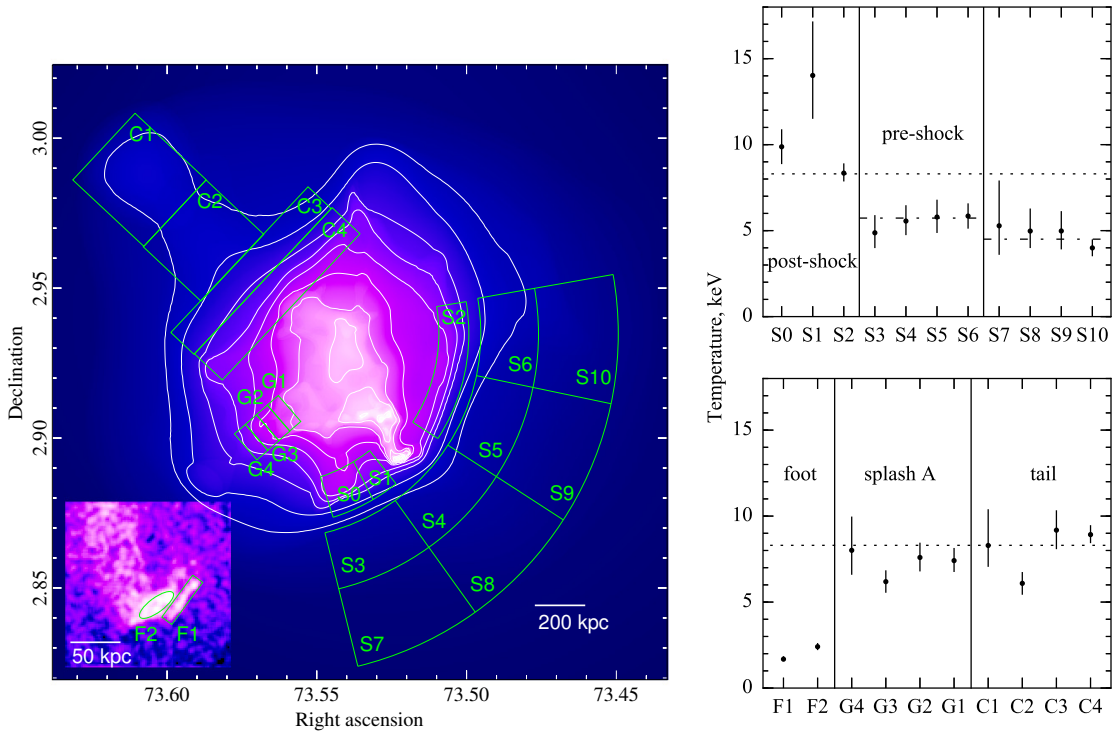


Figure 2.5: Spectral fitting regions shown on wavelet reconstructed 0.8–4 keV image with inset showing 4 $\times$  enlarged view of slightly smoothed 0.8–4 keV image of the tip. Projected temperatures fitted in XSPEC are shown with 1- $\sigma$  error bars. The dotted line shows the cluster average temperature, and the dot-dashed lines for S3-S6 and S7-S10 show the best fit temperatures in those regions combined.

where  $T$  is the gas temperature and  $n_e$  is the electron number density. In all of our analysis, we assume  $n_e = 1.17n_H$ . Since the regions in question are small and bright, they dominate the emission along the l.o.s., so no deprojection is needed for a qualitative estimate.

For the outer, thinner finger (F1 in Fig. 2.5),  $T = 1.7$  keV. If we use the size of the spectral fitting region and assume an elongated shape, i.e.  $10 \times 10 \times 50$  kpc square cuboid, the derived density is  $n_H = 2 \times 10^{-2} \text{ cm}^{-3}$ , giving  $K \approx 20 \text{ keV cm}^2$ . Since the emission is actually confined to a narrower part of the fitting region, if we assume instead a cylinder of the same length 50 kpc and diameter of 5 kpc (half the width of the extraction region), the density estimate increases by a factor  $\sqrt{16/\pi}$  to  $5 \times 10^{-2} \text{ cm}^{-3}$ , which gives  $K \approx 12 \text{ keV cm}^2$ . Alternatively, if the blob is cap-like, taking the geometry of a flat cylinder 50 kpc in diameter and 5 kpc thick, the density changes by a factor  $\sqrt{8/5\pi}$  to  $1.4 \times 10^{-2} \text{ cm}^{-3}$ , which gives  $K \approx 25 \text{ keV cm}^2$ .

For the inner, wider finger (F2 in Fig. 2.5),  $T = 2.4$  keV in an elliptical spectral extraction region. Its density is  $n_H = 1.3 \times 10^{-2} \text{ cm}^{-3}$ ,  $K \approx 40 \text{ keV cm}^2$  assuming constant density for a prolate spheroid with symmetry axis in the sky plane, or  $n_H = 8 \times 10^{-3} \text{ cm}^{-3}$ ,  $K \approx 60 \text{ keV cm}^2$  for an oblate spheroid instead.

The entropy estimates vary by a factor of 2 for the different geometries (elongated vs. cap-like) but are not drastically different. Since the specific entropy could only have increased in the process of merger disruption (e.g., via mild shock heating), such specific entropy values, along with the high gas densities, put these gas clumps confidently in the parameter space of the central core regions of cool-core clusters where typically  $K \sim 15 \text{ keV cm}^2$  as opposed to non-cool-core clusters where  $K \sim 150 \text{ keV cm}^2$  (Cavagnolo et al. 2009). Thus, the cold gas “leg” indeed appears to be a trail of pieces of a merger-

disrupted cool core being swept by the gas flows. We will use this conclusion in § 2.5.4.

### 2.4.3 Splashes, bumps and islands

The eastward extension of the leg curves to the SE after about 300 kpc, and ends with a steep brightness drop (“splash A” in Fig. 2.2*b*) not far beyond. The gas at the dense side of the brightness drop appears to be cooler than the surroundings, including the gas along this structure but closer to the center. While the projected temperature in region G3 (which contains the tip of the splash) is only marginally lower than in regions G2, G1 in Fig. 2.5, and the temperature in region G4 in front of the splash is poorly constrained, the temperature contrast becomes quite pronounced in the wavelet temperature map in Fig. 2.3*b*. This splash looks like a hydrodynamic feature caused by “ram pressure slingshot” (Hallman & Markevitch 2004), in which a rapid decline of ram pressure in a merger causes a parcel of gas to move into the less-dense gas and expand adiabatically, forming a cool spot. In this case, it could be one of the low-entropy clumps remaining of the cool core and forming the cool leg.

North of the cluster center there is another hydrodynamic structure of likely similar origin (“splash B” in Fig. 2.2*b*; also region T5 in Fig. 2.3). The surface brightness structure is picked out by wavelet decomposition, which can be seen in the original image to appear like a pointed stream of gas. The temperature maps indicate that this region is cool. The gas there is not necessarily related to the cool core, as it is quite far and across the cluster from the cool core remnants.

There is a subtle brightness island extending further SE from splash A, marked “island D” in Fig. 2.2 and Fig. 2.3, whose origin is unclear. Its projected temperature is

not well constrained but does not rule out a cool structure.

Another splash-like structure (“bump C” in Fig. 2.2b) is located symmetrically opposite splash B about the merger axis. Unlike splashes A and B and island D, it coincides with one of the weak-lensing mass clumps. Its projected temperature is in line with the cluster average and may even be higher (as suggested by the wavelet map). This bump may have an entirely different origin, a subcluster adiabatically accreting gas, similar to the feature that we will discuss in § 2.5.3.

## 2.5 Discussion

### 2.5.1 Scene of a ‘train wreck’

The detail-rich *Chandra* X-ray image and gas temperature maps of A520, especially the map in which we subtracted the large-scale cluster emission using wavelet transformation, tell a complex story about the events in this merging cluster. From the X-ray and weak lensing data, we see a major merger proceeding mostly along the NE-SW axis (Fig. 2.2c). The NE chain of subclusters have apparently moved away from the collision site, completely stripped of their gas and currently hosting only low-level bumps of X-ray emission (we will discuss this in detail in § 2.5.3). The SW subcluster is also moving away from the cluster center, driving a prominent shock front. Apparently, this subcluster had a cool core, which is now being stripped by ram pressure, leaving a trail of cool clumps — “foot”, “knee” and “leg”. The meandering shape of this trail, its ending with splashes A and D, together with several other signs of complex hydrodynamics such as the kink in the shock surface, the “plume” next to it and “splash B” (Fig. 2.2), suggest a secondary

collision along the north-south direction. A curious X-ray “channel”, possibly resulting from this secondary merger, will be discussed in § 2.5.2. The full history and details of this “train wreck” of a cluster may be understood better with a dedicated hydrodynamic simulation. However, already our present broad-brush understanding of the A520 merger lets us make three measurements that are interesting from the cluster physics viewpoint.

### 2.5.2 X-ray channel

A close look at the X-ray image (in particular, Fig. 2.4a, which show the image with different bin sizes, and Fig. 2.2d, which shows an “unsharp-masked” image), reveals a subtle, long X-ray brightness “channel”. It aligns with the direction of the secondary merger that we mentioned above, running from the “plume” in the south through the central region of the cluster toward “splash B” in the north (Fig. 2.2). We selected a sector in which this channel is most apparent and which excludes any interfering features such as the leg, as shown in Fig. 2.4a. An X-ray brightness profile across the channel extracted in this sector is shown in Fig. 2.6. It confirms a highly significant  $\sim 10 - 12\%$  drop in X-ray surface brightness. The channel is about 30 kpc (9”) wide and at least 200 kpc long, which is its length within the profile sector, though the channel clearly extends beyond it and can be traced as an X-ray dip in the leg and plume in the south, and similarly further to the north.

The channel has to be a relatively thin sheet of lower-density gas seen along the edge. If we assume a rough spherical symmetry of the main cluster body, and assume that the channel is completely devoid of gas in 3D, the sheet’s extent along the l.o.s. would have to be  $\sim 75$  kpc to give the observed projected X-ray brightness drop. Since it cannot

be completely empty, the extent should be significantly greater.

It is interesting to speculate on the origin of the X-ray channel. First, we note that X-ray “cavities” filled with radio emission are routinely observed in cluster cool cores (e.g. [McNamara et al. 2000](#); [Fabian et al. 2002](#), and later works); they are created by outbursts of the central AGN, where the ejected relativistic matter expands and pushes the thermal gas away.

However, the channel/filament in A520 is not in a cool core, and its 500 – 700 kpc size is far greater than any of the cavities seen in cluster cores. In principle, if in a certain region the magnetic field pressure reaches levels comparable to the thermal pressure of the ICM, it may push the plasma away from this region, in a manner similar to “plasma depletion layers” observed near planets (e.g., [Øieroset et al. 2004](#)) and features seen in the galaxy cluster context in MHD simulations by [ZuHone et al. \(2011\)](#) (see their Fig. 23, reproduced in [Fig. 1.4](#)). Such a phenomenon may have recently been observed by [Werner et al. \(2016a\)](#) in the core of the Virgo cluster (though they observed X-ray enhancements rather than depletion regions).

In such a scenario, the sum of thermal and magnetic pressure inside the channel would equal the thermal pressure outside (assuming the magnetic pressure outside to be negligible, as expected for the bulk of the ICM). Neglecting projection effects — that is, assuming the channel to be a broad sheet spanning the whole cluster along the l.o.s. — the observed drop in X-ray brightness would correspond to a drop in gas density by 5 – 6% and a drop in thermal pressure by 5 – 15% depending on the temperature behavior. Such a drop of thermal pressure would imply a plasma  $\beta_p$  parameter ( $\beta_p \equiv p_{\text{thermal}}/p_B$ ) reaching 10–20, compared to the usual  $\beta_p \sim \text{few} \times 100$ . In a high- $B$  filament seen in simulations

by [ZuHone et al.](#), both density and temperature of the gas decline by similar factors, so the temperature is likely to decline in this scenario.

Alternatively, the channel may be a purely hydrodynamic feature — for example, a region of shock-heated gas currently in thermal pressure equilibrium, which has been squeezed into a sheet by gas flows. In this case, the temperature in the channel should be higher by at least 5% than that on the outside.

To test these two possibilities, we extracted a projected temperature profile in the same sector across the channel ([Fig. 2.6](#)). It does not show any significant temperature changes from the regions outside the channel, but a 10% deviation in either direction cannot be excluded. Thus, both possibilities are viable on the basis of the X-ray data. If the channel's span along the l.o.s. is less than assumed above, the 3D density and temperature contrast may be higher (and the magnetic field in the first scenario higher, too), but the projected surrounding denser gas would still make it difficult to detect any temperature difference.

Both of the above configurations may have emerged as a result of a minor merger along the north-south direction. For example, a small subcluster infalling from the south (to explain the kink in the shock surface) and crossing the main cluster could have stretched the magnetic fields in its wake, and/or generated a shock-heated region. Subsequently, this region could have been squeezed into a sheet — for example, by large-scale gas motions of the main NE-SW merger. One can also think of a radio-filled X-ray cavity swept off one of the merging cluster cores, stretched by a N-S merger and compressed into a sheet. It is unclear where that subcluster is now in the lensing mass map (it may be clump N in [Okabe & Umetsu 2008](#), which is not, however, a particularly significant feature in [Clowe](#)

et al. 2012), or how a low-density, unstable gas sheet could have survived as a coherent structure in the middle of an ongoing merger. Such details might be clarified by a dedicated hydrodynamic simulation. In all of the above scenarios, we expect the magnetic field in the channel to be enhanced and oriented preferentially along the channel (because of stretching and compression). This may produce a bright filament in the cluster's giant radio halo (Govoni et al. 2001; Vacca et al. 2014), because the synchrotron radio emissivity is proportional to  $B^2$ , and that filament would be polarized. Giant radio halos are unpolarized (Feretti et al. 2012), so this would be a notable feature. The currently available radio data lack angular resolution to test this prediction (Chapter 3; Wang et al. 2018).

### 2.5.3 Dark subclusters in the northeast

A520 exhibits a low X-ray brightness, relatively narrow tail, a subtle feature but clearly visible out to about 1.3 Mpc northeast from the cluster center (Fig. 2.2; seen more clearly in a heavily-binned image in Fig. 2.7). It has two broad X-ray peaks, each of which coincides with a mass clump seen in the weak lensing map (Fig. 2.7). The tail and the clumps are aligned in the NE-SW direction of the main merger. The outermost clump, centered 1.2 Mpc from the cluster center and approximately 0.5 Mpc in diameter, is particularly interesting, because it is relatively free of projection of the rest of the messy cluster, which lets us make several quantitative measurements.

Only two *Chandra* pointings (ObsIDs 9425, 9526) captured the tail, for an effective exposure of about 200 ks. Spectra extracted from regions C1 and C2, which approximately include the outer and inner of the two tail clumps, respectively, show that they are

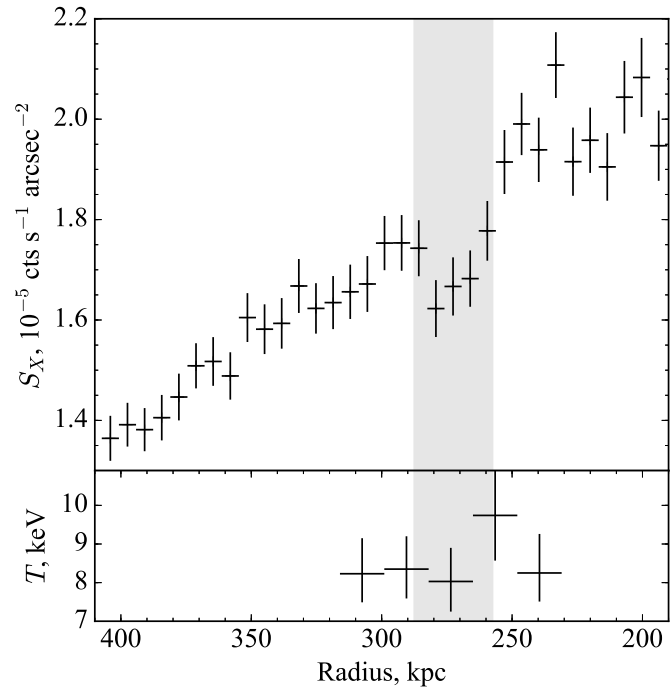


Figure 2.6: Radial profiles extracted in the annular sector in Fig. 2.4a, of X-ray surface brightness (upper panel) and gas temperature (lower panel). The grey band is 30 kpc wide centered on the location of the channel, marked by white ticks in the profile extraction sector. Error bars for X-ray brightness and temperature are  $1\sigma$ . Radial distance is from the center of curvature of the sector.

both hot, with the outer tail clump (C1) being slightly hotter than the inner (Fig. 2.5).

The tail mass peaks are visible in two independent datasets, Subaru (see Fig. 11 in Okabe & Umetsu 2008) and Magellan (Clowe et al. 2012). In the latter paper, only the inner tail peak is shown (peak 1 in Fig. 2.1); the outer, less significant peak is not shown because it was outside the HST FOV, but it is seen in the uncropped version of the map provided by D. Clowe, which we show in Fig. 2.2 and Fig. 2.7. The Subaru map covers a bigger field than Magellan or *Chandra* and reveals another clump (their clump NE1) still further to the northeast, but the Subaru map does not resolve these two Magellan tail clumps, showing them as one (NE2). For the quite substantial mass of the tail clumps suggested by lensing, not much gas can be seen in the *Chandra* image, and not much galaxy light is seen in the Subaru *i'*-band image either — in particular in the outer tail clump (Fig. 11c in Okabe & Umetsu). This is interesting in view of the debated “dark core” in the center of A520, where there is a lack of galaxies while there has been conflicting results on the presence of a dark matter clump (Clowe et al. 2012; Jee et al. 2012). These clumps may be even “darker” and we will try to quantify the X-ray gas fraction below.

We will now concentrate on the outer tail clump, because it is least affected by X-ray projection. (The inner tail clump is more significant in the lensing map, but it is hopeless to deproject it in X-rays.) We will compare the specific entropy of the gas in the clump with that for the main cluster gas at the same distance from the cluster center, estimate the clump total mass under the hydrostatic equilibrium assumption, and derive a gas-to-mass ratio for the clump.

### 2.5.3.1 Specific entropy of the clump

To derive the gas density, we fit the heavily-binned X-ray image (Fig. 2.7) with a simple model consisting of two spherically-symmetric 3D  $\beta$ -model density profiles — one for the clump and another for the main cluster outskirts near the radius of the clump. The  $\beta$ -model profile is given by

$$n_{\text{H}}(r) = n_{\text{H},0} \left[ 1 + \left( \frac{r}{r_c} \right)^2 \right]^{-3\beta/2} \quad (2.2)$$

where  $r_c$ ,  $n_{\text{H},0}$  and  $\beta$  are free parameters. Integrating  $n_{\text{H}}^2$  along the l.o.s. gives an observed X-ray surface brightness profile (more precisely, the projected emission measure, which is very close to the surface brightness for the relevant range of gas temperatures and the *Chandra* energy band) in the form

$$\Sigma_X(\theta) \propto \left[ 1 + \left( \frac{d_A \theta}{r_c} \right)^2 \right]^{-3\beta+1/2}, \quad (2.3)$$

where  $d_A$  is the angular diameter distance and  $\theta$  the angular distance from center.

For the cluster outskirts, we extracted a 0.8–4 keV radial surface brightness profile in an annulus around the same distance from the cluster center as the clump, with prominent asymmetric features (tail including the clump, foot, shock, splashes) masked out as shown in Fig. 2.7. It is not obvious where the “center” of a messy merger is; for this exercise, the center is selected as a centroid of the X-ray emission at the relevant radii in the outskirts. We fit the profile in this annulus using a model given by Eq. 2.3, fixing the core radius  $r_c$  at a typical value of 180 kpc (since we fit very far from the core). To

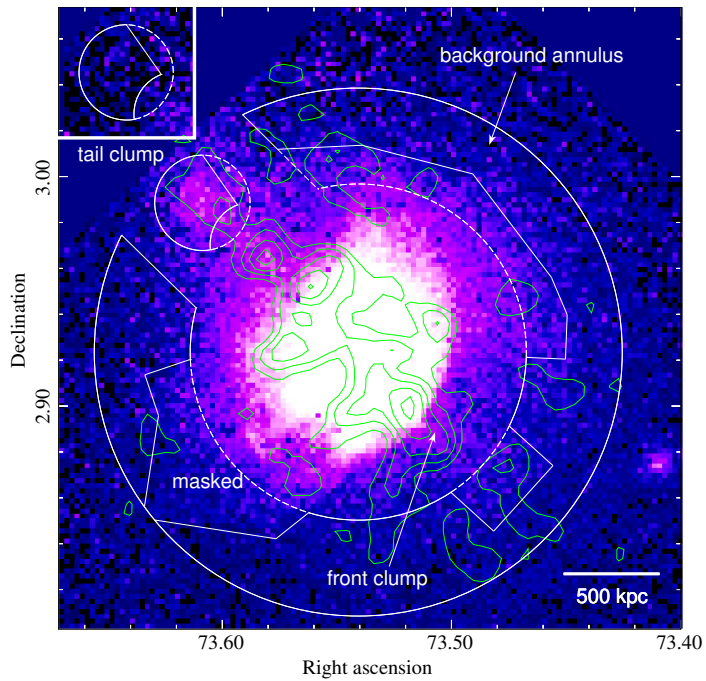


Figure 2.7: The tail clump and background regions shown on the 0.8–4 keV image binned to 8'' pixels. Regions bounded by dashed lines were masked. Contours are lensing mass from D. Clowe. The top left inset shows the residual image after subtracting the clump and outskirts models (same color scale).

determine the normalization  $n_{\text{H},0}$ , we extracted a spectrum in the same region, fit it in XSPEC using APEC model, and compared the model emission measure integrated over the region  $\int n_{\text{H}}n_e dV$  with the absolute APEC model normalization given by XSPEC. The best-fit projected temperature is  $T = 4.1_{-0.9}^{+1.4}$  keV, and the beta-model parameters are  $\beta = 0.62_{-0.05}^{+0.04}$  and  $n_{\text{H},0} = (4.4_{-1.0}^{+1.2}) \times 10^{-3} \text{ cm}^{-3}$ . At the clump's radius, the outskirts density is  $n_{\text{H}} = (1.3 \pm 0.1) \times 10^{-4} \text{ cm}^{-3}$  (density in the outskirts is better constrained than the beta-model normalization, which is an extrapolation of the profile in the outskirts).

The clump density model was then fitted in 2D (that is, pixel-by-pixel, as opposed to extracting a radial profile), because the cluster outskirts contribution makes the surface brightness distribution non-radial. We added a  $\beta$ -model density component for the clump to the density model for the outskirts, fixing the latter at its best fit derived above (which masked out the clump region with a good margin). We chose to add the clump density component, rather than replacing one with the other in the 3D region of the clump, to avoid any smoothness issues for the hydrostatic mass estimates; this choice does not matter as long as the model fits the X-ray image well. The sum of the two density components was calculated in 3D and a projected emission measure was calculated for each pixel of the X-ray image in a masked near-circular region of  $r = 250$  kpc (Fig. 2.7). The best-fit shape parameters for the clump are  $\beta = 0.80 \pm 0.07$  and  $r_c = 203_{-16}^{+20}$  kpc (uncertainties determined with the other parameter fixed at best-fit value) and the model fits the image well ( $\chi^2 = 135/199 = 0.68$ ).

To derive the absolute gas density in the clump, we need the gas temperature. If we assume the clump to be isothermal with the outskirts, its density normalization can be derived directly from the X-ray surface brightness and the outskirts model derived above.

This gives a density of  $n_{\text{H}} = (1.0 \pm 0.1) \times 10^{-3} \text{ cm}^{-3}$  at the clump, of which the clump component dominates the outskirts component by a factor of 7 — a significant gas overdensity.

However, the clump appears to have a higher projected temperature than the outskirts,  $T = 8.1_{-1.9}^{+3.6} \text{ keV}$  (for region C1 in Fig. 2.5, which covers the clump), and its 3D temperature should be higher still. Therefore, we also consider the case in which an isothermal, but hotter, clump is embedded in the outskirts. We make a simple assumption that all gas within a  $r = 250 \text{ kpc}$  sphere of the clump is at a higher temperature. We generate a model image with a cutout for this sphere and calculate the projected contribution of the 4 keV outskirts to the clump spectrum (it is about 9% in projected emission measure at the center of the clump). Adding this as a “background” model for the spectrum of the clump, we obtain a “deprojected” clump temperature  $T = 9.7_{-3.3}^{+5.5} \text{ keV}$ , which is slightly higher but consistent with the projected temperature (as expected, given the relatively high brightness contrast) and the density at the center of the clump increased by 10% to  $n_{\text{H}} \approx 1.1 \times 10^{-3} \text{ cm}^{-3}$  compared to the isothermal assumption — a negligible change for our qualitative estimates, and considering the systematic uncertainties due to the unknown geometry.

Using the deprojected temperature and density for the clump, we can estimate the specific entropy of the gas at its center, defined as in Eq. 2.1,  $K = 930_{-320}^{+510} \text{ keV cm}^2$  (error accounts only for the uncertainty in temperature). For comparison, the gas in the outskirts has  $K = 1540_{-340}^{+530} \text{ keV cm}^2$  at this radius. The two values are consistent, and both are consistent with the entropy range  $(1 - 2) \times 10^3 \text{ keV cm}^2$  observed at  $r \sim 1 - 1.3 \text{ Mpc}$  for a large sample of clusters (Cavagnolo et al. 2009). The temperature and density of

the gas in the clump are consistent with adiabatic compression of the 4 keV gas from the outskirts perturbed by the gravitational attraction of the clump. In contrast, for cool cores, [Cavagnolo et al.](#) observe  $K < 50 \text{ keV cm}^2$ , far below the observed value for the clump, so this gas cannot be a remnant of a former cool core (like the “foot”, § 2.4.2). We will speculate on the sequence of events that could have created this clump after estimating its mass below.

### 2.5.3.2 Total mass of the “dark clump” and its possible origin

Given the relative isolation of the tail clump, we can try to estimate its total mass, assuming that its hot gas is close to hydrostatic equilibrium with the clump’s gravitational potential. The equilibrium should be achieved on a timescale of sound crossing the size of the subcluster. Considering that the subcluster is unlikely to move supersonically at such a distance from the core (we also do not see any shocks around it), this assumption should be adequate for a qualitative estimate.

The total enclosed mass within the radius  $r$  for a spherical mass clump is given by (e.g., [Sarazin 1988](#))

$$M(< r) = -\frac{kT(r)r}{G\mu m_p} \left[ \frac{d \ln n_H}{d \ln r} + \frac{d \ln T}{d \ln r} \right], \quad (2.4)$$

where  $\mu$  is the mean atomic mass per gas particle ( $\mu \approx 0.6$  for ICM),  $T(r)$  is the local gas temperature at the radius  $r$  and  $n_H$  is the gas density, which is the sum of the clump and outskirt density models in our case. For an accurate estimate, a temperature profile is required, for which our data are not adequate — all we know is that the temperature

near the clump center is around 10 keV and it goes down to 4 keV in the main cluster's outskirts. Therefore, we will make two isothermal estimates for these two temperature values to get a rough range of masses. (The higher-temperature estimate would neglect the  $(d \ln T / d \ln r)$  contribution, which should be nonzero in this case, partially canceling out the effect of the expected lower local  $T$  at the radius of the estimate.) For the gas density gradient, we will use the best-fit model (sum of offset 3D beta-models) obtained above, calculating the gradient in the direction tangential to the main cluster in order to isolate the effect of the clump. We will calculate the mass for a radius well within our model fit above. Within a  $r = 200$  kpc sphere, we obtain the total mass of  $2.5 \times 10^{13} M_{\odot}$  and  $6 \times 10^{13} M_{\odot}$  for the lower and higher temperature values, respectively (of course, statistical errors do not matter with such a modeling uncertainty). This is consistent with masses within the same radius derived for real mid-temperature clusters (e.g., [Vikhlinin et al. 2006](#)).

To assess the sensitivity of the clump hydrostatic mass estimate to our assumption of spherical symmetry for the main cluster's outskirts, we varied the surface brightness of the outskirts by factor  $\pm 2$  in the region of the clump and refitted the density model for the clump. The resulting variations in the quantity  $d \log n_{\text{H}} / d \log r$  (where  $n_{\text{H}}$  is the sum of the clump and outskirts components, and  $r$  is the distance from the center of the clump), which determines the clump mass estimate, varies by at most 40% in the radial range of interest. Thus, our estimate should be relatively robust to geometric assumptions.

It is interesting to compare our mass estimate with a weak lensing mass for this clump. D. Clowe (private communication) provided us with an estimate of a projected mass within a cylinder of  $r = 150$  kpc. Depending on whether the HST data (partially

covering the clump) are included in the reconstruction along with the Magellan data, the projected mass is  $(1.7 - 2.3) \times 10^{13} M_{\odot}$ ; the statistical significance of this clump detection is only  $2-3\sigma$ . To convert our 3D measurement into a projected mass, we assume that the clump’s total mass profile is truncated at  $r = 300$  kpc. For the low and high temperatures, we obtain the projected masses within the  $r = 150$  kpc aperture of  $2.4 \times 10^{13} M_{\odot}$  and  $5.6 \times 10^{13} M_{\odot}$ , respectively. The lower range of our X-ray estimates is in agreement with the lensing value.

With this qualitative validation for our mass estimate, we now estimate the gas mass fraction  $f_{\text{gas}}$  for the clump. Within the  $r = 200$  kpc sphere, we get  $f_{\text{gas}} = 0.03$  and  $0.014$  for the cool and hot clump assumptions, respectively. This is low — even the former, conservatively high value is at least a factor 2 below the  $f_{\text{gas}}$  values observed within the same radius in relaxed clusters (e.g., [Vikhlinin et al. 2006](#)). So the tail clump appears to be “dark” in terms of the apparent deficit of both the galaxy light and the ICM density. The caveat here is the uncertainty in the total mass is quite high, and one cannot be entirely confident in the X-ray hydrostatic equilibrium assumption here; a more sensitive weak lensing observation may reduce the total mass and  $f_{\text{gas}}$  uncertainty.

Based on the high specific entropy that we derived in § 2.5.3.1 (consistent with that in the A520 outskirts), a cluster-like total mass and an anomalously low gas fraction, we speculate that this clump entered the collision site from the SW as a fairly massive sub-cluster. It then lost most of its gas to ram pressure stripping (and probably all matter in its outskirts to tidal stripping) during the passage through the main cluster, but re-accreted some high-entropy gas from the A520 outskirts once it emerged on the other side. The gas compressed adiabatically into its potential well once the subcluster slowed down suf-

ficiently. Of course, the resulting  $f_{\text{gas}}$  need not be anywhere near the universal value. On subsequent infall, such a subcluster would be the analog of the dark-matter dominated “gasless” subclusters used in idealized hydrodynamic simulations (e.g., [Ascasibar & Markevitch 2006](#); [ZuHone et al. 2010](#)), which disturb the gravitational potential but produce few hydrodynamic effects.

Judging from the X-ray/lensing overlay, the more prominent inner-tail lensing mass peak (clump 1 in [Fig. 2.1](#), from [Clowe et al. 2012](#)) appears to have a similar or even lower gas-to-mass ratio (the peak X-ray brightness is similar and the lensing mass is higher). We did not attempt any quantitative X-ray estimates for this clump because the 3D geometry is very uncertain.

We also note that the mass clump that hosted the stripped cool core, denoted “front clump” in [Fig. 2.7](#), appears to be reaccreting or concentrating the surrounding hotter gas. It is seen as an enhancement in density of the preshock gas at the position of the clump. Although this subcluster appears to be more massive than the tail clump, its gas density enhancement is smaller, probably because the gas is flowing over this dip in the gravitational potential toward the shock front with a higher velocity. As this subcluster moves to the periphery and slows down with respect to the gas, it may re-accrete a gas halo similar to that of the tail clump.

Interestingly, [Sasaki et al. \(2015\)](#) observed three massive weak-lensing subhalos in the periphery of the Coma cluster with *Suzaku*. One of their subhalos exhibits a diffuse X-ray emission excess with the projected gas temperature similar to that of the surrounding ICM. They derive an extremely low gas fraction of  $\sim 0.001$  for it. These subhalos may be of similar nature to our dark clump — complete stripping of the original gas and

subsequent reaccretion of the surrounding ICM.

#### 2.5.4 Constraints on thermal conduction

In our picture of A520, the cool clumps in the “leg” (from the “foot” to the “knee”, then east along the bright ridge) come from the same cool core (§ 2.4.2), so their magnetic field structure should be (a) interconnected and (b) stretched along the trail by the same gas motions that separated the cool core pieces. This offers a unique opportunity to constrain the conductivity *along* the field lines. We know the Mach number of the shock front and the velocity of the post-shock flow (M05), which lets us estimate how long ago they were stripped based on their distance along the trail. We can then determine if the conductivity between them should be suppressed by comparing the Spitzer conduction timescale with their age,

$$\kappa/\kappa_S = (t_{age}/t_{cond})^{-1}. \quad (2.5)$$

In our simple picture, the “foot” is the last piece of the former cool core that is still gravitationally bound to the subcluster that drives the shock (or, at least, it has been bound until recently). The post-shock gas flow peels away pieces of the cool core, carrying them off at the downstream velocity of  $1000 \text{ km s}^{-1}$  (M05). Guided by the temperature map (Fig. 2.4b), we picked two pairs of circular regions in near contact (in projection) that have large and significant temperature differences. The blobs are assumed to attain their present temperature and spatial separation upon stripping from the core, and then to move with the flow together; the distance of the pair from the “foot” along the “leg” gives the age of the pair.

We estimated the thermal conduction timescale as in, e.g., [Markevitch et al. \(2003b\)](#):

$$t_{\text{cond}} \approx 1.2 \times 10^7 \left( \frac{n_e}{2 \times 10^{-3} \text{ cm}^{-3}} \right) \left( \frac{l_T}{100 \text{ kpc}} \right)^2 \left( \frac{T}{10 \text{ keV}} \right)^{-5/2} \text{ yr}, \quad (2.6)$$

where  $n_e$  is the electron number density,  $l_T \equiv T/|\nabla T|$  is the thermal gradient scale length, and  $T$  is the electron temperature. This equation applies when the heat flux is unsaturated — where  $l_T \gg \lambda_e$ , the electron mean free path ([Spitzer 1956](#)):

$$\lambda_e \approx 31 \text{ kpc} \left( \frac{kT}{10 \text{ keV}} \right)^2 \left( \frac{n_e}{10^{-3} \text{ cm}^{-3}} \right)^{-1}. \quad (2.7)$$

Based on this, the regions we selected are far from the saturated heat flux regime. The density in [Eq. 2.6](#) is taken to be the average density in the corresponding stretch of the leg,  $n_H = 0.01 \text{ cm}^{-3}$ . This is uncertain to a factor 2, based on density estimates for each region using two different geometric assumptions — all emission originating from a sphere in projection (leading to higher densities and therefore longer  $t_{\text{cond}}$ ), or from cylinder along the l.o.s. that is 400 kpc long (the opposite effect). Therefore our values of  $\kappa_S/\kappa$  also has a factor of 2 uncertainty arising from this.

We also consider how the uncertainty in  $l_T$  affect our results. Since  $t_{\text{cond}} \sim l_T^2$ , it is important to estimate the gradient correctly. For one set of estimates, we use the projected temperatures in the regions of interest, measured using XSPEC. However, projection is likely to wash out the temperature gradient, resulting in longer  $l_T$ . While our wavelet temperature map ([§ 2.3.2](#)) is qualitative, it removes most of the projection effects and

leaves only the relevant linear scales. Fig. 2.4b shows a temperature map created with only the smallest wavelet components that correspond to the angular scale of the structures in the leg. Using the temperature values from this map, the values of  $T/\Delta T$  are up to 2 times smaller. We note that since we calculate the gradients using projected distances between the regions, this is a lower limit for  $l_T$ . On the other hand, the leg may be bent along the l.o.s., so our ages for the region pairs may be underestimated. And of course, the absence of a temperature gradient does not always result from thermal conduction, so we can only place a lower limit for an order-of-magnitude estimate of a suppression factor.

The results are shown in Table 2.1. For regions 1 and 2 (see Fig. 2.4b), we cannot say whether the conduction is suppressed — the suppression factor is consistent with 1 for both the projected or deprojected temperatures. For regions 3 and 4,  $\kappa_S/\kappa \sim (3.3 - 11)$ , so there seems to be some suppression.

We did not use splash A at the end of the cool trail for this estimate, even though there appears to be a significant temperature gradient there. The splash should have been cooling via adiabatic expansion as it formed, so its age is very uncertain.

The above attempted constraints for the suppression *along* the field lines can be contrasted with thermal conductivity across the edge of the cool trail of gas. In our scheme for A520, the cool trail should be isolated from the surrounding gas by a magnetic field stretched along its boundary (a likely analog of the infalling group in Eckert et al. 2012). For example, consider the feature marked ‘edge’ in Fig. 2.4b. Along this trail of cool gas the temperature gradient is small, but in the perpendicular direction it jumps from about 4.5 keV in the leg to 12 keV for the post-shock gas on a scale smaller than 10 kpc. The surface brightness jump there is unresolved by *Chandra* (Fig. 2.8). The trail is 120 kpc

Table 2.1: Thermal conduction timescale estimates using adjacent pieces of the stripped cool core remnant. The columns are: estimated age of the feature in yr; projected temperatures in keV; suppression factor ( $\kappa_S/\kappa = t_{\text{age}}/t_{\text{cond}}$ ) using projected temperatures; deprojected temperatures from the wavelet temperature map; suppression factor using deprojected temperatures.

Reg	$t_{\text{age}}, \text{yr}$	$T_1^{\text{proj}}$	$T_2^{\text{proj}}$	$\kappa_S/\kappa^{\text{proj}}$	$T_1^{\text{dep}}$	$T_2^{\text{dep}}$	$\kappa_S/\kappa^{\text{dep}}$
1, 2	$1.9 \times 10^8$	5.2	7.4	1.1	4.5	7	1.4
3, 4	$2.6 \times 10^8$	7.4	11.9	3.3	6	14	11

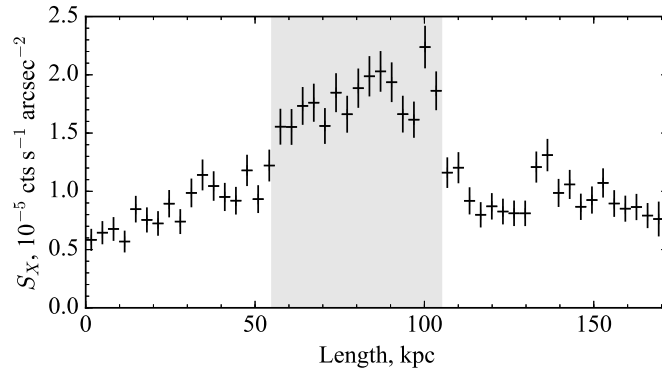


Figure 2.8: Surface brightness profile across the cool trail just above the foot, extracted in a narrow rectangular region (Fig. 2.4a), showing an unresolved edge at around 105 kpc. The cool trail spans the shaded region between 55 and 105 kpc. The small bump between 130 and 150 kpc is due to the tip of the foot.

long, implying an age of  $1.2 \times 10^8$  yr from the cool core at the downstream velocity. The density inside the trail is estimated from the emission measure in the same region (assuming cylindrical shape) to be  $6 \times 10^{-3} \text{ cm}^{-3}$ . For these values,  $\lambda_e = 3.5$  kpc, so this is still in the unsaturated conduction regime. We find  $t_{cond} = 7 \times 10^5$  yr, implying a large suppression factor,  $(\kappa/\kappa_S)^{-1} \gtrsim 170$ . Thus, this trail could not have sustained its sharp boundary over its physical scale in the presence of any significant thermal conduction across the edge.

## 2.6 Summary

The deep *Chandra* exposure of Abell 520 revealed rich structure in this cluster train wreck, including a prominent bow shock. Some of these structures provide interesting constraints on cluster physics. We derived detailed gas temperature maps using two methods, one that utilizes variable-width smoothing and evaluates the projected temperature, and another that uses wavelet decomposition to “deproject” the large-scale structure in a qualitative way and enhance the contrast of the interesting small-scale structure.

On small scales, A520 exhibits an apparent disrupted cool core at a unique evolutionary stage — the gas of the core is swept away from the central galaxy of its former host subcluster by ram pressure of the gas flow downstream of the shock front, completely displacing the gas peak from the galaxy (by 50–70 kpc). The disrupted core is not mixed with the hot gas but still forms a physically connected trail of dense clumps (a cool “leg”). Its twisted structure apparently reflects the chaotic gas velocities in this region. The core remnant in A520 is at a later stage of disruption compared to the bullet in the Bullet clus-

ter, where it is still seen as a regular shuttlecock structure. The specific entropy of the gas in the clumps is much lower than elsewhere in the cluster and is typical of other cool cores.

In the above scenario, the magnetic field within the leg should be stretched along the leg and still connect the clumps (since they come from the same core), while insulating the leg from the surrounding hot gas. We use the observed temperature variations between the cool leg and the surrounding gas, and within the leg, to constrain thermal conductivity across the field lines (a factor  $> 100$  suppression from the Spitzer value) and, for the first time, suggest that the conductivity along the lines may also be suppressed by a factor of at least several. This is, of course, dependent on our assumption about the magnetic field structure.

About 1.3 Mpc northeast of the cluster center, the X-ray image reveals a subtle tail of low X-ray brightness. Two clumps in the tail coincide with mass peaks seen in the weak lensing mass map. For one of the clumps that is least affected by projection, we derived a specific entropy of the X-ray gas, which turns out to be similar to the high value for the cluster gas at that radius, while the gas density in the clump is several times higher. Thus, the X-ray enhancement at that clump appears to be due to adiabatic compression of the surrounding gas. The second clump looks similar, though quantitative estimates are difficult because of projection. It appears that these clumps have passed through the cluster merger site and lost all of their gas (or, alternatively, arrived to the cluster already gasless) and then re-accreted the surrounding outskirts gas as soon as they slowed down sufficiently. An X-ray hydrostatic estimate the total mass of the clump is consistent with the lensing mass. The ratio of the X-ray measured gas mass to total mass is 1.5–

3%, much lower than the typical average cluster value, making these clumps truly “dark subclusters”. Of course, considering our scenario for their origin with stripping and re-accretion, it would have to be a coincidence if the resulting gas fraction ended up the same as the universal cluster value.

Finally, we found a curious long ( $> 200$  kpc), narrow (30 kpc or  $9''$ ) X-ray “channel”, going across the bright cluster region along the direction of an apparent secondary merger. The projected X-ray brightness in the channel is 10–12% lower than in the adjacent regions. The channel has to be a sheet spanning at least 75 kpc along the l.o.s. It is possible that this is a “plasma depletion layer” with the magnetic field stretched and enhanced by the merger; the plasma  $\beta$  parameter should reach 10–20 in the sheet. In this scenario, we predict that the channel will be seen as a bright filament in the radio image of sufficient angular resolution, and the filament will be polarized.

## CHAPTER 3

---

### Bow shock in merging cluster Abell 520 — The edge of the radio halo and The electron–ion equilibration timescale

*This chapter has been adapted from the published version in *The Astrophysical Journal*, Vol. 856, p. 162 (Wang et al. 2018).*

We studied the prominent bow shock in the merging galaxy cluster A520 using a deep *Chandra* X-ray observation and archival *VLA* radio data. This shock is a useful diagnostic tool, owing to its clear geometry and relatively high Mach number. At the “nose” of the shock, we measure a Mach number of  $M = 2.4^{+0.4}_{-0.2}$ . The shock becomes oblique away from the merger axis, with the Mach number falling to  $\approx 1.6$  around  $30^\circ$  from the nose. The electron temperature immediately behind the shock nose is consistent with that from the Rankine-Hugoniot adiabat, and is higher (at a 95% confidence) than expected for adiabatic compression of electrons followed by Coulomb electron–proton equilibration, indicating the presence of equilibration mechanisms faster than Coulomb collisions. This is similar to an earlier finding for the Bullet cluster. We also combined four archival *VLA* datasets to obtain a better image of the cluster’s giant radio halo at 1.4 GHz. An

abrupt edge of the radio halo traces the shock front, and no emission is detected in the pre-shock region. If the radio edge were due only to adiabatic compression of relativistic electrons in pre-shock plasma, we would expect a pre-shock radio emission detectable in this radio dataset; however, an interferometric artifact dominates the uncertainty, so we cannot rule this model out. Other interesting features of the radio halo include a peak at the remnant of the cool core, suggesting that the core used to have a radio minihalo, and a peak marking a possible region of high turbulence.

### 3.1 Introduction

The test for the electron–ion equilibration timescale requires a simple, reasonably unambiguous shock geometry and a high-statistics, high-resolution X-ray dataset in order to derive a 3D temperature jump at the shock. After the Bullet cluster result, [Russell et al. \(2012, hereafter R12\)](#) examined two other merger shocks that fit these requirements, those in A2146, but their results were inconclusive because of large uncertainties and the low Mach number of one of the shocks (the difference between shock heating and adiabatic heating of electrons becomes practically undetectable for  $M \lesssim 2$ ). A deep *Chandra* observation of A520, which we have analyzed in [Chapter 2 \(Wang et al. 2016, hereafter W16\)](#) for everything else other than the shock front, presents another one of those rare opportunities. We will describe this test in [§ 3.4.2](#).

A520 exhibits a giant radio halo detected by the Very Large Array (VLA; [Govoni et al. 2001; Vacca et al. 2014](#)), whose distinct brightness edge coincides with the X-ray shock front ([Markevitch et al. 2005, hereafter M05](#)), similar to several other clusters with shock fronts (e.g., [Giacintucci et al. 2008; Markevitch 2012; Planck Collaboration et al.](#)

2013; Shimwell et al. 2014). The previous analyses of the A520 radio halo used two subsets of *VLA* data separately, which limited the sensitivity both because of the partial statistical accuracy and the limited coverage of the Fourier space (the  $uv$  plane) by the antennas during a typical *VLA* observation, which may lead to lower reconstructed image fidelity. To take full advantage of the existing radio data, we combine all archival *VLA* observations in § 3.3. We revisit the earlier finding of the coincidence of the radio halo edge and the X-ray shock front. We use the improved radio sensitivity to put an upper limit on the radio emission in the pre-shock region and test one of the possible mechanisms for the origin of the radio edge considered in M05 — adiabatic compression of pre-existing relativistic electrons. There are other illuminating coincidences between the radio and X-ray structure of the cluster that we discuss in § 3.4.3.

We assume a flat cosmology with  $H_0 = 70 \text{ km s}^{-1} \text{ Mpc}^{-1}$  and  $\Omega_m = 0.3$ , in which  $1''$  is 3.34 kpc at the cluster’s redshift of 0.203. Uncertainties are quoted at 90% confidence unless otherwise stated.

## 3.2 X-ray data analysis

The *Chandra* data reduction is described in § 2.2 (W16), where we discussed all the A520 features seen in this dataset other than the shock front. In summary, we use 447 ks of *Chandra* observations of A520 performed in 2007–2008 (ObsIDs 9424, 9425, 9426, 9430). Three earlier observations (ObsIDs 528, 7703, 4125) were not used because they would not meaningfully improve our results while adding complexity to the analysis. Spectral analysis was performed using XSPEC (v12.9.0). Temperatures were obtained by

fitting an absorbed APEC model, while accounting for the additional background component as determined in [W16](#). The redshift was fixed at  $z = 0.203$ , while metal abundance (relative to [Anders & Grevesse 1989](#)) and Galactic absorption were fixed at the best-fit cluster average values of 0.21 and  $N_H = 6.3 \times 10^{20} \text{ cm}^{-2}$ , respectively, obtained from a fit to the spectrum from an  $r = 3'$  circle centered on the X-ray centroid.

### 3.3 Radio data analysis

We reanalyzed the archival VLA data at 1.4 GHz from project AF349 (the data used in [Govoni et al. 2001](#)) and projects AC776 and AC706 (the data used in [Vacca et al. 2014](#)), which observed A520 in C and D array configurations. [Table 3.1](#) gives technical details of these observations.<sup>1</sup>

We calibrated and reduced the datasets separately using the Astronomical Image Processing System (AIPS). We followed the standard procedure, with amplitude and phase calibration carried out after accurate editing of the raw data on both the primary and secondary calibration sources. The flux density scale was set using the amplitude calibrators listed in [Table 3.1](#) and the [Perley & Butler \(2013\)](#) coefficients in AIPS SETJY task. The accuracy of the flux density scale is estimated to be within 3%. Phase-only self-calibration was applied to each dataset to reduce the effects of residual phase errors. Final images were made using the multi-scale CLEAN algorithm implemented in AIPS IMAGR task, which results in better imaging of the extended sources compared to the traditional single-resolution CLEAN (e.g., [Clarke & Ensslin 2006](#)). After self-calibration,

---

<sup>1</sup>The radio data presented in [Fig. 3.2](#), and used in the subsequent analysis of the bow shock in [§ 3.4.4](#), are from a new combined reanalysis of two VLA 1.4 GHz data sets, produced by S. Giacintucci. The following is a description of the data reduction method of that reanalysis.

Table 3.1: Details of archival VLA observations of A520

Project	Configuration	Frequency (MHz)	Bandwidth (MHz)	Date	Time (min)
AF349	C	1364.9/1435.1	50/50	1998 Dec 8	129
AF349	D	1364.9/1664.9 <sup>a</sup>	50/25	1999 Mar 19	180
AC776	C	1364.9/1435.1	50/50	2005 Aug 30	250
AC706	D	1364.9/1435.1	50/50	2004 Aug 13	345

Project	FWHM, PA ("×", °)	rms ( $\mu\text{Jy b}^{-1}$ )	Primary Calibrator	$S_{\text{calibrator}}$ (Jy)
AF349	15.4 × 14.9, 59	25	3C48	16.4/15.7
AF349	50.6 × 49.4, 27	65	3C48	16.4/14.1
AC776	15.4 × 14.5, -29	22	3C147	23.1/22.2
AC706	48.8 × 46.0, 0	50	3C296	15.4/15.0

Notes. – Column (1): VLA project identifier; column (2): array configuration; columns (3) and (4): frequency and width of the two intermediate frequency (IF) channels used during the observation; columns (5) and (6): observation date and total time on source; column (7): full width at half-maximum (FWHM) and position angle (PA) of the beam; column (8): image rms noise; columns (9) and (10): primary calibrators and their flux densities set according to the [Perley & Butler \(2013\)](#) scale.

<sup>a</sup> We used only the 1364.9 MHz IF channel here.

we combined the C and D data into a single data set. For the AF349 D-configuration observation, we used only the 1364.9 MHz IF channel that matches the frequency and width of the first IFs of all other data sets. Finally, a further cycle of phase calibration was applied to the combined dataset to improve the image quality. We reached an rms sensitivity level of  $20 \mu\text{Jy beam}^{-1}$  in the final combined image, with a restoring beam of  $19''$ .

Good sampling of short baselines (i.e., close antenna pairs) in the  $uv$  plane is crucial for correct determination of the flux density, size, and structure of a low-surface-brightness source like the radio halo in A520. The inner portion of the  $uv$  plane of our final combined data set is shown in [Fig. 3.1](#). Only visibilities corresponding to baselines shorter than  $1.5 \text{ k}\lambda$  are plotted. The very good sampling of short spacings in this plot ensures high-fidelity imaging of the radio halo whose angular size of about  $5'$  (diameter) is sampled by visibilities shorter than  $0.8 \text{ k}\lambda$ . Nominally, the largest structure detectable by this dataset should be about 3 Mpc; we return to this in a more quantitative way later.

To image only the extended and compact radio sources unrelated to the giant halo, we produced images using only the baselines longer than  $0.5 \text{ k}\lambda$  and longer than  $1 \text{ k}\lambda$ , respectively. We identified 16 such sources with peak flux densities exceeding a  $3\sigma$  level of  $0.06 \text{ mJy beam}^{-1}$  (for a  $19''$  restoring beam) within  $r \sim 1 \text{ Mpc}$  from the cluster X-ray centroid. These include three extended radio galaxies (two with the narrow-angle tail morphology and one a double-lobed source), one marginally resolved object (a possible “dying” radio galaxy, as discussed by [Vacca et al. 2014](#)), and 12 unresolved sources. We then subtracted the CLEAN components associated with these compact sources (for a total flux density of 75 mJy) from the  $uv$  data and used the resulting dataset to obtain

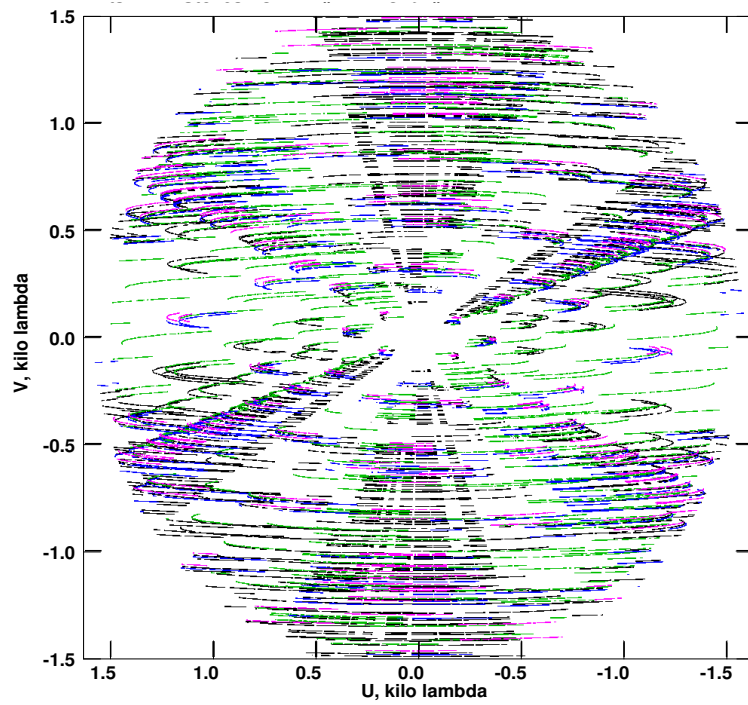


Figure 3.1: Coverage of the  $uv$  plane of spatial frequencies by the four combined *VLA* datasets (shown by different colors). Fuller coverage results in a reconstructed image with higher fidelity for the extended features. The datasets are complementary, especially at smaller wavenumbers near the center of the plot (corresponding to larger angular scales).

images of only the diffuse radio halo at multiple resolutions using the multi-scale CLEAN. Images restored with a 22'' circular beam before and after the removal of the sources unrelated to the halo are shown in Fig. 3.2. The image with sources removed (panel *a*) has an rms noise level of  $22 \mu\text{Jy beam}^{-1}$ . The halo flux density, measured within the  $1\sigma$  isocontour, is 20.2 mJy with an error of 7.2%, computed following Cassano et al. (2013), i.e., including the flux calibration uncertainty (3%), the noise in the integration area, and the error due to the subtraction of the discrete radio sources in the halo region. Our flux measurement is in agreement with the flux density of  $19.8 \pm 1.4$  used by Cassano et al. (2013) to calculate the radio halo luminosity at 1.4 GHz and measured on an image obtained from the AF349 observations. A slightly lower flux of  $16.7 \pm 0.6$  mJy is measured by Vacca et al. (2014) by masking the radio galaxies (rather than subtracting them as we did).

Our high-quality image of the radio halo reveals a prominent edge and significant brightness structure on small angular scales. We will compare these fine features with our X-ray data in § 3.4.3 and § 3.4.4. As we will see, the dataset still exhibits some interferometric artifacts with the scale and amplitude that are significant for us; we will address this in § 3.4.4.1.

## 3.4 Discussion

### 3.4.1 Bow shock

A classic bow shock would exhibit the highest Mach number  $M$  (and the highest gas density and temperature jumps) at the “nose,” and a decreasing  $M$  as the angle from the

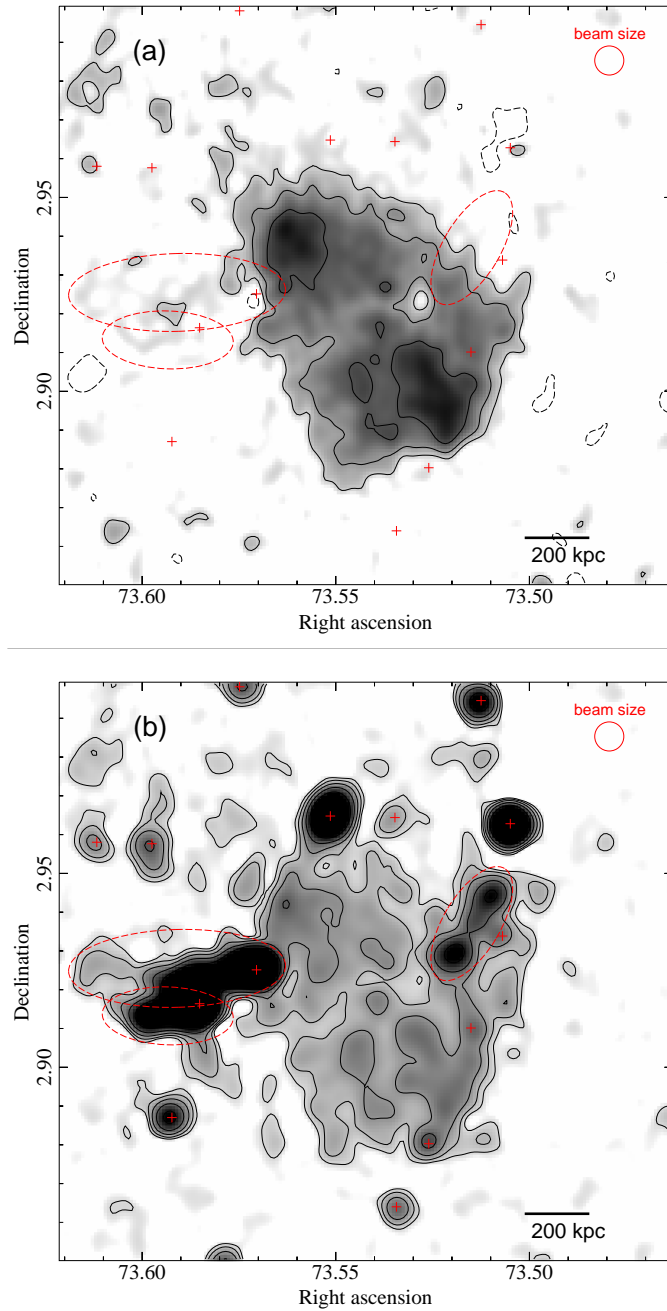


Figure 3.2: (a) 1.4 GHz image of the radio halo after the removal of unrelated sources. Red crosses mark the positions of point sources while dashed ovals mark the three extended sources associated with radio galaxies. (b) Radio brightness image before the source removal. Radio contours start at  $66 \mu\text{Jy beam}^{-1}$  ( $3\sigma$ ) in steps of  $\times 2$  (dashed contours are negative). The beam size is the same in both images. 200 kpc is  $1'$ .

axis of symmetry of the shock increases and the shock becomes oblique. For the electron–proton equilibration test that we want to perform, we need as high a Mach number as possible to maximize the difference in electron temperature between the two possibilities, and thus want to study as narrow a sector at the “nose” as possible. The deep A520 X-ray observation provides sufficient statistics to analyze the bow shock in several sectors, divided based on the brightness contrast across the front (Fig. 3.3a). We exclude a narrow segment of the front between sectors S and N1 immediately in front of the bright cool structure because of the small-scale irregularities, possibly caused by the dark matter mass peak located there (see Fig. 2.7; Figure 6 in W16), that would be difficult to model. A small region that includes those structures is also excluded from sector N1 as shown in Fig. 3.3a.

In each sector, we fit the 0.8–4.0 keV surface brightness profile with a density model that consists of two power-law radial profiles (with different slopes) on either side of the shock and an abrupt jump at the shock, whose position is a free parameter. This 3D model is projected onto the sky under the assumption that the curvature along the l.o.s. is the same as that of the brightness edge in the plane of the sky (which is further discussed in § 3.4.2.1) and compared to the brightness profiles extracted in the respective sector. For these observations, we can use the 0.8–4.0 keV count rate as a direct proxy for the l.o.s.-integrated  $n_e^2$ , because the combination of the spectral model parameters ( $N_H$ , abundance, gas temperatures) and the *Chandra* response in this energy band conspire to make the dependence of the X-ray flux on temperature negligible ( $< 1\%$  for the interesting range of temperatures, based on examining how the predicted flux responds to varying the plasma temperature of the model in XSPEC). The Mach number,  $M$ , of the shock front relative to

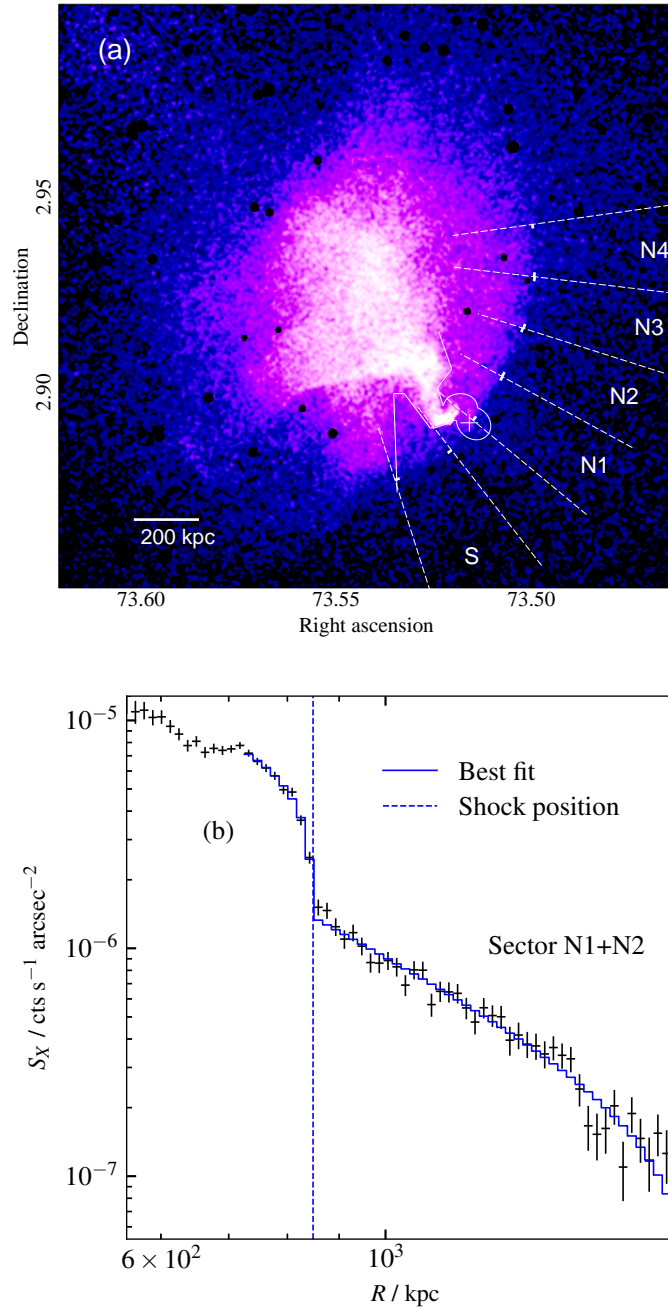


Figure 3.3: (a) 0.8–4 keV *Chandra* image, smoothed by  $2''$  gaussian (holes are masked point sources). The white dashed lines mark the sectors used for X-ray shock profile fitting, with tick marks indicating the best-fit shock position in each sector. The white cross indicates the position of the BCG next to the cold front. The white solid outline indicates masked regions for the X-ray brightness profile and spectral extraction, covering the cold front close to the shock surface. (b) X-ray brightness profile in the combined sector N1+N2 and best-fit model. 200 kpc is  $1'$ .

the upstream flow is derived from the density jump,  $x$ , using the Rankine-Hugoniot jump conditions (Landau & Lifshitz 1959):

$$M = \left( \frac{2x}{(\gamma + 1) - (\gamma - 1)x} \right)^{1/2}, \quad (3.1)$$

where we use the adiabatic index  $\gamma = 5/3$  for monatomic gas. For typical, low Mach numbers found in clusters,  $x$  is far from the asymptotic value for strong shocks (4 for  $\gamma = 5/3$ ) and thus allows an accurate determination of  $M$ . Fit results for the sectors are shown in Table 3.2. The highest Mach numbers,  $M = 2.5^{+0.5}_{-0.4}$  and  $M = 2.4^{+0.6}_{-0.3}$ , are seen in sectors N1 and N2 at the “nose” of the shock, respectively, and decrease to  $M < 2$  on either side, where the shock becomes oblique. The shock “nose” direction is in agreement with the NE–SW merger axis. The “nose” sectors have higher values compared to  $M = 2.1^{+0.4}_{-0.3}$  reported in M05 because the latter included the adjacent sectors with lower density jumps.

Although the  $M$  decline toward the wings of the front is expected, it has only been reported previously for the main shock of the Bullet cluster (Markevitch & Vikhlinin 2007, hereafter MV07), because such a study requires good statistics. Care should therefore be taken when using a wide sector to analyze bow shocks, as the peak density jump will probably be underestimated.

### 3.4.2 Electron–ion equilibration timescale

In the collisional plasma picture, a shock front with relatively low Mach numbers — such as those occurring in cluster mergers — would heat protons and heavier ions

Table 3.2: Details of X-ray modeling of shock sectors

Sector	$\rho$ Jump	$M$	Inner slope	Outer slope	$\chi^2/\nu$
S	$2.0^{+0.2}_{-0.3}$	$1.7^{+0.2}_{-0.2}$	$-0.8^{+0.4}_{-0.6}$	$-1.8^{+0.3}_{-0.2}$	59.5/43
N1	$2.7^{+0.3}_{-0.3}$	$2.5^{+0.5}_{-0.4}$	$-0.3^{+0.7}_{-0.7}$	$-1.7^{+0.3}_{-0.2}$	35.6/27
N2	$2.6^{+0.4}_{-0.2}$	$2.4^{+0.6}_{-0.3}$	$-0.2^{+0.7}_{-0.6}$	$-1.7^{+0.2}_{-0.3}$	34.3/27
N3	$2.2^{+0.3}_{-0.2}$	$1.9^{+0.3}_{-0.2}$	$-1.1^{+0.6}_{-0.8}$	$-1.7^{+0.2}_{-0.2}$	44.2/27
N4	$1.9^{+0.2}_{-0.2}$	$1.6^{+0.2}_{-0.1}$	$-0.4^{+0.3}_{-0.3}$	$-1.5^{+0.1}_{-0.2}$	68.5/39
N1+N2	$2.7^{+0.2}_{-0.3}$	$2.4^{+0.4}_{-0.2}$	$-0.5^{+0.8}_{-0.7}$	$-1.6^{+0.1}_{-0.2}$	24.7/30

Notes. – Column (1): shock sector as shown in Fig. 3.3a; column (2): density jump at shock; column (3): shock Mach number; column (4): density profile inner power law index; column (5): density profile outer power law index; column (6): chi-square and degree of freedom. Errors are 90% with all other parameters free.

dissipatively, while electrons, whose thermal velocity is much higher than the velocity of such shocks, are compressed adiabatically to a temperature lower than that of ions. Protons and electrons subsequently equilibrate on a Coulomb collision timescale (e.g., [Spitzer 1962](#); [Zeldovich & Raizer 1966](#)):

$$\tau_{\text{ep}} = 2 \times 10^8 \text{ yr} \left( \frac{n_e}{10^{-3} \text{ cm}^{-3}} \right)^{-1} \left( \frac{T_e}{10^8 \text{ K}} \right)^{3/2}. \quad (3.2)$$

We can measure the electron temperature directly by modeling the X-ray spectrum, but cannot measure the proton temperature<sup>2</sup>. However, the *equilibrium* post-shock temperature  $\overline{T}_2$  (the one that protons and electrons achieve asymptotically) can be derived from the pre-shock temperature and the compression factor  $x$  (or, equivalently, the Mach number) using the shock jump conditions:

$$\frac{\overline{T}_2}{T_1} = \frac{(\gamma + 1)x - \gamma + 1}{x(\gamma + 1) - x^2(\gamma - 1)}. \quad (3.3)$$

Indices 1 and 2 correspond to pre-shock and post-shock quantities, respectively. The adiabatic temperature jump for the electrons comes from  $T \propto \rho^{\gamma-1}$  for an adiabatic compression, so

$$T_{\text{e,ad}} = T_1 x^{\gamma-1}. \quad (3.4)$$

The time dependence of the electron temperature  $T_e$  increasing asymptotically from the adiabatic value to the equilibrium value under Coulomb collisions was given by, e.g., [Fox & Loeb \(1997\)](#), [Wong & Sarazin \(2009\)](#), and [Sarazin et al. \(2016\)](#). As the local  $T_e$

---

<sup>2</sup>It is possible to infer the temperature of heavier ions (assuming they are in thermal equilibrium) by measuring the thermal broadening of their emission lines. However, such high spectral resolution measurements remain observationally challenging (e.g., [Hitomi Collaboration et al. 2018](#)) and combined with the spatial resolution required for this test, will be out of reach for the foreseeable future.

increases, the post-shock gas flows away from the shock front, and the  $T_e$  time dependence gets encoded in the spatial temperature profile, which can be measured by *Chandra*. The closing piece of the experimental setup is the velocity of the post-shock gas relative to the front, which is given by the shock mass conservation condition:

$$v_2 = M c_{s1}/x, \quad (3.5)$$

where  $c_{s1}$  is the pre-shock sound speed, determined from the X-ray measured pre-shock temperature (electrons and ions in the pre-shock region can reasonably be assumed to be in equilibrium).

The Mach number should be sufficiently high to distinguish between shock heating and adiabatic compression. For  $M = 2.4$ , there is a measurable difference between the two, but they become practically indistinguishable for  $M \lesssim 2$ . In sectors N1 and N2, the shock is strongest, and their Mach numbers are statistically the same (Table 3.2), thus we will combine them (see the N1+N2 entry) and use the combined profile for the above test. We will use the other sectors, which should be insensitive to the possible temperature non-equilibrium, for consistency checks.

We construct two model  $T_e$  profiles for each sector, one for adiabatic compression at the shock and subsequent Coulomb equilibration, and the other for instant equilibration, and compare them with the observed temperature profile. The electron density is derived from the emission measure using the normalization of the APEC model in XSPEC,  $\int n_e n_H dV = 10^{14} \times \text{norm} \times 4\pi [D_A(1+z)]^2$ . In sector N1+N2, we find  $n_{e1} = (4.04 \pm 0.15) \times 10^{-4} \text{ cm}^{-3}$  immediately in front of the shock, and  $n_{e2} = (1.07 \pm 0.11) \times 10^{-3} \text{ cm}^{-3}$

behind the shock (the latter includes a 10% uncertainty of the density jump). Reasonable deviation of the shock surface from spherical does not affect our results – this is discussed in § 3.4.2.1.

The pre-shock temperature profile for N1+N2 is consistent with being constant out to at least 800 kpc from the shock (Fig. 3.4). We thus decided to use the best-fit temperature in a radial bin between 10 and 400 kpc from the shock (where we excluded the immediate vicinity of the shock to avoid any irregularities of the front),  $T = 4.70_{-0.72}^{+0.82}$  keV, as the pre-shock value. This temperature, the best-fit compression factor, and Eq. 3.5 give the post-shock gas velocity of  $1030_{-80}^{+90}$  km s<sup>-1</sup> relative to the shock front. During the collision equilibration timescale  $\tau_{\text{ep}} \simeq 0.2$  Gyr, the post-shock gas travels  $\sim 200$  kpc or 65'', which is well resolved by *Chandra*.

We will compare the deprojected and projected temperature profiles for N1+N2 with the instant-equilibration and adiabatic compression models in Fig. 3.4 and Fig. 3.5a. To construct the adiabatic compression model, we calculate the time dependence of the local post-shock  $T_e$  using the measured shock parameters following Sarazin et al. (2016). For the instant-equilibration model, we assume the electron temperature jumping to  $\overline{T}_2$  right at the shock. These models with their uncertainties, which include statistical uncertainties of the pre-shock temperature and the density jump, are shown in Fig. 3.4. The 3D temperature model profile is projected onto the sky using the best-fit density model and the spectroscopic-like temperature weighting  $w = n^2 T^{-3/4}$ , following Mazzotta et al. (2004). The projected model profiles are shown in Fig. 3.5 for sector N1+N2 as well as N3 and N4.

We also deproject the *measured* temperatures in bins of several sizes (30, 50, and

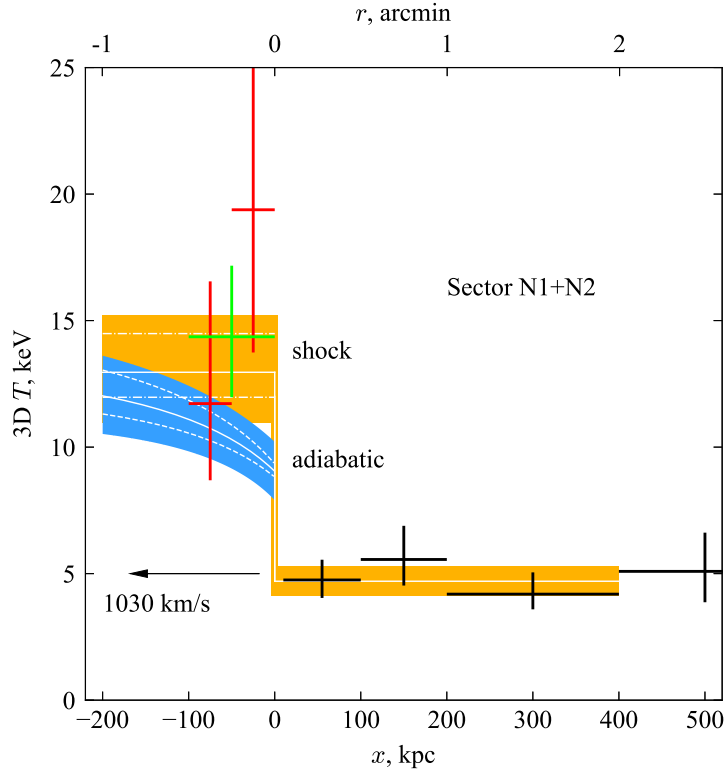


Figure 3.4: Deprojected post-shock temperatures compared with model profiles in sectors N1 and N2 combined (Fig. 3.3a). The yellow band is the instant-equilibration model, while the blue band is adiabatic compression followed by Coulomb equilibration. The band width indicates  $1\text{-}\sigma$  error bounds. In the pre-shock region, this equals the error in the pre-shock temperature measurement, while in the post-shock region this further includes the density jump parameter uncertainty, which has a smaller effect. The white dashed and dotted–dashed lines bounding the post-shock model profiles indicate the effect of geometric uncertainty ( $\pm 10\%$  change in the l.o.s. extent). The  $x$ -axis denotes distance from the shock position. Different colors of post-shock crosses correspond to bins of different widths (red is 50 kpc and green is 100 kpc).  $x$ -error bars denote the radii in which temperature was measured.  $y$ -errors are  $1\sigma$ .

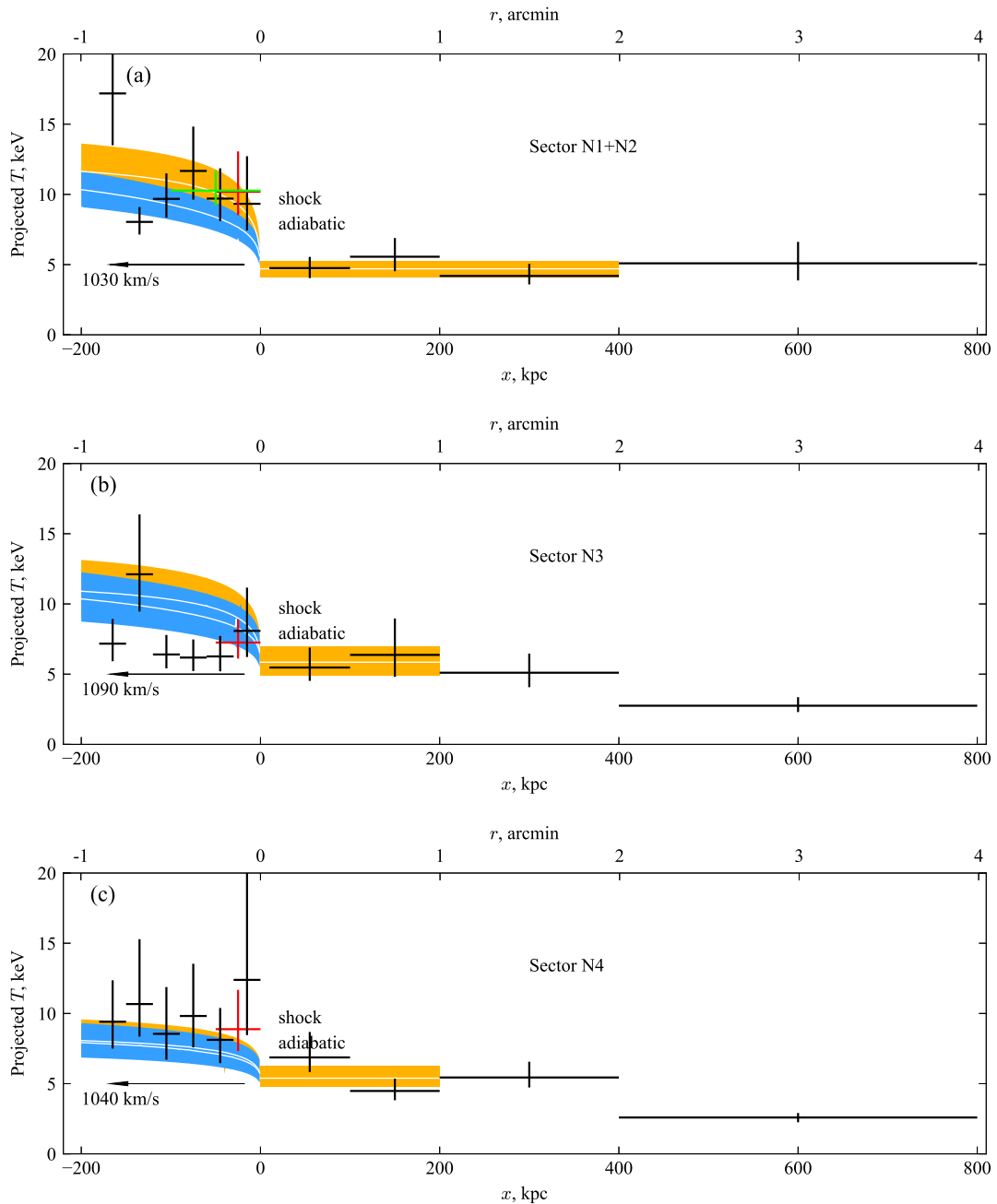


Figure 3.5: Projected temperatures compared with model profiles for segments of the shock surface in sectors labeled in Fig. 3.3a. The model profiles are projected spectroscopic-like temperature, using  $n^2 T^{-3/4}$  weighting, following Mazzotta et al. 2004). The  $x$ -axis denotes distance from the shock position. Different colors of post-shock crosses correspond to bins of different widths.  $x$ -error bars denote the radii in which temperature was measured.  $y$ -errors are  $1\sigma$ . The bands are  $1\sigma$  error bounds.

100 kpc) immediately after the shock by estimating the contributions of the outer 3D shells into the spectrum from the respective post-shock region and adding the properly normalized spectral component in the XSPEC fit to represent the projected gas. Using projected profile and using deprojected profile are equivalent — the difference between the two models is greater for the 3D profiles, but so is the uncertainty of the deprojected measured temperature.

For the N1+N2 sector, in the 50 kpc bin behind the shock, we measure the projected temperature of  $T = 10.2_{-2.4}^{+5.3}$  keV, while the deprojected temperature using the best-fit 3D density model is  $T = 19.4_{-8.4}$  keV (unconstrained on the high side because of *Chandra's* poor sensitivity to such high temperatures). The first post-shock bin is the most useful, because it has the greatest model difference. For illustration purposes, we also obtained a deprojected temperature for the second 50 kpc shell, with the first 50 kpc post-shock shell fixed at the model instant-equilibration temperature, in effect deprojecting the instant-equilibration model (this is done to regularize the deprojection procedure, as the errors of the neighboring bins are anti-correlated). The procedure was repeated for three narrower 30 kpc post-shock bins, and for one wider 100 kpc bin.

The deprojected  $T_e$  in the first 30, 50, and 100 kpc post-shock bins are all above the adiabatic model and consistent with the instant-equilibration model. (Of course, these measurements are not statistically independent.) The adiabatic model is below the measured deprojected value at 95% significance in a single parameter test for the 50 kpc and 100 kpc bins, and around 90% for the 30 kpc bin. Similarly, the projected spectroscopic-like temperatures are higher than the adiabatic compression model at 95% significance for the 50 kpc and 100 kpc bins.

In the 30 and 50 kpc bins further from the shock, the temperatures remain consistent with the instant-equilibration model. In Fig. 3.5a, we show the 30 kpc bins for the projected profile up to about 200 kpc behind the shock to give a broader overview; however, cool core fragments and unrelated cluster structure can be seen within 200 kpc behind the shock (Fig. 3.3a), which can affect the projected temperatures and create the apparent large scatter.

For a consistency check, we also obtained the projected temperature profiles in sectors N3 ( $M = 1.9_{-0.2}^{+0.3}$ ) and N4 ( $M = 1.6_{-0.1}^{+0.2}$ ), where the Mach numbers are insufficiently high to distinguish the two models (Fig. 3.5b,c). In these sectors, the pre-shock temperature shows a slow decrease with radius, so we derived the best-fit pre-shock temperatures in a narrower 10–200 kpc bin. They are consistent with the pre-shock temperature for N1+N2. In both sectors, the temperature increase immediately behind the shock is consistent with both models. In N3, the presence of a cool blob of gas causes measurements from about 50 kpc behind the shock to be lower than adjacent sectors; this blob has been seen in the temperature map (Fig. 2.3; Figure 2 in W16). In N4, measurements appear systematically above the models (although not significantly). This may be caused by our underestimating of the immediate pre-shock temperature, as the deviation at the first pre-shock bin suggests. We conclude that sectors N3 and N4 behave consistently with the expectation for the lower Mach numbers observed in these sectors.

#### 3.4.2.1 Geometrical systematic uncertainty

In the above experiment, we relied on the assumption that the shock surface has the same curvature along the l.o.s. as in the plane of the sky. This is a reasonable assumption

for this merger with a relatively clear geometry, for which the apparent shock direction is generally well aligned with the merger axis evident from both the X-ray and lensing maps, and the shock front center of curvature in the image approximately coincides with the large-scale cluster centroid. Nevertheless, we should determine how the uncertainty of this assumption affects the results. If the surface has a different curvature along the l.o.s., we would derive the incorrect density jump and Mach number. The deprojected post-shock temperature would also be affected, but because of the relatively high brightness contrast at the shock (i.e., a relatively low projected contribution), this is a secondary effect.

To evaluate the effect, we varied the radius of curvature of the shock surface along the l.o.s., while keeping the pre-shock gas model unchanged (spherically symmetric). For simplicity we used a spheroid geometry for the shock surface, keeping its axes in the plane of the sky to be the same as the shock radius  $r_{\text{jump}}$ , while linearly stretching its l.o.s. axis. Note that with this geometry, the extent  $l$  of the shock surface in the l.o.s. direction scales with the l.o.s. radius of curvature  $R$  not linearly but as  $l \propto \sqrt{R}$ .

For a 20% change in  $R$ , the best-fit density jump changed by 5% — the difference coming from the change in post-shock density, while the pre-shock density stays the same. This is smaller in magnitude than the  $\sim 10\%$  fitting error on this parameter, so for a moderate amount of shock-surface variation, the geometry does not significantly affect our results (see [Fig. 3.4](#)). For this uncertainty to become dominant, the shock surface should be very asymmetric, e.g. a factor 1.7 different  $R$  corresponds to a 15% change to the density jump.

### 3.4.2.2 Comparison with other shocks

While such a degree of asymmetry seems unlikely for the relatively symmetric merger in A520, there is no way of knowing this for sure for each individual shock. One way to assess the probability of the shock front asymmetries and how well the true Mach number is recovered from the X-ray density profiles is to study shocks in cosmological simulations. On the observational side, measurements for a sample of relatively strong ( $M \gtrsim 2.5$ ) shocks is needed for a robust conclusion on the electron–proton equilibration timescale. Our A520 result adds a data point to two other previously published measurements — the Bullet cluster with  $M \approx 3$  (Markevitch 2006 hereafter M06, MV07) and the stronger of the two shocks in A2146, one with  $M = 2.3$  (R12). The Bullet cluster showed, at a similar 95% confidence, a similar preference for fast electron–proton equilibration. The A2146 shock showed preference for the Coulomb equilibration at a similar  $\sim 2\sigma$  significance (considering, as we do, only the temperature bin immediately after the shock) — although the instant-equilibration and Coulomb models themselves were only  $1\sigma$  apart due to a low  $M$  and a large uncertainty for the pre-shock temperature. The physics of the intracluster plasma in different clusters should be similar, so we should get the same answer from all of the experiments. The mild contradiction between the Bullet and A520 on one side and A2146 on the other may be a reflection of the above geometrical uncertainty. We do note that the bow shock in A2146 used in R12 exhibits a flat shape at its “nose,” with the shock center of curvature far from the cluster centroid (see Figure 8 in R12), which diminishes our confidence in the above l.o.s./image plane symmetry assumption. It is interesting that their second, weaker shock exhibits a  $T_e$  jump that is *higher* than the

prediction of both models (at a similar significance), which may be further illustration of the geometric uncertainty. An additional apparent difference between our (along with M06 and Sarazin et al. 2016) and R12 analyses is the three times longer Coulomb equilibration timescale used in R12 (cf. their Equation 2 and our Eq. 3.2), although this would not reconcile the results.

Sarazin et al. (2016) performed a similar test on an  $M = 2.5$  shock front at the position of the western radio relic in A3667. Their derived post-shock electron temperature goes below even the adiabatic model, which would appear to indicate a problem with this method. However, that shock is located 2 Mpc away from the cluster center, where the cluster emission is very faint and a projection of any unrelated X-ray structure on the l.o.s. may have a significant effect. For example, if a faint, cool group were projected onto the post-shock region, it would result in both an overestimate of the gas density jump and an underestimate of the temperature jump — effect of the right sign to explain their result. For A520, as well as the Bullet and A2146, projection of unrelated objects is much less of a problem because the shocks are located in much brighter cluster regions.

Thus, our conclusion is score 2:1 in favor of quick electron–proton equilibration in the intracluster plasma, but more strong shocks need to be studied to reduce the systematic uncertainties.

### 3.4.3 Radio halo features

There are interesting coincidences between the radio halo and X-ray features in A520 (Fig. 3.6a). There are bright radio spots at the positions of the cool “foot” and “knee” that we discussed in § 2.4.2. The radio emission here may be related to a radio

*minihalo* that had inhabited the cool core before its disruption, which gave rise to these cool X-ray clumps, as minihalos are observed in almost all massive cool cores (Giacintucci et al. 2017). The radio enhancements there may also be caused by reacceleration of relativistic particles by local turbulence in the wake of the disrupted cool core (see Brunetti & Jones 2014 for review of possible acceleration mechanisms in clusters). Another prominent, broad brightness peak in the NE half of the radio halo is located at one of the hottest regions of the cluster, but it does not have any obvious corresponding X-ray brightness structures. This can be the site of vigorous merger-induced turbulence, which would produce relativistic electrons via reacceleration. Future spatially resolved X-ray calorimeters with much higher spectral resolution than *Chandra*, such as *XRISM*, will be able to study the l.o.s. velocities of the gas in this turbulent region.

#### 3.4.4 Origin of the radio edge

As discussed in M05, the X-ray bow shock in A520 traces a sharp edge of the radio halo, and we see it clearly in Fig. 3.6. Mechanisms of producing ultra-relativistic electrons responsible for the post-shock radio synchrotron emission include first-order Fermi acceleration, which can use thermal electrons as its seeds or re-accelerate “fossil” relativistic electrons (e.g., Blandford & Eichler 1987) that existed prior to shock passage but whose radio brightness is below the detection limit. Another possible mechanism is adiabatic compression of such fossil electrons and the compression of the magnetic field (since cosmic rays and magnetic fields are frozen into the thermal gas that is being compressed by the shock). Both the adiabatic compression and the reacceleration should be present, but the reacceleration boost for aged, steep-spectrum electrons depends on the the

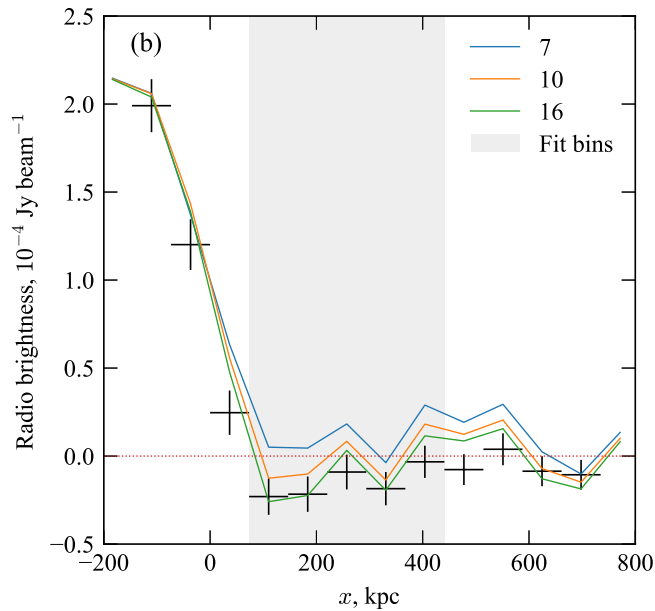
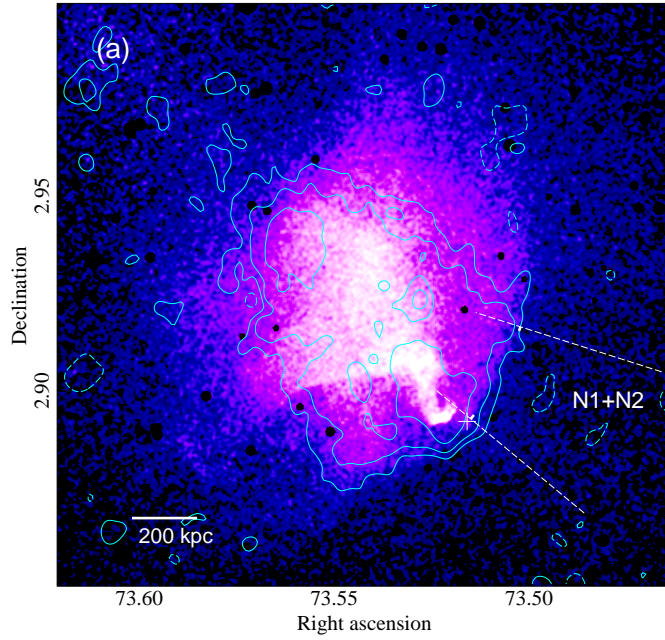


Figure 3.6: (a) 0.8–4 keV *Chandra* image, same as Fig. 3.3a, showing the combined sector N1+N2. Radio contours are the same as in Fig. 3.2a. (b) Radio brightness profile in the combined sector N1+N2 (crosses: extracted radial profile; solid lines: profiles extracted from simulated images with additional pre-shock emission injected, for different values of the emissivity jump; grey band: the 5 bins used to measure  $\Delta\chi^2$ , see § 3.4.4.1). The radial bins correspond to the FWHM beam size.  $x$  is relative to the X-ray best-fit shock position.

Lorentz factor  $\gamma_{\max}$  of the fossil electrons (see M05 for discussion of the resulting spectrum and normalization), so either effect may dominate. In either of these two scenarios, the fossil relativistic electrons in the pre-shock region should produce radio emission at a certain low brightness level that can be related to that of the post-shock emission. As derived in M05 in the compression-only scenario, for a power-law fossil electron energy spectrum with index  $\delta$  (defined as  $dN/d\gamma \propto \gamma^{-\delta}$ ), a gas density jump by factor  $x$  at the shock, and certain assumptions about the tangled magnetic field, the radio emissivity per unit volume would change as

$$I_{\nu} \propto x^{\frac{2}{3}\delta+1}. \quad (3.6)$$

If both compression and significant reacceleration are present, for a fixed *observed* post-shock radio brightness, we would expect a lower level of pre-shock radio emission, and in the case of the Fermi acceleration directly from the thermal pool, the pre-shock radio emission would be lower still by many orders of magnitude. With our new, higher-sensitivity radio map, we can try to test these possibilities by extracting a radio surface brightness profile across the shock.

#### 3.4.4.1 Modeling radio emissivity profile

In the same sector N1+N2 where we obtained the highest Mach number bins, we extracted a radio profile binned to the beam size and aligned with the best-fit shock position. It is shown in Fig. 3.6b; the radio brightness drops sharply at the position of the X-ray shock and is not detected in the pre-shock region. To evaluate measurement errors for the profile, we generated Gaussian noise images with the observed rms noise of

$22 \mu\text{Jy beam}^{-1}$  after smoothing by the beam size, and extracted radial profiles from 1000 smoothed noise images. An elongated “hole” in the radio image in the N1+N2 sector about 200 kpc in front of the shock (dashed radio contour in Fig. 3.6a) is most likely an interferometric artifact. Since we want to place an *upper* limit on the pre-shock radio emission, to be conservative we masked this negative deviation.

We will now compare this radio brightness profile and, in particular, the non-detection in the pre-shock region, with the expectation for an adiabatic compression model for the origin of the radio edge. To model the radio image, we created a spherical model of the radio emissivity in the relevant region of space, projected it on the sky, and convolved it with the *VLA* beam.

For lack of information on the distribution of cosmic rays and magnetic fields in A520, our model makes two assumptions. First, the density of cosmic-ray electrons is assumed proportional to that of thermal ICM. If we consider the various possible sources for fossil electrons — merger shock acceleration and subsequent vigorous mixing, disrupted and mixed radio galaxies, turbulent acceleration, and “secondary” electrons from cosmic-ray proton collisions (see Brunetti & Jones 2014 for a review) — this seems a reasonable assumption. We note that for our purpose, this is a conservative assumption compared to the alternative of a flat cosmic-ray density profile. Second, we assume the magnetic field strength changes across the cluster as  $B \propto n^{0.5}$  (where  $n$  is gas density), which is the best fit derived for Coma (Bonafede et al. 2010), also a merging cluster. Then the synchrotron emissivity (emission per unit volume)  $P \propto nB^2 \propto n^2$ , so the pre-shock radio emissivity has essentially the same dependence on the gas density as the X-ray. We therefore use the radial profile derived from the X-ray and only let the normalization change to model the

radio profile.

The post-shock region is fit very well with the projection of a 3D model with an abrupt emissivity drop, convolved with the beam. We assume constant emissivity vs. radius in this region, because we are most interested in the bin immediately next to the shock surface and because it is not clear how the radio brightness should change further downstream (the image does not have enough leverage to fit this slope because of the unrelated radio structures inside the cluster halo). We did check that the post-shock radio profile does not favor, for example, a thin 3D shell that in projection would show a peak at the shock position and a decline toward smaller radii. The jump in radio emissivity at the X-ray shock location is the only free parameter. The model is truncated at 1.5 Mpc from the X-ray centroid (which is 1.15 Mpc from the shock surface); because of the model's steep decline, this does not matter much.

Because an interferometer can lose signal on large angular scales, we must be careful when deriving an upper limit in the low-surface-brightness areas. The unknown zero level of the image limits our ability to constrain the pre-shock emission, but we should be able to constrain models with steep changes on linear scales that are well within the nominal  $uv$  coverage limit, which is  $\sim 3$  Mpc for this dataset (§ 3.3). However, there may be subtle artifacts on all scales, and for example, the apparent systematic negative values in the radio profile in the pre-shock region are a cause for concern. With this in mind, rather than simply fitting the projected radio emission model to the profile, we tried to account for the possible artifacts to a first approximation by convolving the brightness model with the actual  $uv$  coverage and the beam and reconstructing the image. Technically, we followed [Giacintucci et al. \(2014\)](#) and “injected” or added our brightness model for the

pre-shock emission into the pre-shock region of the data using the AIPS task UVSUB. We then extracted a radial profile in the same sector of the new image, thought of it as a model, and compared it with the actual profile using the  $\chi^2$  statistics. (Because the same statistical noise is present in both the real and the “model” images, for the  $\chi^2$  calculation we used the errors for only one of the profiles). The injected brightness model was calculated by keeping the post-shock emission at the same best-fit level, while varying the jump amplitude and thus the normalization of the pre-shock profile (only the pre-shock region of the model emission was injected). We compared the data and model profiles in the 400 kpc pre-shock radial interval [Fig. 3.6b](#) to avoid being affected by the accuracy of our model assumptions while being interested only in the shock jump.

This exercise revealed that the negative deviations in the pre-shock region are indeed an artifact — the difference between the image with and without the injection there was *less* than the injected emission, which means that the interferometer does redistribute the flux from this region into other radial bins (see, e.g., the positive bump around  $x \approx 500$  kpc). Theoretically, it should be possible to account for this effect and constrain the absolute brightness in the pre-shock region, but it would require creating an accurate spatial model of the radio brightness for the entire cluster, which is beyond the scope of this study. (It may be more efficient instead to obtain a dataset with better  $uv$  coverage that would not require such modeling.)

Nevertheless, we can evaluate the sensitivity of this radio image to the pre-shock emission under the assumption that the true pre-shock emission in the data is zero. Then, an injected model that corresponds to the emissivity jump by a factor of 10 (see [Fig. 3.6b](#)) is rejected at a  $3\sigma$  statistical significance, while a jump by a factor of 16 is rejected at  $2\sigma$ .

If we ignored the interferometric artifact and simply convolved the brightness model with the beam without accounting for the  $uv$  coverage, we would exclude a factor 22 jump at a  $3\sigma$  level.

#### 3.4.4.2 Comparison with adiabatic compression

Let us now compare this with the emissivity jump expected in the adiabatic compression model. Compression does not alter particle energies, but increases synchrotron emissivity through higher electron density and magnetic field strength. It would preserve the shape of the electron energy spectrum, while shifting the radio spectrum in frequency and changing its normalization. For a power-law electron spectrum, the radio synchrotron spectrum  $I_\nu \propto \nu^{-\alpha}$  is related to the electron spectrum via  $\alpha = (\delta - 1)/2$ . For the radio spectral index, we use  $\alpha = 1.25 \pm 0.11$  ( $1\sigma$  errors) from the first post-shock bin in Figure 6 of [Vacca et al. \(2014\)](#), which corresponds to  $\delta = 3.5 \pm 0.2$ . Formally, for the observed gas density jump of  $x = 2.7$  in sector N1+N2 ([Table 3.2](#)), [Eq. 3.6](#) gives the expected radio emissivity jump of  $27 \pm 4$  for the adiabatic compression scenario. For comparison with the data, we need to include projection effects, because the post-shock radial brightness profile includes regions along the l.o.s. that are away from the shock “nose,” with a lower density jump. The gas density jump azimuthal dependence in the plane of the sky in the sectors in which it was measured, can be interpolated well by  $x = x_{\text{nose}}(\cos \theta)^{1/2}$ , where  $\theta$  is the angle from the “nose” of the shock. Then, we assumed rotational symmetry about the “nose” and calculated the shock-surface-area-weighted radio jump (given by [Eq. 3.6](#)) in the first post-shock bin in the radio brightness profile. This gives a value of 16 for the average radio emissivity jump, which can be directly compared with the limits derived

above for a model that did not include this azimuthal dependence for simplicity.

If we approximately include radiative cooling of the post-shock relativistic electrons, we expect a lower emissivity jump at the shock and therefore more easily detectable pre-shock emission. The radio spectrum should steepen within  $\sim 100$  kpc downstream of the shock (M05). The beam size of the *VLA* data used to calculate spectral index images by Vacca et al. is 130 kpc (see their Figure 4), so such a spectral change in the immediate post-shock region is not resolved, and the spectral index immediately at the shock would be flatter. An unresolved mixture should have a volume-averaged slope of  $\bar{\alpha} \approx \alpha + 1/2$  (Ginzburg & Syrovatskii 1964), so for  $\bar{\alpha} \simeq 1.25$  the value at the shock could be  $\alpha \simeq 0.75$ , for which the radio emissivity jump in the compression scenario would be a factor of 9 (including the projection of oblique shock contributions), compared to 16 obtained above without cooling. The true value may be somewhere in this interval, depending on the processes in the post-shock plasma. Note that in the above calculations, we do not consider radiative cooling of the pre-shock electrons, in effect assuming either that something balances that cooling or that the pre-shock electrons are continuously generated by some process (e.g., cosmic-ray proton collisions with thermal protons). If cooling is balanced pre-shock, it may be balanced post-shock as well, so the above cooling correction for the spectral index would not be necessary. A high-resolution map of the post-shock spectral index may shed light on the relevant physical processes here.

Comparing these estimates to the limits above, we see that the statistical sensitivity of the radio data would allow us to exclude such jumps at  $>3\sigma$  confidence. However, because of the unfortunate interferometric artifact, the exclusion significance is lower, only  $\sim 2\sigma$ , and it depends on the assumption about the zero level in the image. Nevertheless,

this demonstrates that ruling out the compression model is within reach with a dataset with similar sensitivity but better  $uv$  coverage.

Note that our estimates above used the assumption that the electrons have a power-law energy spectrum. If this is not the case (e.g., both pre-shock and post-shock spectra may have a cutoff at some frequencies because of radiative cooling), the adiabatic model can still be constrained, but it requires measurements at several frequencies. As noted in M05, using our notation, a single electron emits most of its synchrotron radiation at a frequency that scales with the compression factor as

$$\nu_{\text{peak}} \propto B\gamma^2 \propto x^{4/3}. \quad (3.7)$$

For  $x = 2.7$ , the post-shock electron emitting at 1.4 GHz would have emitted at 370 MHz before the shock passage (or at 560 MHz for  $x = 2.0$ ). So pre-shock observations at those lower frequencies, combined with the post-shock 1.4 GHz brightness, would be least dependent on the assumed shape of the electron spectrum. Alternatively, pre-shock measurements at 1.4 GHz would need to be combined with higher-frequency data for the post-shock region. And, ultimately, measuring the spectrum of the post-shock emission in the relevant range above and below 1.4 GHz and verifying that it is a power law (or detecting a curvature) would provide the most robust constraint.

### 3.5 Summary

We analyzed a deep *Chandra* exposure of A520 to study its prominent bow shock, one of only a handful of merger shocks with simple and unambiguous geometry and a

relatively high Mach number. At the “nose” of the shock, we find  $M = 2.4^{+0.4}_{-0.3}$ . This is higher than in the previous study based on a shorter exposure (M05), because we were able to use a narrower sector at the “nose” of the shock. As expected, the Mach number declines (toward 1.6–1.7) away from the “nose,” where the shock front becomes oblique.

The relatively high Mach number of the central segment of the front allowed us to perform a test of the electron–proton equilibration timescale, similar to the earlier tests for the Bullet cluster (M06, MV07) and A2146 (R12). We fit the shock X-ray brightness profile using a gas density model with a jump, and, using the density jump to evaluate the post-shock gasdynamic temperature, compared it to the measured post-shock electron temperature. The electron temperature immediately behind the shock is higher than expected from a simple picture where electrons are compressed adiabatically by the shock and then equilibrate with protons on a Coulomb collisional timescale. This indicates a faster equilibration rate, pointing to the prevalence of other particle interactions in hot magnetized plasma. Although the confidence level is only 95% (this includes the statistical error on temperature, ACIS background uncertainty, and sky background effect), it is similar to the finding for the Bullet cluster (M06, MV07). Although the A2146 result (R12) was inconclusive (mostly because its Mach number is lower and the amplitude of the effect is smaller), it did prefer adiabatic compression over fast equilibration. The scatter between these results most likely reflects the geometric uncertainty inherent in this test — the curvature of the shock front in the sky plane is used to model its curvature along the l.o.s. This scatter can be averaged out by studying a sample of shocks, and our result provides a third entry for such a sample. Unfortunately, bow shocks that are as clear-cut as Bullet or A520 are rare, so expanding the sample may require going to higher

redshifts with more sensitive instruments. This is worth the effort, because cluster shocks provide one of the most direct methods of determining this important timescale for any astrophysical plasmas.

We also present a new combined analysis of the archival 1.4 GHz radio *VLA* data on the cluster giant radio halo, previously analyzed separately in [Govoni et al. \(2001\)](#) and [Vacca et al. \(2014\)](#). In addition to providing lower statistical noise, the datasets complement each other's interferometric coverage, which improves fidelity of the reconstructed image. The radio image reveals several interesting features, such as the bright spot that coincides with the disrupted cool core, possibly related to a former minihalo. Another bright spot may point to a region of high turbulence, a possible target for future X-ray calorimetric measurements.

A520 is one of the growing number of clusters where both a giant radio halo and an X-ray shock front are observed ([Markevitch 2012](#)). As in most of them, there is a prominent sharp edge of the radio halo that coincides with the X-ray shock front. Some clusters have X-ray shocks with counterparts both in the form of the halo edges and radio relics ([Shimwell et al. 2015](#)). Studying these colocated features may shed light on the physical processes responsible for the generation and acceleration of the radio-emitting electrons. For example, in our A520 dataset, the radio emission in the pre-shock region is undetected at a very low brightness level, which has not been probed for any other shocks. If the jump of the radio emission at the shock were caused by simple adiabatic compression of relativistic electrons in the pre-shock plasma (e.g., remaining from past shocks or produced throughout the cluster by cosmic-ray proton interactions), we should see the radio emission beyond the edge ([M05](#)). We came close to being able to rule this

model out (and thus demonstrate the existence of particle acceleration or reacceleration at shocks) based on statistical sensitivity of the radio data. However, an interferometric artifact in the region of interest dominates the uncertainty. Our analysis shows that this interesting test for the cluster radio halos is within reach, but probably requires an observation with a better interferometric coverage and at lower frequencies, e.g., with *GMRT* or *LOFAR*.

## CHAPTER 4

---

A deep X-ray look at Abell 2142 —  
Viscosity constraints from Kelvin-Helmholtz eddies,  
A displaced cool peak that makes a warm core, and  
A possible plasma depletion layer

*This chapter has been adapted from the version to appear in The Astrophysical Journal (Wang & Markevitch 2018).*

We analyzed 200 ks of *Chandra* ACIS observations of the merging galaxy cluster A2142 to examine its prominent cold fronts in detail. We find that the southern cold front exhibits well-developed Kelvin-Helmholtz (KH) eddies seen in the sky plane. Comparing their wavelength and amplitude with those in hydrodynamic simulations of cold fronts in viscous gas, and estimating the gas tangential velocity from centripetal acceleration, we constrain the effective viscosity to be at most 1/5 of Spitzer isotropic viscosity, but consistent with full Braginskii anisotropic viscosity for magnetized plasma. While the northwestern front does not show obvious eddies, its shape and the structure of its brightness profile suggest KH eddies seen in projection. The southern cold front continues in a spiral to the center of the cluster, ending with another cold front only 12 kpc from the gas

density peak. The cool peak itself is displaced  $\sim 30$  kpc from the brightest cluster galaxy (BCG), the biggest such offset among centrally-peaked clusters, while the X-ray emission on a larger scale is still centered on the BCG, indicating that the BCG is at the center of the gravitational potential and the cool gas is sloshing in it. The specific entropy index of the gas in the peak ( $K \approx 49$  keV cm<sup>2</sup>) makes A2142 a rare “warm core”; apparently the large displacement of the cool peak by sloshing is the reason. Finally, we find a subtle narrow, straight channel with a 10% drop in X-ray brightness, aligned with the southern cold front — possibly a plasma depletion layer in projection.

## 4.1 Introduction

So far, KH eddies in the plane of the sky have been seen only in A3667 ([Mazzotta et al. 2002](#); [Vikhlinin 2011](#); [Ichinohe et al. 2017](#)). A possible eddy has also been reported at a sloshing cold front in Perseus ([Walker et al. 2017](#)), although the Perseus core is full of AGN bubbles and that feature could also be one of those. Those are the ones that can provide the most unambiguous constraints on the plasma microphysics, because the length scale of the KH instabilities can be inferred from these identifiable eddies. In this chapter, we present another example of a cold front that shows apparent KH eddies, the southern front in A2142, based on a deeper *Chandra* observation of the cluster core. In addition, we analyze a recently found cold front at a very small radius, as well as two other interesting effects: a cool peak displaced from the central galaxy, as well as a subtle channel in the cluster X-ray brightness — a phenomenon similar to that we have recently discovered in another cluster, A520 (§ 2.5.2; [Wang et al. 2016](#)).

While we concentrate on the core of A2142, where we now observe three concentric

cold fronts (at  $r \approx 12 - 340$  kpc), this cluster exhibits another cold front far outside the core, 1 Mpc from the center (Rossetti et al. 2013), outside the *Chandra* coverage. A set of multiple concentric fronts at such different radii indicates “an extreme case of sloshing”, quoting the above authors. Interestingly, A2142 has a specific entropy in the gas density peak that makes it a relatively rare “warm core” — intermediate between cool-core and non-cool-core clusters (Cavagnolo et al. 2009; Giacintucci et al. 2017). We will try to clarify if this can be related to the observed strong sloshing. A2142 also has a giant radio halo whose structure spatially correlates with the cold fronts on all scales (Venturi et al. 2017).

In § 4.2, we describe our treatment of *Chandra* data, as well as spectral and imaging analyses. In § 4.2.1, we describe the procedure we used to generate a wavelet enhanced temperature map of the cluster’s central regions. In § 4.3, we describe each of the three cold fronts in turn, including the displacement of the cool core from the BCG in § 4.3.3. We then discuss in § 4.4 our results in the context of constraining viscosity, and in § 4.5 a possible plasma depletion sheet. Finally we summarize our results in § 4.6.

At the cluster redshift of  $z = 0.089$ ,  $1''$  is 1.66 kpc for  $h = 0.7$  and  $\Omega_M = 0.3$ . Unless otherwise stated, errors in the text are given at 90% confidence.

## 4.2 X-ray data analysis

We combined the archival *Chandra* Advanced CCD Imaging Spectrometer (ACIS) observations with ObsID 5005, 15186, 16564, and 16565, omitting for convenience the short (16 ks) dataset analyzed in (Markevitch et al. 2000) (hereafter M00). ObsID 5005

(45 ks) was taken in 2005 (PI L. VanSpeybroeck) and had the cluster center in ACIS-I3; it has been analyzed by [Owers et al. \(2009\)](#) and [Johnson \(2011\)](#). The latter three (153 ks total) were taken in 2014 (PI M. Markevitch) and centered the cluster in ACIS-S3. An image from these observations have been looked at by [Walker et al. \(2016\)](#). We processed the data using CIAO (v4.9.1) and CALDB (v4.7.7), with standard event filtering procedure to mask bad pixels, filter by event grades, remove cosmic ray afterglows and streak events, and detector background events identified using the VFaint mode data. The data were then checked for background flares using the 2.5–7 keV light curve in 1 ks time bins in a cluster-free region, separately for the FI and BI chips. As a more sensitive check for faint flares, we also used the ratio of 2.5–7 keV to 9.5–12 keV counts. There were no period with strong flares. The final data we used have a total exposure of 197 ks, which is 97% of the raw exposure.

We accounted for the background following [Markevitch et al. \(2003a\)](#) and [Hickox & Markevitch \(2006\)](#), using the blank-sky data sets from CALDB. For ObsID 5005, we used the Period E dataset with an exposure of 1.55 Ms. For ObsIDs 15186, 16564, and 16565, we used the Period F dataset with an exposure of 800 ks. For both imaging and spectral analysis, the background was scaled by the ratio of the 9.5–12 keV counts (separately for front-illuminated and back-illuminated chips), which corrects for the secular background rate variability. The 90% uncertainty of the 0.8–9 keV quiescent background modeled in such a way is 3% ([Hickox & Markevitch 2006](#)), so we vary the background by this amount and include the effect in quadrature in our temperature measurement errors. The ACIS readout artifact was modeled using `make_readout_bg`<sup>1</sup> and treated as

---

<sup>1</sup>[http://cxc.harvard.edu/contrib/maxim/make\\_readout\\_bg](http://cxc.harvard.edu/contrib/maxim/make_readout_bg)

an additional background component, as in M00. We identified point sources for exclusion from our analysis by visual inspection using the 0.8–4 keV and 2–7 keV images at different binning and smoothing scales.

Spectral analysis was performed in XSPEC (version 12.9.1p). Instrument responses for spectral analysis were generated as described in Vikhlinin et al. (2005). We used the CHAV tools to generate the PHA, ARF, and RMF files for each pointing and then combined the data products. PHA files from different pointings were coadded for each of the observed data, blank-sky background, and simulated readout background, while ARFs and RMFs were weighed by the counts in the 0.5–2 keV band (where most of the events are) in the spectral extraction region.

A single-temperature fit to the whole cluster in a 4′ circle (0.4 Mpc, covers most of the S3 chip) centered on  $(\alpha, \delta) = (15:58:20.4, +27:13:52.7)$  (FK5, J2000), using the 0.8–9 keV band and the `appec*wabs` model, gives  $T = 8.0 \pm 0.1$  keV, metal abundance  $0.28 \pm 0.01$  (relative to Anders & Grevesse 1989), and absorption column  $N_H = (7.7 \pm 0.3) \times 10^{20} \text{ cm}^{-2}$ . The errors are formal errors from fitting with and the effect of the 3% uncertainty in the blank-sky background added in quadrature. The best-fit temperature and abundance are the same as those reported in M00, while the best-fit  $N_H$  is double the value  $3.8 \times 10^{20} \text{ cm}^{-2}$  from the LAB survey (Kalberla et al. 2005), which probably reflects the uncertainty of the ACIS calibration at the lowest energies — the reason for our excluding  $E < 0.8$  keV from the fits. In the analysis below, we fix the abundance and  $N_H$  to the cluster-wide best-fit values.

To make the exposure-corrected images, we created exposure maps using Alexey

Vikhlinin’s tools<sup>2</sup>, assuming the spectrum of a single-temperature plasma with best-fit parameters from the 4′-radius circle described above. These are images of effective exposure time that include vignetting and variations in detector efficiency. Varying the assumed temperature within the range found in the cluster would make little difference to the broad-band exposure map, as the counts are dominated by those around the peak of the ACIS effective area at 1–2 keV. (For narrow-band exposure maps used in § 4.2.1 it matters even less.) We divided the coadded (in sky coordinates) background-subtracted count images by the coadded exposure maps to get the final flux images.

#### 4.2.1 Temperature map of the small-scale structure

To determine the nature of the X-ray structure in the cluster core, we derived a temperature map of the core by subtracting the smoother, large-scale emission component, in order to enhance the contrasts of the small-scale features — that is, to get closer to their true temperatures. Because the precise 3D geometry of the gas in this asymmetric cluster is unknown, such a map necessarily provides only a qualitative picture of the core of A2142.

The map shown in Fig. 4.2(a) was derived following the method described in § 1.4.5. We extracted six narrow-band images in the 0.8–1–1.5–2–4–6–9 keV bands. The flux and error images were smoothed by wavelets prior to deriving the temperature map, using the same wavelet decomposition coefficients for all bands. The absorption column and metal abundance were fixed to the cluster best-fit values. The wavelet reconstruction was derived from the 0.8–4 keV image binned to 1.5″ pixels, with scales of 2.5, 5, 10, 20, 39,

---

<sup>2</sup><http://hea-www.harvard.edu/~alexey/CHAV>

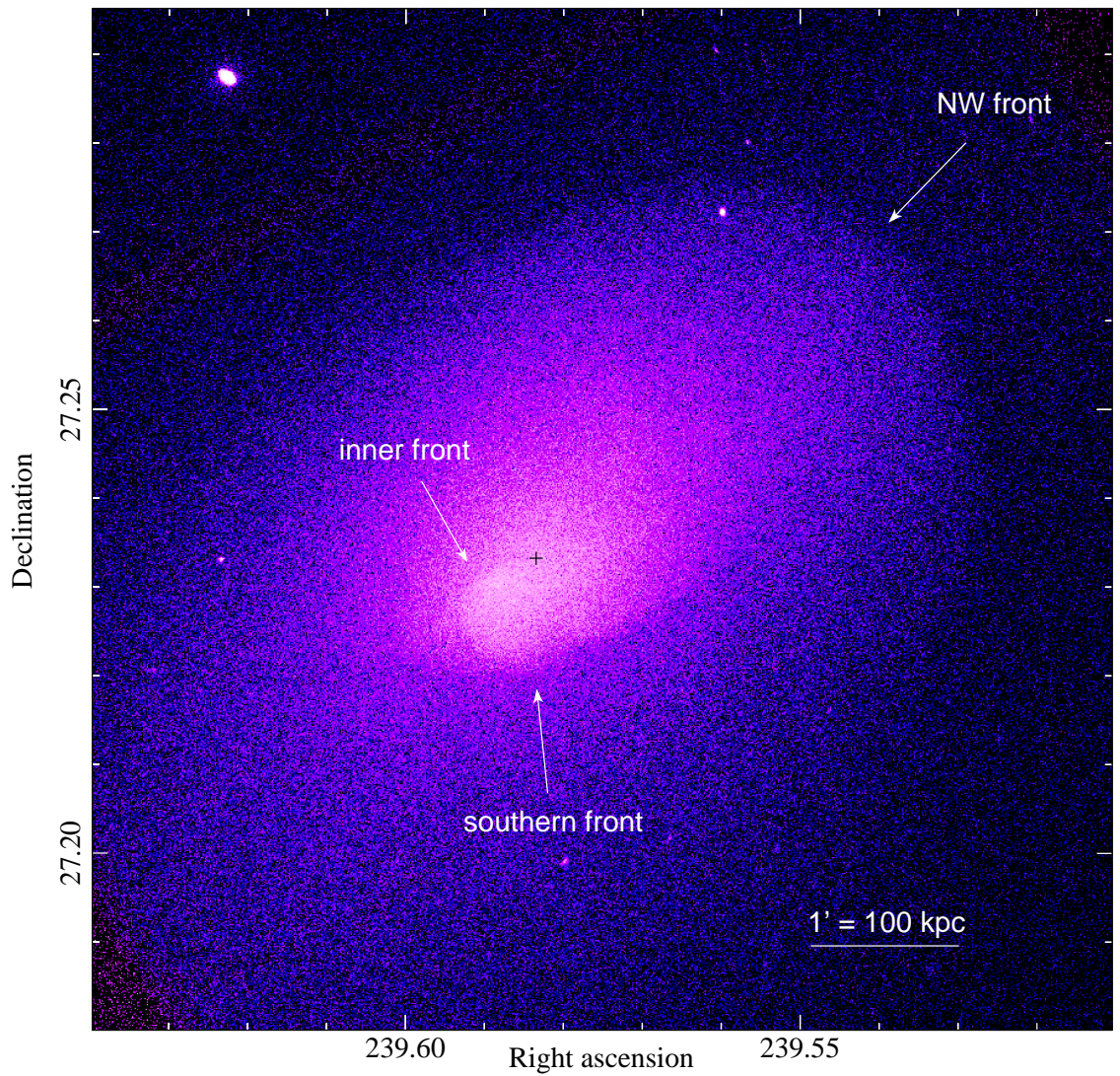


Figure 4.1: A broad view of the features we studied in A2142, shown by an unbinned 0.8–4 keV *Chandra* image (1 pixel is 0.5"). The cross marks the position of the BCG.

and 78 kpc (or 1.5, 3, 6, 12, 24, and 47''). Point sources were removed from the component images before they were coadded. Error images were treated with the same procedure.

### 4.3 Cold fronts

The 0.8–4 keV A2142 image, full-resolution without any smoothing or enhancements, is shown in Fig. 4.1. We see the two prominent brightness edges that are the first cold fronts reported in M00 (marked “southern” and “NW”). The current, much deeper image reveals that the southern front spirals inward and ends with another cold front (marked “inner”). The inner front has been noted by Johnson (2011) in the earlier *Chandra* dataset. A temperature map of this structure (Fig. 4.2(a)) confirms that the gas behind those brightness edges is cool, thus the cold front interpretation is correct. A closer look at the image reveals that the southern front branches in two, one branch apparently continuing with a similar low curvature to the east (where we will find an intriguing “channel”, § 4.5) and another one curving toward the center and the inner front. Such a pattern is predicted by hydrodynamic simulations of gas sloshing for the recently formed fronts (see, e.g., Ascasibar & Markevitch 2006, hereafter A06, and their Figure 7, panels 1.8–2.1 Gyr, or Figure 2 in ZuHone et al. 2015). At this stage, the fronts do not yet form a complete spiral pattern and still exhibit the remainders of the Rayleigh-Taylor instability that gives rise to cold fronts with successively smaller radii (A06).

It is not clear whether the NW front and its more distant opposite (Rossetti et al. 2013, outside this *Chandra* image) are part of the same sloshing pattern as the inner two or they are caused by another disturbance. A closer look at Fig. 4.1 and the unsharp-masked

image in Fig. 4.5(b), as well as the gradient image in Walker et al. (2016) hints at subtle filamentary brightness enhancements that start at the NW front and go inward, as if they were extensions of the southern front. While Walker et al. interpreted them as projected KH instability (KHI) of the NW front, they may instead be the structures surviving from the stage when the cool gas currently in the core detached from the NW front and sank inward. However, this speculation is beyond the statistical accuracy of the present dataset.

The gas density peak, which is right under the inner cold front and is the location of the coolest gas (Fig. 4.2(a)), is offset by  $\approx 30$  kpc from the BCG, which is likely to be the center of the gravitational potential. We will discuss this in § 4.3.3.

The southern cold front shows structure that resembles eddies of the KHI, predicted by hydrodynamic simulations with sufficient resolution. The NW front exhibits interesting structure consistent with such disturbances as well. We will discuss the constraints on viscosity that we can place using these observations in § 4.4. We start below with the necessary preparatory analysis of the fronts.

### 4.3.1 Southern front

We selected a sector enclosing the sharp segment of the southern cold front, as shown in Fig. 4.2(b), and extracted a surface brightness profile from the exposure-corrected image (Fig. 4.2(c)) to model the 3D gas density across the front. Our model describes the density profile inside the cold front with a power law and outside the cold front with a

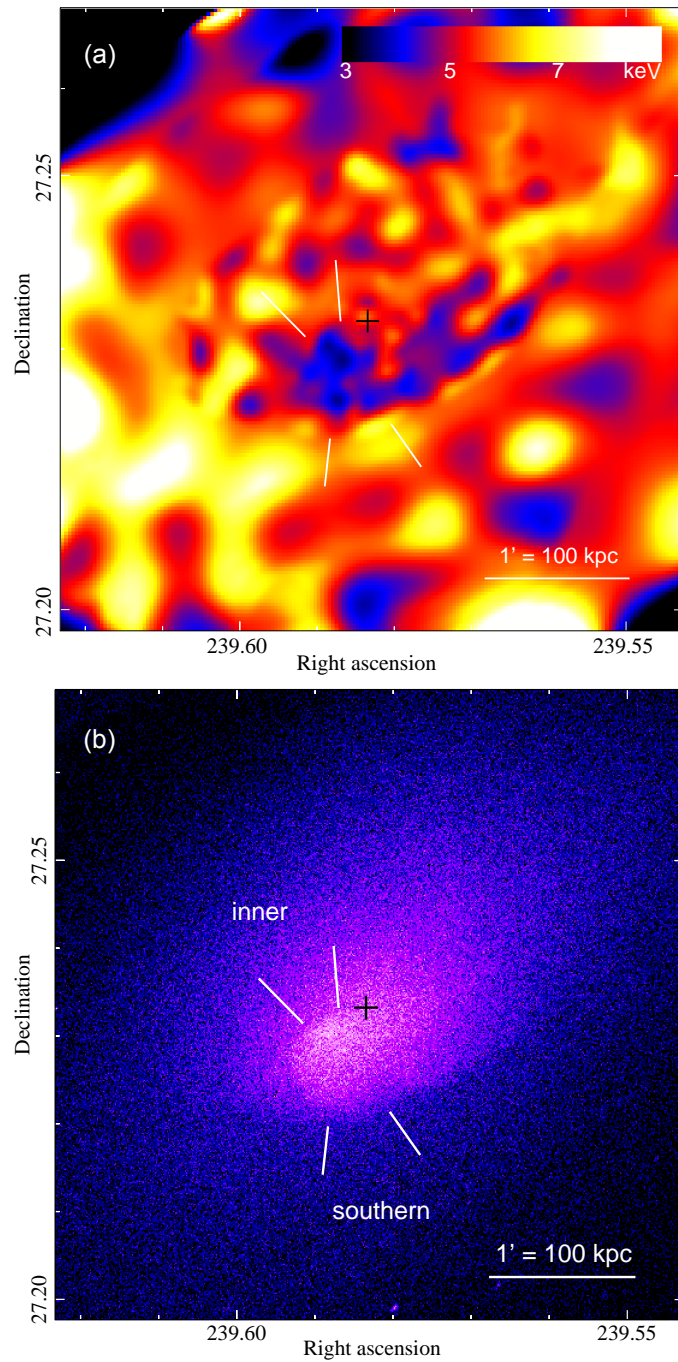


Figure 4.2: (a) Temperature map created using wavelet reconstructed narrow-band images, keeping only components on scales up to  $47''$  ( $=78$  kpc). This has the effect of deprojecting the larger-scale components for a better qualitative view of the temperature structure. A  $1''$  Gaussian was used to smooth edge artifacts without changing its appearance qualitatively. (b) 0.8–4 keV image of the same zoom as (a). The white lines indicate the width of the sectors used to model the surface brightness profiles of the southern and inner cold fronts. The cross marks the BCG position.

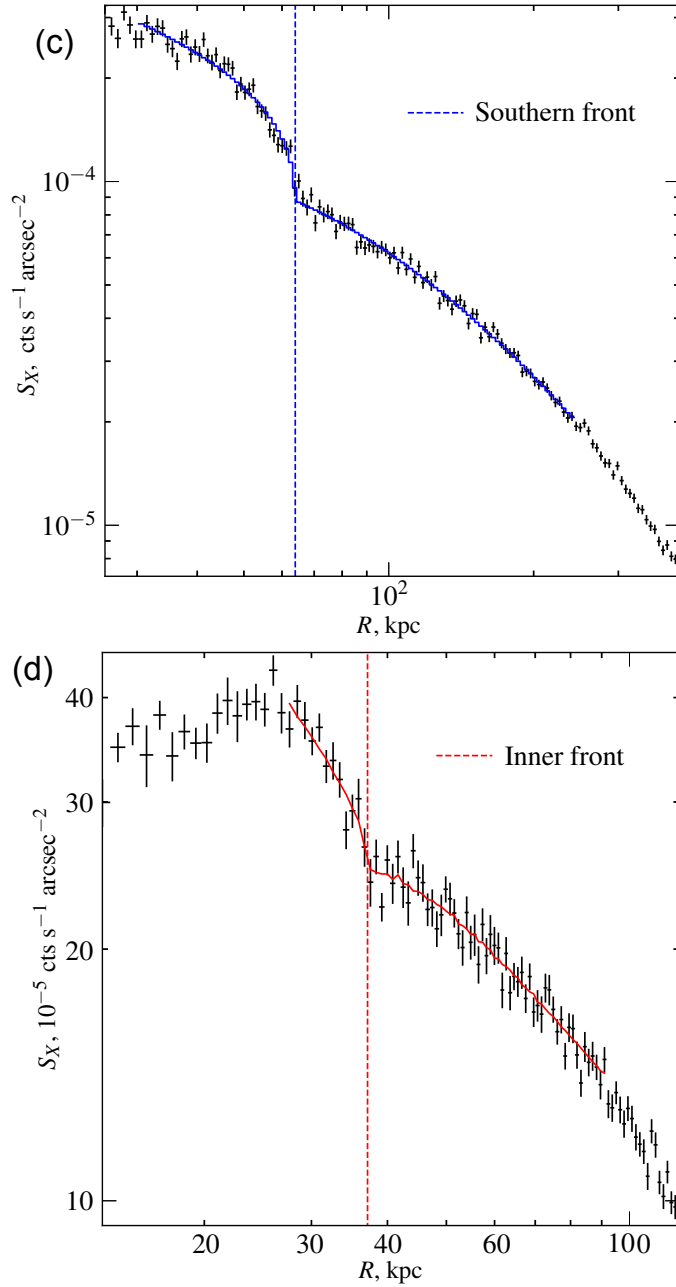


Figure 4.2: (—*continued.*) (c) X-ray surface brightness profile taken across one of the suspected KH eddies in the southern front, in the region shown in (b). Blue solid line is the projection of the 3D density model, using a power law inside the cold front and a beta model profile outside (see § 4.3.1 for details). It is drawn for the range of  $R$  used in the fitting. The dashed line marks the best fit position of the edge. (d) Surface brightness profile of the inner front in the sector shown in (b). Red solid line is the projection of the 3D density model (see § 4.3.3 for details). The dashed line marks the best fit position of the edge.

beta model, with a density jump at the cold front:

$$n(r) = \begin{cases} n_0(r/r_J)^\alpha & , r \leq r_J \\ \frac{n_0}{x} \left[ \frac{1+(r/r_c)^2}{1+(r_J/r_c)^2} \right]^\beta & , r > r_J. \end{cases} \quad (4.1)$$

Here,  $r_J$  is the radius of the density jump,  $x$  is the density jump factor,  $n_0$  is the density on the inside of the jump, and  $r_c$  is the core radius of the beta model. The model is centered at the center of curvature of this section of the cold front (it is close to the X-ray peak), and we assume spherical symmetry of the model (i.e. the same curvature of the front along the l.o.s. as in the sky plane). The best-fit parameters are given in [Table 4.1](#). The model fits the profile very closely, showing a sharp jump at the cold front ([Fig. 4.2\(c\)](#)).

We then extracted spectra from regions in the same sector on both sides of the southern front and fitted their projected temperatures in XSPEC:  $T_{\text{cold,proj}}$  from a 10'' wide annular segment inside, and  $T_{\text{hot,proj}}$  from a 15'' wide annular segment outside, allowing 1'' of clearance from the front position on either side. Using the APEC normalization, we determined the absolute density by comparing it with the model's emission measure  $\int n_H n_e dV$ , assuming  $n_e = 1.17 n_H$ . To evaluate the 3D gas temperature inside the cold front,  $T_{\text{cold,deproj}}$ , we scaled the best-fit model in the outside region by the ratio of our model's emission measure for the outside component that is projected into the inner segment. We then refit the inner spectrum with this component added and held constant. Finally, we used XSPEC to check if  $x$  and  $n_{H,0}$  needed to be corrected for the difference in 0.8–4 keV emissivity in the presence of the temperature jump across the front (a small factor not included in the brightness profile fitting procedure). For the best-fit temper-

Table 4.1: Best fit cold front model parameters for the southern and northwestern cold fronts.  $n_{H,0}$  is given as the model density on the inside of the jump, calculated using density and temperature of the outer component. Errors are 90%.

Location	$n_{H,0}$ $10^{-3} \text{ cm}^{-3}$	$r_J$	$x$	$\alpha$	$\beta$
Southern	$16.4 \pm 0.16$	$63.9^{+0.6}_{-0.5}$	$1.87 \pm 0.1$	$-0.51 \pm 0.09$	$-0.60^{+0.04}_{-0.05}$
NW1	$4.31 \pm 0.04$	$175.0 \pm 1.0$	$2.14^{+0.09}_{-0.10}$	$-0.42 \pm 0.04$	$-0.71^{+0.05}_{-0.06}$
NW2	$4.31 \pm 0.04$	$174.6^{+1.0}_{-1.7}$	$2.07^{+0.11}_{-0.10}$	$-0.50 \pm 0.04$	$-0.66 \pm 0.05$

Location	$r_c$ kpc	$T_{\text{cold,proj}}$ keV	$T_{\text{cold,deproj}}$ keV	$T_{\text{hot}}$ keV
Southern	$75^{+16}_{-15}$	$6.9^{+0.8}_{-0.5}$	$5.8^{+1.1}_{-0.9}$	$9.0^{+1.1}_{-0.9}$
NW1	$218^{+39}_{-37}$	$8.6^{+1.2}_{-0.8}$	$7.9^{+1.6}_{-1.3}$	$10.5^{+1.9}_{-1.2}$
NW2	$178^{+41}_{-43}$	$7.2^{+0.9}_{-0.7}$	$6.1^{+1.1}_{-0.9}$	$10.5^{+2.2}_{-1.3}$

atures, the factor is  $<0.1\%$  so no correction was applied. The temperatures are given in [Table 4.1](#). The gas pressure across the front is continuous within the 90% statistical uncertainties.

### 4.3.2 Gas velocity at the southern front

For our instability analysis below, we now try to estimate the gas velocity at the front. Within the simple subcluster-stripping picture of the fronts, [M00](#) used the pressure profile to constrain the velocity of the flow around the front, ascribing any difference of thermodynamic pressures across the front to ram pressure. They obtained a rough upper limit  $v < 400 \text{ km s}^{-1}$  for the southern front. A more accurate way to estimate the front velocity from the pressure profile is proposed in [Vikhlinin et al. \(2001a\)](#) for A3667. However, we now think that (at least) the southern and the inner fronts are, in fact, sloshing fronts with gas flowing tangentially (see, e.g., [A06](#) for the possible flow patterns). In particular, the cool gas under the southern front is likely to be flowing from NW along the inward spiral.

In this picture, we can try to estimate the velocity of the curved tangential flow from the centripetal acceleration, as was done in [Markevitch et al. \(2001\)](#) and [Keshet et al. \(2010\)](#). In the simplest approximation, the outer gas is stationary while the cold front gas inside the front is in circular orbit with velocity  $v$  in the cluster gravitational potential. Then

$$\frac{GM(r')}{r'^2} = -\frac{1}{\rho} \frac{dp}{dr} + \frac{v^2}{r'}, \quad (4.2)$$

where  $M$  is the cluster total mass within the radius  $r'$ ,  $\rho$  is gas density, and  $p$  is thermo-

dynamic pressure. Here the  $r$  coordinate is from the center of the model density profile (the center of curvature of the cold front) and  $r'$  is from the center of mass (the BCG). At the cold front, they are at an angle of only  $15^\circ$ , so  $dr'/dr = 0.97$  there, and we can ignore this distinction for an approximate estimate. The left-hand side of [Eq. 4.2](#) is continuous over the cold front, because the cluster total mass distribution (dominated by dark matter) is smooth. However, the moving gas inside the cold front effectively feels a lower mass. Therefore, we can check for a difference in the total mass derived under the hydrostatic equilibrium assumption (e.g., [Sarazin 1988](#)) on the inside and outside of the cold front, and attribute it to the centripetal term. Using the gas density model of [Eq. 4.1](#) and the temperatures on two sides derived above (assumed constant at those values on both sides), we calculated the difference between the second term in [Eq. 4.2](#) to be  $(4.0 \pm 2.7) \times 10^3 \text{ km}^2 \text{ s}^{-2} \text{ kpc}^{-1}$ , which corresponds to a  $\approx 35\%$  drop in the apparent total mass on the inside of the cold front. The hydrostatic mass given by the outer part of the model (i.e., the true mass under our assumptions) is  $(1.5 \pm 0.3) \times 10^{13} M_\odot$  within  $r' = 75 \text{ kpc}$  of the BCG.

This gives a tangential velocity of the cold gas of  $(550 \pm 190) \text{ km s}^{-1}$ , where the errors are statistical and include the uncertainties of the parameters  $\alpha$ ,  $\beta$ ,  $r_J$ ,  $r_c$ ,  $T_{\text{cold,deproj}}$ , and  $T_{\text{hot}}$  ([Table 4.1](#)). If we use a smaller radius of curvature such as that of the cold front at this position, we get a lower value but not by much, because of the square root. Given the unknown 3D geometry and a number of assumptions, this is, of course, only a qualitative estimate with a factor 2 accuracy at best. Furthermore, if the outer gas also rotates but in the opposite direction, one can in principle have a much higher *relative* tangential velocity and still satisfy [Eq. 4.2](#). While such a scenario is unlikely considering how the sloshing

fronts form — we do not expect flows faster than Mach  $\sim 0.3\text{--}0.5$  — a conservative upper limit on the relative velocity is probably the sound speed in the outer gas ( $1500 \text{ km s}^{-1}$ ), from the fact that we do not see any shocks immediately outside this cold front. We will use the velocity estimate of  $550 \text{ km s}^{-1}$  in § 4.4 below.

### 4.3.3 The displaced gas peak and the inner front

We noted above that the gas density peak is offset  $\sim 30 \text{ kpc}$  from the position of the brightest cluster galaxy (Fig. 4.1, Fig. 4.2(b)). Such offsets are rare but not unknown — they have been seen, e.g., in A644 (Buote et al. 2005), Ophiuchus (Million et al. 2010; ZuHone et al. 2010; Hamer et al. 2012; Werner et al. 2016b), A1991 (Hamer et al. 2012), and Zw1742+33 (Ettori et al. 2013). However, to our knowledge, this is the largest offset seen in a cluster that still has a cool density peak. A comparable offset of  $20 \text{ kpc}$  is seen in Zw1742+33, but that cluster also shows evidence of AGN X-ray cavities emanating from its BCG, which has an active nucleus seen in the radio and X-rays. In comparison, the BCG in A2142 is currently very faint in the radio (Venturi et al. 2017) and is not detected in the X-ray; we see no evidence for X-ray cavities either. Thus, the offset peak that we observe is clearly the result of sloshing and of the merger that set it off.

We subtracted the cool sloshing structure from the X-ray image by wavelet decomposition to see the larger-scale X-ray gas distribution. After the subtraction of components  $20 \text{ kpc}$  and smaller (using the same decomposition as § 4.2.1), we are left with the image shown in Fig. 4.3(a). The contours of the subtracted small-scale structure are overlaid. We see a symmetric elliptical X-ray structure centered very near the BCG. This is consistent with a picture where the BCG is the center of the gravitational potential of the cluster,

and the gas beyond the inner sloshing structure is largely in hydrostatic equilibrium with it (this does not exclude slower motions that can accompany the outer cold fronts). The gravitational lensing map of [Okabe & Umetsu \(2008\)](#) does show the main mass peak of the cluster near this BCG. The second brightest galaxy seen in [Fig. 4.3\(b\)](#), which was thought in [M00](#) to be the center of a merging subcluster, appears not to be physically related to the cluster, based on its high peculiar velocity ( $1840 \text{ km s}^{-1}$  from the BCG, [Oegerle et al. 1995](#)) and lack of a mass concentration ([Okabe & Umetsu 2008](#)).

We will now model the inner cold front in order to derive the parameters of the gas in the offset density peak. A surface brightness edge near the peak of the X-ray emission spans a sector from east to north ([Fig. 4.2\(b\)](#)). The contrast in X-ray brightness and projected temperature is highest in the northeastern quadrant, and the edge disappears to the west. It is a cold front, as shown by the temperature map ([Fig. 4.2\(a\)](#)). We extracted a brightness profile ([Fig. 4.2\(d\)](#)) in the sector shown in [Fig. 4.2\(b\)](#) and model it as follows. The density profile inside the edge is centered on the center of curvature of the front and is a power law. The outer gas is modeled with an ellipsoidal component following a power law profile, centered on the BCG. The ellipticity of the outer component model is achieved simply by rescaling the coordinate of the long axis before calculating the model density in 3D. Both position angle and ellipticity of the outer component were deduced from the X-ray brightness contours of the remaining cluster emission after we subtracted the core structure (as described above), and fixed during the fit. Since the two density components have different centers, we could not just calculate a 1D projected model. Instead, we projected the model onto the same image plane as the flux image and extracted a brightness profile in the same sector. The best fit model is shown in

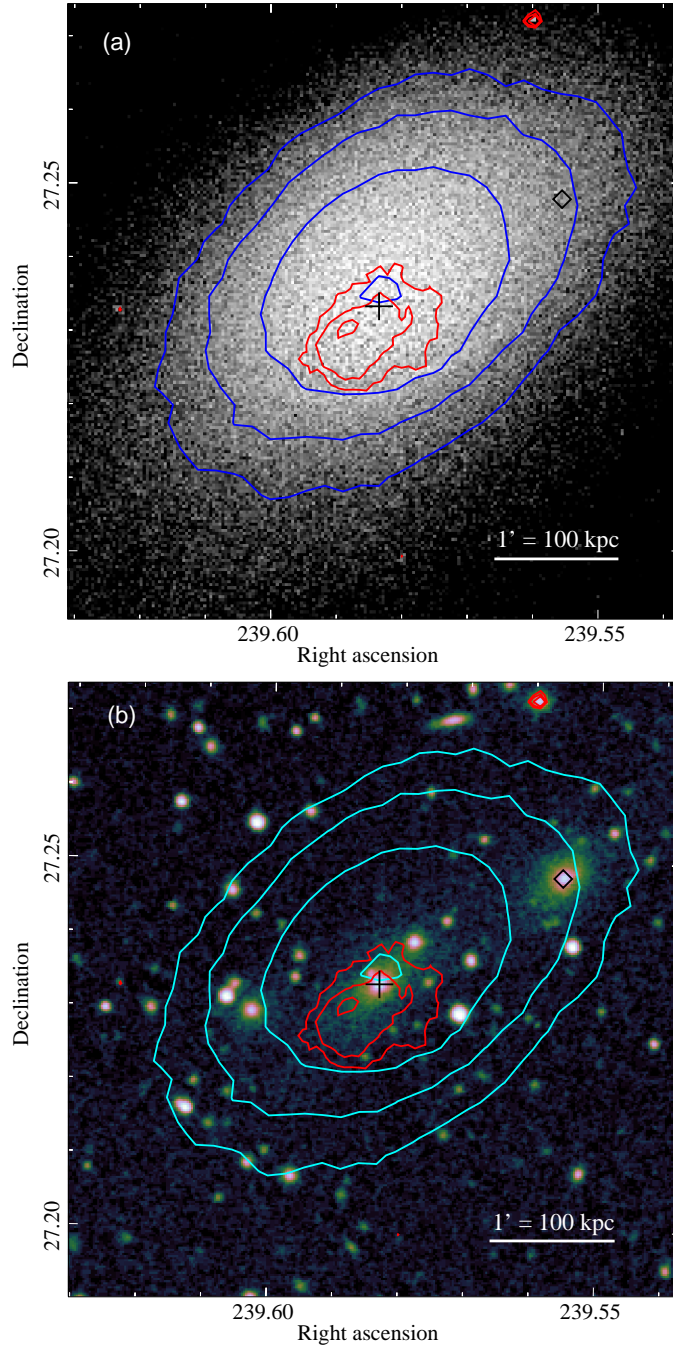


Figure 4.3: (a) Residual 0.8–4 keV flux, binned to  $1.5''$  pixels, after subtracting wavelet components 20 kpc and below. (b) Optical image from Digital Sky Survey image archive, showing the main BCG (marked by the cross) and its neighborhood. The position of the second brightest galaxy is also shown (marked by the diamond). The blue contours show the position of the peak and the shape of the residual emission in (a), with levels in  $1.4\times$  steps. The red contours show the X-ray peak and shape of the small-scale structures, with levels in  $2\times$  steps. They are derived from a wavelet reconstruction of the small scale structures using scales up to 39 kpc. The wavelet reconstruction uses the same decomposition as described in § 4.2.1.

Fig. 4.2(d). To determine a deprojected central temperature, we first fitted the spectrum extracted from a sector, 17 kpc wide, just outside the cold front. Then, we created an image of the ellipsoidal component with a spherical cutout for the core and used it to normalize the projected contribution to an inner sector, 10 kpc thick, inside the front. We then fixed this contribution at the best-fit outer temperature and fit the inner temperature. Finally, we use the APEC model normalization to derive the gas densities in 3D as we did in § 4.3.1.

Our deprojected density just behind the cold front (near the peak) is  $n_H \approx 2.3 \times 10^{-2} \text{ cm}^{-3}$  and temperature  $T = 4.0_{-0.6}^{+0.8} \text{ keV}$ . The gas specific entropy index, commonly defined in the cluster field as  $K = T_e n_e^{-2/3}$ , is  $K \approx 49 \text{ keV cm}^2$  (statistical errors are probably meaningless because the systematic uncertainties dominate). The true value at the peak can be slightly lower because our spectral fitting region does not resolve the peak. For the gas immediately outside this cold front, our model gives  $K \approx 120 \text{ keV cm}^2$ . We note that our value for the central entropy index is lower than  $58 \pm 2 \text{ keV cm}^2$  in [Giaccintucci et al. \(2017\)](#) from the same dataset; however, the difference is expected because those authors have used a different definition of “central entropy” in order to be consistent with [Cavagnolo et al. \(2009\)](#), who combined the projected temperature with the 3D gas density, whereas both our quantities are deprojected.

The above small difference notwithstanding, our value of the central entropy places A2142 in the gap between the cool-core and non-cool-core clusters ([Cavagnolo et al. 2009](#)). This is apparently related to strong sloshing in this cluster. As shown by [ZuHone et al. \(2010\)](#), sloshing of a cool core can balance radiative cooling, except for the very central region, by facilitating mixing with the higher-entropy gas from outside the core. Once

the gas peak is displaced from the minimum of the gravitational potential, it becomes even more prone to mixing, because it expands (which reduces the density contrast) and because the stabilizing effect of gravity is removed. We may have caught A2142 at the moment of dissolution of its former cool core by sloshing. The displacement of the gas peak should also have deprived the cD galaxy of the accreting cool gas for a significant period of time, which is why it does not exhibit an AGN, similarly to Ophiuchus and to most clusters without cool cores.

#### 4.3.4 Northwest front

Upon close inspection, the NW front (Fig. 4.4) shows interesting structure, which includes a “boxy” shape and apparent multiple edges at its nose. We extract brightness profiles in sectors NW1 and NW2 shown in Fig. 4.4(a) and fit them as in § 4.3.1 with the density model given in Eq. 4.1, centered on the front center of curvature (same for both sectors). The best-fit parameters, along with the gas temperatures across the front, are given in Table 4.1. For the observed temperature jumps, a 1% reduction was applied to the jump factor to correct for the higher 0.8–4 keV emissivity at the lower deprojected temperature. These two segments of the cold front are visually similar, have the same radius of curvature, and the brightness jump can be traced by the same circle. Their model parameters are therefore very comparable, and indeed their best-fit density jump positions, jump factors, and outer model index  $\beta$  are consistent with being the same. The inner index  $\alpha$  and the beta model core radius  $r_c$  are statistically different, but this is expected because of the cluster’s ellipticity. The brightness profile and the the best-fit model for NW1 are shown in Fig. 4.4(b) (the NW2 profile is not shown as the fit is good

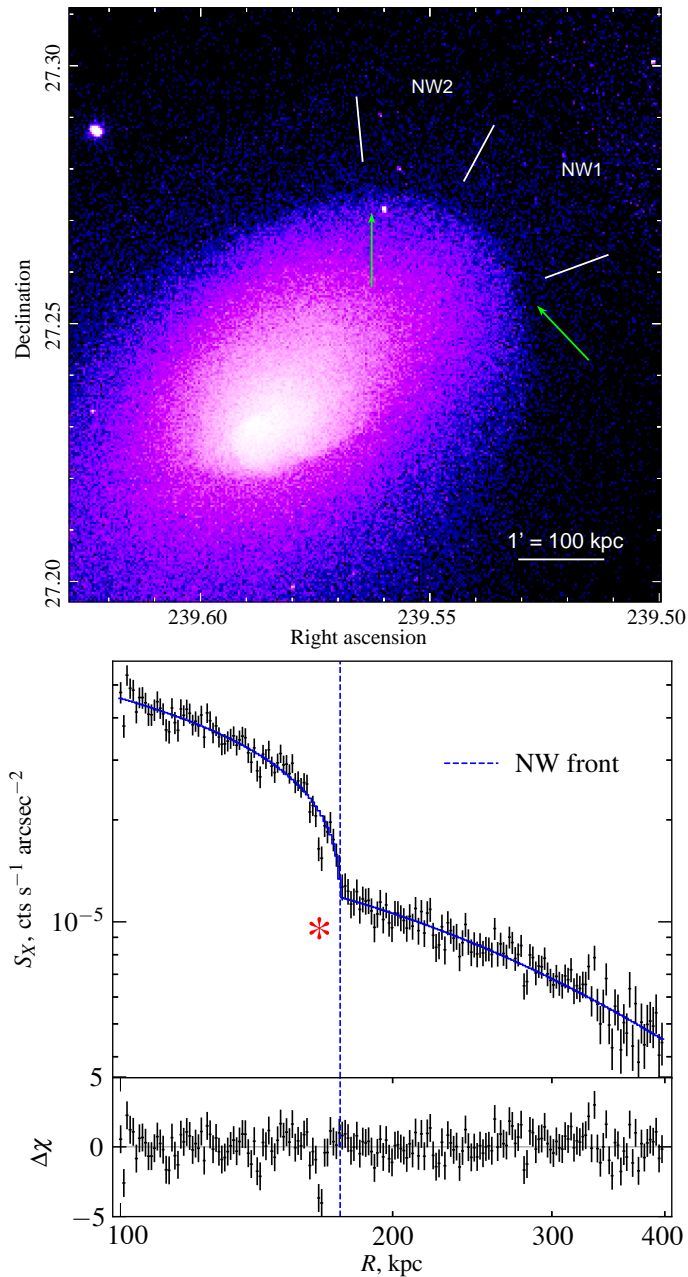


Figure 4.4: (a) The NW cold front, with the brightness profile sectors NW1 and NW2 marked, on a 0.8–4 keV image binned to  $1.5''$  pixels. The green arrow to the left points to the “boxy” shape of the front. The continuation of the right green arrow is the feature that shows as a dip in surface brightness. (b) Brightness profile in the NW1 sector. There is a highly significant drop in X-ray brightness, at the radius indicated by the red asterisk, 8–10 kpc inside the best-fit position of the density jump (dashed line). The best-fit positions are statistically identical in the two sectors.

and there is nothing special about it.) Notably, the NW1 brightness profile shows a  $4\sigma$  dip — 25% below the model — 8–10 kpc behind the front. This feature is seen in the image in Fig. 4.4(a) (on the continuation of the right arrow). Along with the boxy shape (left arrow), it looks just like the deformations expected from KHIs (e.g., Roediger et al. 2013a, see their Figure 6) and seen in a few other clusters. In particular, multiple edges would be the KH eddies that develop along the line of sight.

#### 4.4 Constraints on plasma viscosity

Even without any image enhancements, the X-ray image of the southern front (Figures 4.1, 4.2(b)) shows a wavy structure that looks like the classic KHI at the interface of two gas layers with velocity shear. In Fig. 4.5(a), we show a slightly enhanced image of the small-scale structure by subtracting the large-scale ( $\geq 26$  kpc) wavelet components from the raw image. In Fig. 4.5(b), we instead apply the usual unsharp mask. Both images reveal two prominent bumps of the cold front surface that we interpret as two developed KH eddies, spaced by 55 kpc, with a crest-to-trough amplitude of 13–15 kpc (green dashes in Fig. 4.5(b)). This amplitude is a lower limit because projection can only make it look smaller. The high contrast of the edge suggests that we are getting an edge-on view of the shear layer. This is only the second cold front that affords us a good, direct, and unambiguous view of the KH eddies; the other one is A3667 (Vikhlinin 2011; Ichinohe et al. 2017).

If these are indeed KH eddies, they present an opportunity to constrain the ICM effective viscosity. In our picture, the gas inside the southern cold front is flowing along

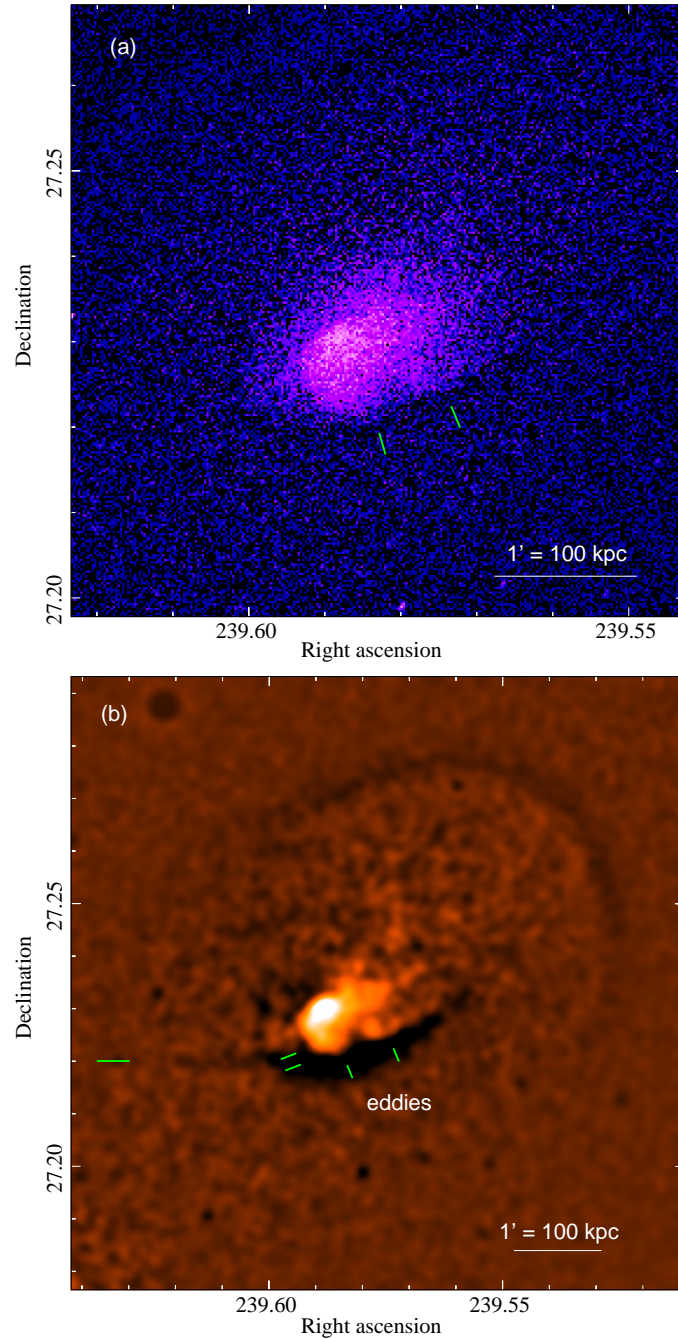


Figure 4.5: Zooming in on the suspected Kelvin-Helmholtz eddies at the southern cold front. (a) Wavelet decomposition was used to remove emission from components on scales larger than the KH eddies,  $16'' (=26 \text{ kpc})$  and up, by subtracting them from the 0.8–4 keV image binned to  $1''$  pixels. The two green ticks mark the crests of the KH eddies. (b) Unsharpmasked version of the 0.8–4 keV image, created by subtracting one image smoothed by a  $\sigma=12''$  gaussian kernel from a second image smoothed by  $\sigma=3''$ , so as to highlight features on scales in between. The additional pair of green ticks mark the crest-to-trough scale of the eddies. The horizontal green line to the left points along the channel discussed in § 4.5.

the curved edge from the NW and spirals inward with the velocity that we estimated in § 4.3.2, while the outer gas has a negligible velocity. Roediger et al. (2013b) (hereafter R13) performed a numerical study of the growth of KHIs on cluster cold fronts for a range of values of isotropic viscosity (under the assumption of no magnetic fields) both Spitzer-like with strong temperature dependence as well as temperature-independent. They covered a range of gas parameters that included the A2142 southern front — in fact, they used it as one of their fiducial cases (using the early M00 results that did not show the eddies). While the R13 simulations are 2D, they should provide a good qualitative approximation for the flow geometry expected at the cold front. Thus, all we need is to find where our new results fit in the R13 study to derive an estimate of the viscosity under their assumptions. We will try to constrain the isotropic Spitzer-like viscosity.

A full Spitzer viscosity would suppress the growth of KHI on small scales, so that only the perturbations of the interface between the two fluids larger than a critical wavelength can grow (R13, their Eq. 28):

$$\lambda_{\text{crit}} = 70 \text{ kpc} \left( \frac{\text{Re}_{\text{crit}}}{30} \right) \left( \frac{U}{500 \text{ km s}^{-1}} \right)^{-1} \times \left( \frac{n_e}{9 \times 10^{-3} \text{ cm}^{-3}} \right)^{-1} \left( \frac{kT_{\text{ICM}}}{9.0 \text{ keV}} \right)^{5/2}, \quad (4.3)$$

where the density and temperature are those observed on the hotter side of the front from Table 4.1 (because the temperature dependence of the Spitzer viscosity makes that side dominate the effect),  $U$  is the relative shear velocity of the gases on two sides of the cold

front and  $\text{Re}_{\text{crit}}$  is a Reynolds number defined for the KHI as

$$\text{Re} \equiv \frac{\lambda U}{\nu}, \quad (4.4)$$

where  $\nu$  is the kinematic viscosity. The full Spitzer viscosity is (Spitzer 1962; Sarazin 1988)

$$\mu = 6100 \text{ g cm}^{-1} \text{ s}^{-1} \left( \frac{kT}{9.0 \text{ keV}} \right)^{5/2} \left( \frac{\ln \Lambda}{40} \right)^{-1}, \quad (4.5)$$

where  $\nu = \mu/\rho$ , and the Coulomb logarithm  $\ln \Lambda \approx 37$  for the density and temperature we measure outside the southern cold front.

Based on simulations, R13 showed that for Spitzer-like viscosity, a conservative value is  $\text{Re}_{\text{crit}} = 30$  to suppress KHI. We do see a developed KHI, so for our wavelength,  $\text{Re} > 30$ . To place a somewhat more accurate lower limit on the Reynolds number, and thus an upper limit on the viscosity, we compare our eddies with those in the R13 simulations at a similar growth stage. Their grid of simulation snapshots for different Reynolds numbers, and at different times, are shown in Fig. 4.6. It shows the development of KHI for different Reynolds numbers and the interface parameters very close to ours (their density contrast is 2 vs. our 1.9 and their  $M = 0.5$  vs. our rough estimate of  $0.36 \pm 0.12$ ). For our front, we can use the peak-to-peak distance to measure the KHI  $\lambda \simeq 55$  kpc. The amplitude (half of the crest-to-trough distance) appears to be at least  $0.10\text{--}0.12\lambda$ . There are not enough photons to resolve the small-scale features in the eddies, such as the expected turning-over of the tip of the eddy, though observers with imagination would see a hint of this in the wavelet-subtracted image.

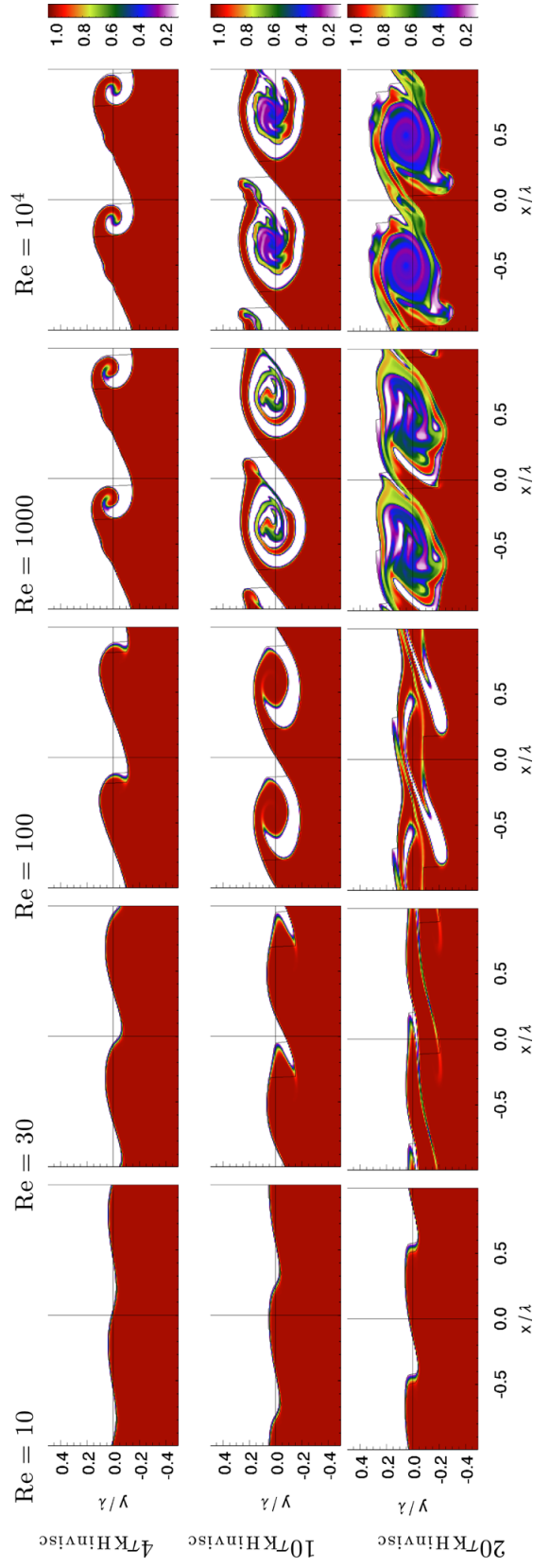


Figure 4.6: Slices from simulations with Spitzer viscosity, density ratio 2, and shear flow of Mach 0.5. Reynolds number increases from left to right, while time evolves from top to bottom. We compare these with the scale of the eddies in the southern front of A2142, which resemble the  $Re=30$  and  $Re=100$  at  $4\tau_{KH}^{invisc}$  the most. (From [Roediger et al. 2013b](#), Figure 8.)

We can estimate the time that the eddies had to grow to their present amplitude.

The inviscid KH timescale (R13, their Equations 2-3) is

$$\tau_{\text{KHinvis}} = \frac{\sqrt{\Delta} \lambda}{2\pi U}, \quad (4.6)$$

where

$$\Delta = \frac{(\rho_{\text{cold}} + \rho_{\text{hot}})^2}{\rho_{\text{cold}}\rho_{\text{hot}}} \quad (4.7)$$

is related to the growth time of the eddies estimated from  $t = L/U$ , by

$$\frac{t}{\tau_{\text{KHinvis}}} = \frac{2\pi L}{\sqrt{\Delta}\lambda}. \quad (4.8)$$

If we take the distance  $L$  that the perturbations have traveled along the front to be from the crests of the eddies to the eastern side of the front,  $L \approx 50\text{--}100$  kpc and  $t \approx 3\text{--}6\tau_{\text{KHinvis}}$ .

If we compare our eddy amplitude to R13 at this early growth stage (see their Figure 8 and the left panel of Figure 10), they look similar to the case with  $\text{Re} = 100$  or above and rule out Reynolds numbers much lower than that. We note that the R13 simulations assumed uniform density on each side of the interface, whereas our density increases toward the cluster center (away from the interface) and changes noticeably on the scale of the disturbance. This is likely to decrease the depth of the troughs compared to the simulated case, so the above estimate should be conservative.

To convert this to a constraint on the viscosity, Eq. 4.4 and Eq. 4.5 can be combined:

$$\frac{\mu_S}{\mu} = 5 \left( \frac{n_H}{9 \times 10^{-3} \text{ cm}^{-3}} \right)^{-1} \left( \frac{kT_e}{9.0 \text{ keV}} \right)^{5/2} \left( \frac{\ln \Lambda}{40} \right)^{-1} \times \left( \frac{\text{Re}}{100} \right) \left( \frac{\lambda}{55 \text{ kpc}} \right)^{-1} \left( \frac{U}{500 \text{ km s}^{-1}} \right)^{-1}. \quad (4.9)$$

Here we again used the values of the gas density and temperature on the hotter side of the front, the shear velocity that we estimated in § 4.3.2, and the above wavelength and Reynolds number of the KHI. The velocity of the flow is the most uncertain parameter for our constraint, but even if we use a very conservative upper limit of 1500 km s<sup>-1</sup> (§ 4.3.2), the viscosity should still be lower than Spitzer.

The NW front also shows hints of KHIs, including the boxy shape of the front and the apparent double density edge seen in projection (§ 4.3.4). They are not seen directly in the plane of the sky as the southern front eddies, so any constraints from them would be more uncertain than those above. However, the NW edge samples a factor 4 different gas density and possibly a different velocity, so it may be interesting to perform a joint study of the two edges, perhaps using hydrodynamic simulations to reproduce their morphology and better constrain the flow velocities.

The R13 simulations have a major omission — they do not include magnetic fields, which we know are present in the intracluster plasma and, furthermore, should be significantly amplified and stretched along the cold front surface because of the expected draping (Ettori & Fabian 2000; Vikhlinin et al. 2001a; Lyutikov 2006; Dursi & Pfrommer 2008). ZuHone et al. (2015) showed via high-resolution magnetohydrodynamic (MHD) simulations that in the context of sloshing cold fronts in clusters, isotropic Spitzer vis-

cosity reduced by a factor  $\sim 0.1$  produces similar-looking cold fronts as the anisotropic Braginskii viscosity that describes the magnetized plasma. Thus, our estimate of the effective viscosity of  $< 1/5$  Spitzer is in agreement with full anisotropic viscosity in the presence of the magnetic fields.

## 4.5 X-ray channel

There is a subtle, long X-ray brightness channel that extends from the the middle of the southern cold front to the east. We selected the contrast in the unbinned X-ray image shown in Fig. 4.7(a) to emphasize this linear depression. The unsharp-masked image in Fig. 4.5(b) helps to see the feature’s location. It is not a residual artifact of any ACIS chip gaps or edges, which are corrected for in all our images. Further, in this mosaic of slightly different pointings, the feature does not overlap with any chip gap or edge. Even if the exposure maps were significantly inaccurate, the amplitude of the effective exposure variations over the channel region that it corrects for is  $< 2\%$ , while the depth of the channel is much greater. The channel is aligned with the southern cold front (with its branch that does not curve toward the center but continues eastward, § 4.3). While the channel is most apparent to the east of the front, it may continue west, wrapping around the southern front. However, the much greater brightness gradient associated with the front there, as well as the KH eddies, preclude the detection of a subtle dip, because the baseline brightness is very uncertain.

While large, apparently significant deviations, some arranged in patterns, are expected in a noisy image with many independent pixels (the “look elsewhere” effect), this

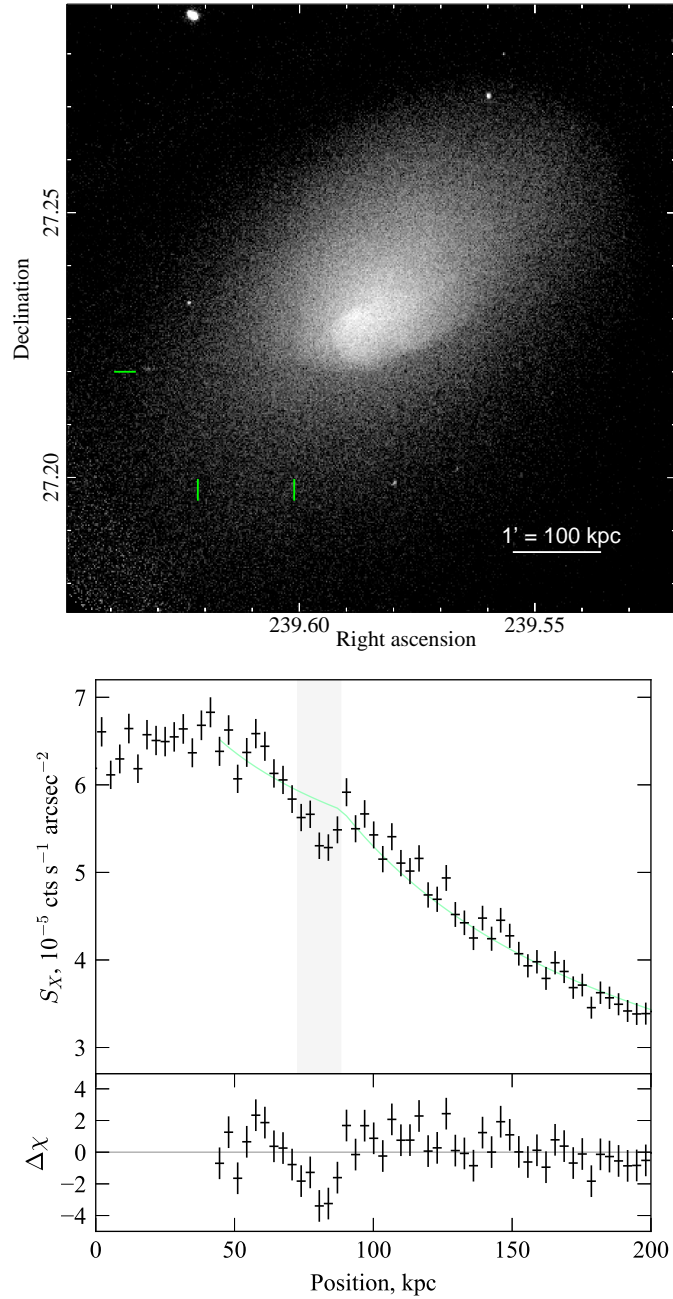


Figure 4.7: (a) Image in the 0.8–4.0 keV band, binned by  $1''$ , with colors selected to better show the channel. The green horizontal tick shows the position of the channel, which can also be seen in the unsharp-masked image in Fig. 4.5(b). The vertical ticks mark the span of the rectangular band used to derive the brightness profile shown in panel (b). The position coordinate in the profile runs from north to south (zero is arbitrary). Error bars for surface brightness are  $1\sigma$ . The shaded band indicates the apparent width of the channel. The green line shows a simple best-fit generic model that would represent a break (but no dip or a jump up) in the density profile, and residuals in the lower panel are for this model.

apparent linear feature is not found at a random place, but rather at a continuation of a prominent cold front. So it is likely to be a real structure.

We selected a section of the channel 110 kpc long, where the channel is unobstructed by brighter features, and extracted a brightness profile across it in a strip indicated by the tick marks in Fig. 4.7(a). The width of the channel is about 15 kpc. The brightness profile is shown in Fig. 4.7(b), where each bin is 3.3 kpc (2'') wide. To quantify the dip amplitude, we performed a simple fit of the brightness in the vicinity of the dip with a broken power-law model (which would represent a break in the density profile, but not allowing for a dip or a density jump up or down at the break), shown in green. There is a very significant  $\sim 9\text{--}12\%$  depression in the surface brightness at the center of the channel, where two bins are each  $>3\sigma$  below the model and below the brightness in bins immediately to the right (outwards).

The origin of such a density depression is not immediately clear. Simply projecting any number of monotonically declining brightness profiles of any shape would not create a brightness depression (but could create multiple brightness edges, as seen elsewhere in A2142) — as long as the density gradients point in the same general direction of the cluster center. One can imagine two cold fronts *facing* each other, with their gradients in the opposite directions, as in two subcluster cores about to collide and a low-density layer between them. However, based on the X-ray image, such a scenario is clearly not the case in A2142. Perhaps some other unexpected gas geometries could emerge in a merging cluster.

If we take the premise that the feature is indeed due to a density depression, not the presence of an edge-like profile facing the opposite direction, the geometry of this channel

has to be a relatively thin sheet of lower-density gas, seen along its edge. If we consider the surface brightness profile of a NE-SW cross section of the cluster at the position of the channel, we must empty of gas the central 35 kpc interval along the l.o.s. to remove 10% of the flux. Since the channel cannot be completely devoid of gas, the true extent along the l.o.s. should be significantly greater.

We have reported a similar subtle channel in the merging cluster A520 (§ 2.5.2; Wang et al. 2016). There, it was aligned with an apparent direction of a secondary sub-cluster merger. An intriguing possibility is that these channels are examples of a plasma depletion layer (PDL) — a feature observed when the magnetic field gets stretched and amplified to values where its energy density becomes comparable to thermal pressure of its host plasma. This happens, for example, when the solar wind drapes around a planetary magnetosphere, gets amplified and squeezes the plasma out from the narrow layer around the obstacle (Øieroset et al. 2004). A flow of magnetized plasma around a cluster cool core was simulated, e.g., by Dursi & Pfrommer (2008), and a similar draping phenomenon was predicted. While they used a uniform magnetic field in the gas flow, a tangled field, more representative of clusters, produces a similar end result (ZuHone et al. 2013). While cold fronts are obvious locations for PDL, sheets and filaments of significantly amplified field can emerge in other locations with coherent gas flows. ZuHone et al. (2011) presented MHD simulations of a sloshing core and traced the evolution of the magnetic fields. In their Figure 23, there is a particularly illuminating example of a plasma depletion phenomenon. A filament of an amplified magnetic field aligned with the cold front, but located at a distance from it, is in pressure equilibrium with the surrounding gas, but because the pressure contribution from the amplified magnetic field is significant

(30% of thermal pressure — compared to the usual  $\sim 1\%$ ), its thermal pressure is reduced by that amount essentially by squeezing the gas from the filament. This would produce an X-ray feature just like the channel we see aligned with the cold front in A2142. Our channel is located well within the sloshing region delineated by the NW cold front, and coherent gas flows are easily expected throughout this region. A possibly similar feature, though seen as an enhancement rather than a depression in X-ray brightness, was reported near the cold front in the Virgo core (Werner et al. 2016a).

The existence of such layers of draped magnetic fields around cold fronts have long been proposed to explain the suppressed thermal conduction and diffusion across the front and the front stability (Ettori & Fabian 2000; Vikhlinin et al. 2001a; Markevitch & Vikhlinin 2007). The KHIs at the southern front (§ 4.4) allowed us to evaluate the *effective* ICM viscosity. If the layer that we see in A2142 indeed has an amplified and ordered field and wraps around the southern front, it is the likely underlying physical mechanism that regulates the growth of those KHIs and determines that effective viscosity.

## 4.6 Summary

A2142 provides a laboratory to study several interesting effects in the intracluster plasma and in cluster cool cores. It exhibits four cold fronts — three in the core (two of which were the initial discovery of cold fronts in M00) and one 1 Mpc from the center, indicating long-lived sloshing set off by a strong disturbance from a merger. In this work, we have studied the three inner fronts using a 200 ks *Chandra* dataset. For the southern front, we estimate the velocity of the tangential gas flow inside the front from an estimate

of the centripetal acceleration and obtain  $v = 550 \pm 190$  km/s ( $M = 0.36 \pm 0.12$  w.r.t. the sound speed in the gas on the hotter side of the front). The southern front is clearly disrupted by Kelvin-Helmholtz instability, exhibiting two eddies separated by 55 kpc with an amplitude of 6–7 kpc. This is only the second reported example of the clearly observed KH eddies in the plane of the sky (the other one is A3667; other reports of the KHI were based on interpreting the structure in the front brightness profiles as eddies in projection). We compare the observed eddies with the numeric study of the growth of KHI in the context of cluster cold fronts by [R13](#), who included isotropic viscosity in their simulations. The A2142 eddies match the simulations if the isotropic, Spitzer-like viscosity is suppressed by a factor at least 5. The velocity of the gas flow is the biggest uncertainty in this estimate, but the viscosity has to be lower than Spitzer even if we assume a  $M = 1$  flow. From the numeric comparison of the effects of isotropic Spitzer viscosity and anisotropic Braginskii viscosity in the presence of gas sloshing and stretching of the magnetic fields ([ZuHone et al. 2015](#)), such a suppressed effective isotropic viscosity is consistent with full Braginskii anisotropic viscosity. Our viscosity constraints are in line with several recent results for other clusters based on the KHI at cold fronts ([Roediger et al. 2013a](#); [Su et al. 2017](#); [Ichinohe et al. 2017](#)) as well as on the observed details of gas stripping for an infalling galaxy ([Kraft et al. 2017](#)).

A2142 has a cool, dense peak, whose specific entropy index ( $K \approx 49$  keV cm<sup>2</sup>) makes it a rare “warm core,” an intermediate case between the cool cores with sharply peaked, low-entropy cores and non-cool-core clusters with flat cores. The peak is offset from the BCG by 30 kpc. Once the cool sloshing structure (that includes this peak, the inner cold front and the southern cold front) is approximately subtracted using wavelet

decomposition, we see that the larger-scale emission in the core is well-centered on the BCG, confirming the lensing result (Okabe & Umetsu 2008) that the BCG is at the center of the cluster gravitational potential. This is the largest observed offset between the cool peak and the center of the potential for any cluster that still exhibits a well-defined peak. The extreme sloshing in A2142 should have displaced the former cool core from the center of the potential, which facilitated its disruption, as simulated in ZuHone et al. (2010). The displaced peak expands, loses the stability provided by gravity, and becomes more susceptible to sloshing-induced mixing with the hotter gas. The BCG does not show a strong AGN (exhibiting only a very weak radio source) and there is no evidence for X-ray cavities, suggesting that the displaced peak has starved its nucleus of the accreting gas for a significant period.

Finally, we detect an intriguing “channel” in the X-ray brightness,  $>100$  kpc long,  $\sim 15$  kpc wide, with a  $\sim 10\%$  dip in brightness, that appears to be aligned with the southern cold front. It is similar to the channel we observed in A520 (§ 2.5.2; Wang et al. 2016) (though that channel is aligned with the axis of a secondary merger, not with a cold front). The channel should be a sheet of low-density gas seen edge-on. While some non-obvious 3D gas distributions cannot be excluded based on the X-ray image of this merging cluster, we think that a plausible explanation of this feature is a plasma depletion layer. In such a layer, the stretched and amplified magnetic field in the sloshing core may reach a pressure comparable with the thermal pressure of the gas, squeezing the gas from the layer. Such phenomena are observed when the solar wind flows around an obstacle, and also seen in simulations of sloshing cluster cores that include magnetic fields (ZuHone et al. 2011). Such channels may provide an interesting additional tool to

study the intracluster magnetic fields.

## CHAPTER 5

---

### Temperature maps of Abell 521, Abell 2319, and RX J1347

We present *Chandra* temperature maps of a further three clusters. The X-ray imaging and spectral analysis follow the same methods described in [Chapter 1](#).

#### 5.1 Abell 521

Abell 521 ( $z = 0.247$ ;  $1''$  is 3.89 kpc) is a  $T \simeq 6.2$  keV cluster undergoing a major merger. Its appearance suggests the merger taking place in the plane of the sky approximately along the NW-SE direction, which is supported by dynamical analysis of member galaxies ([Ferrari et al. 2003](#)). The cluster hosts a radio relic to the southeast, which is coincident with an X-ray surface brightness edge and is a shock front ([Giacintucci et al. 2008](#); [Bourdin et al. 2013](#)), while a radio halo can be seen in lower frequency radio observations ([Brunetti et al. 2008](#)).

We analyzed four archival *Chandra* data sets (ObsIDs 430, 901, PI: Arnaud; 12880, 13190, PI: Markevitch) that have a total exposure of 146 ks on the cluster after cleaning for background flare (88% useful). The soft band X-ray image and temperature map with

radio contour overlay are shown in [Fig. 5.1](#). Point sources were left in the X-ray image as a visual guide to *Chandra*'s spatial resolution compared to the features being discussed.

A schematic diagram of the merger is shown in Figure 6 of [Bourdin et al. \(2013\)](#) (reproduced in [Fig. 5.1](#)), illustrating how two subclusters (centered on the cD galaxies marked in [Fig. 5.1](#)) are pushing into each other, with a region of shock heated gas between them. Our *Chandra* temperature map is qualitatively in agreement with the map derived from XMM-Newton data in [Bourdin et al. \(2013\)](#). It shows clearly the surviving cool core of the northern subcluster, while the southern subcluster's original core gas shows as a mixture of hot and cool regions and may be in the process of being broken up. The band of hot gas between the two extends outward roughly perpendicular to the merger axis.

[Bourdin et al. \(2013\)](#) noted that the spatial distribution of the radio halo and shock heated gas appear correlated. We draw attention to the western extension of the shocked heated region, which leads to a curved surface brightness edge (its outline is pointed to by the three arrows in [Fig. 5.1](#)). The northern portion has the highest contrast and was noted by [Ferrari et al. \(2006\)](#) in earlier *Chandra* data sets, who described this segment as an arc-like discontinuity (in their Figure 1). The addition of the later observations (ObsIDs 12880, 13190) doubles the exposure time and hints at this discontinuity continuing further forming a round feature resembling the outline of a bubble. This is an interesting suggestion because the radio halo also fills this region, so it could well be an expanding bubble of shock heated gas embedded with ultra-relativistic electrons accelerated by the shock. We are unable to constrain from the current data set — which may be feasible with better signal-to-noise in this feature, given its likely hemispherical geometry — a model of the density and temperature profile of gas here. If the bubble's expansion into

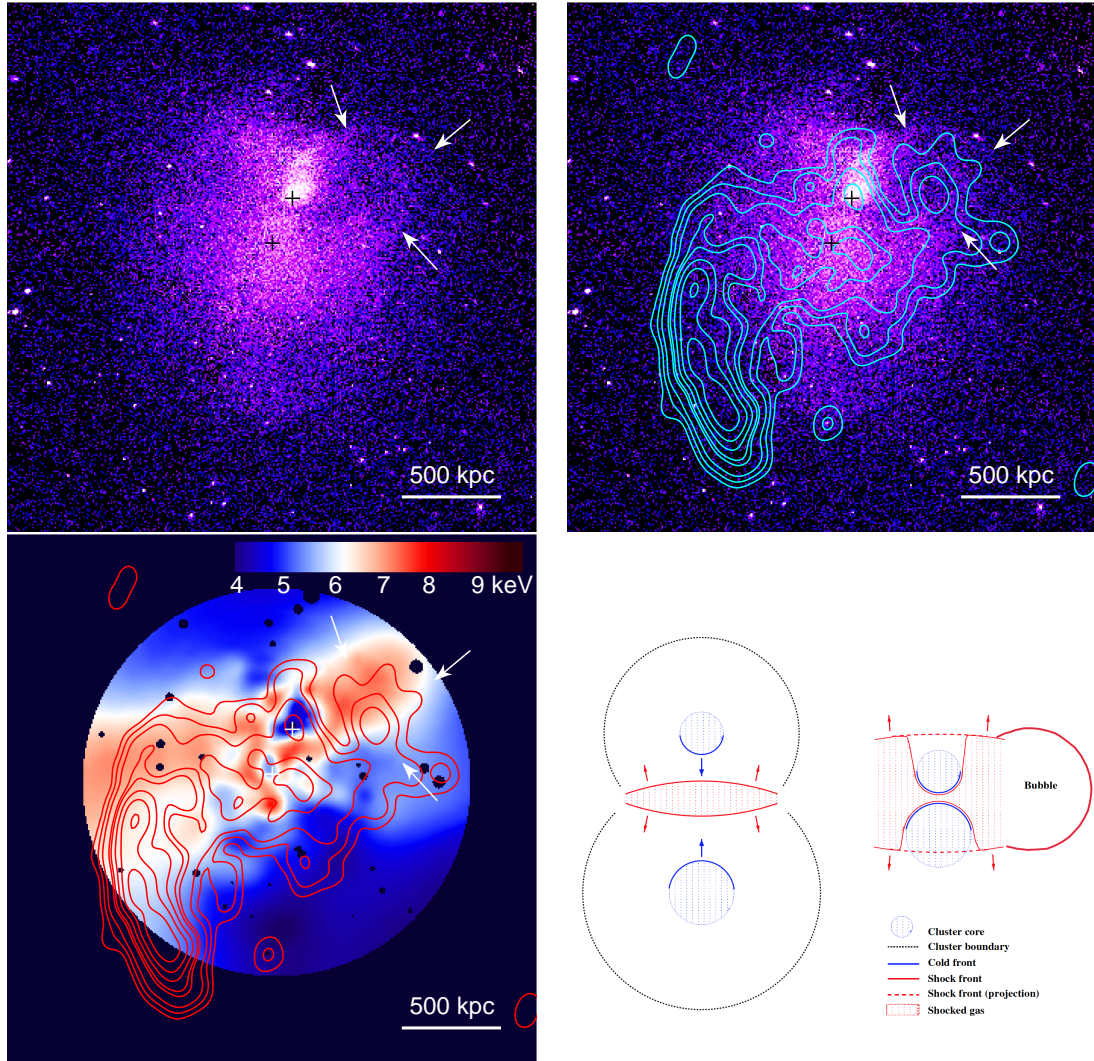


Figure 5.1: Abell 521. (*Upper left*) *Chandra* 0.8–4 keV surface brightness binned to  $2''$  pixels, without smoothing or source removal. The crosses mark the positions of the cD galaxies of the two colliding subclusters. The arrows point to the outline of an X-ray excess with a bubble-like shape. (*Upper right*) Same *Chandra* X-ray image with 240 MHz GMRT radio contours overlaid (Brunetti et al. 2008). (*Lower left*) Variable width Gaussian smoothed temperature map with radio contours overlaid. (*Lower right*) Merger scenario explaining the distribution of shock heated gas in this merger (reproduced from Bourdin et al. 2013, Figure 6). The bubble feature, inserted by us into the diagram, could be the expansion of this hot gas into cooler unshocked gas (see text).

the surrounding gas is supersonic, it could present us with an additional sample of a shock surface that has a simple geometry and little overprojection of other gas.

## 5.2 Abell 2319

Abell 2319 ( $z = 0.056$ ;  $1''$  is 1.09 kpc) is a  $T \simeq 9$  keV cluster with a large scale sloshing cold front, and hosts a radio halo (e.g., [Feretti et al. 1997](#); [Govoni et al. 2004](#); [Farnsworth et al. 2013](#); [Storm et al. 2015](#)). Studies of the merger dynamics using cluster galaxies and ICM properties suggest two main subclusters engaged in a low Mach number merger with a significant component of the trajectory out of the plane of the sky ([Oegerle et al. 1995](#); [O’Hara et al. 2004](#); [Sugawara et al. 2009](#); [Yan et al. 2014](#)).

We analyzed two archival *Chandra* data sets (ObsID 3231, PI: Mohr; 15187, PI: Markevitch) that have a total exposure of 89 ks for the cluster center after cleaning for background flare (98% useful). The soft band X-ray image and the temperature map are shown in [Fig. 5.2](#). Point sources were left in the X-ray image as a visual guide to the spatial resolution, which is much finer than the ICM features we are interested in.

The temperature map shows a significant temperature change at the southern cold front coinciding neatly with the full length of the X-ray edge. It also suggests that the more fuzzy brightness edge north of the X-ray peak is also a cold front. The arrows in [Fig. 5.2](#) point to two notable features in the cold front. The left arrow points to a dim spot, approximately 50 kpc across, just behind the cold front, which appears in the temperature map to be a pocket of hotter gas. The right arrow points to the bend in the outline of the southern cold front, where the edge begins to blur, and a waviness is present. The

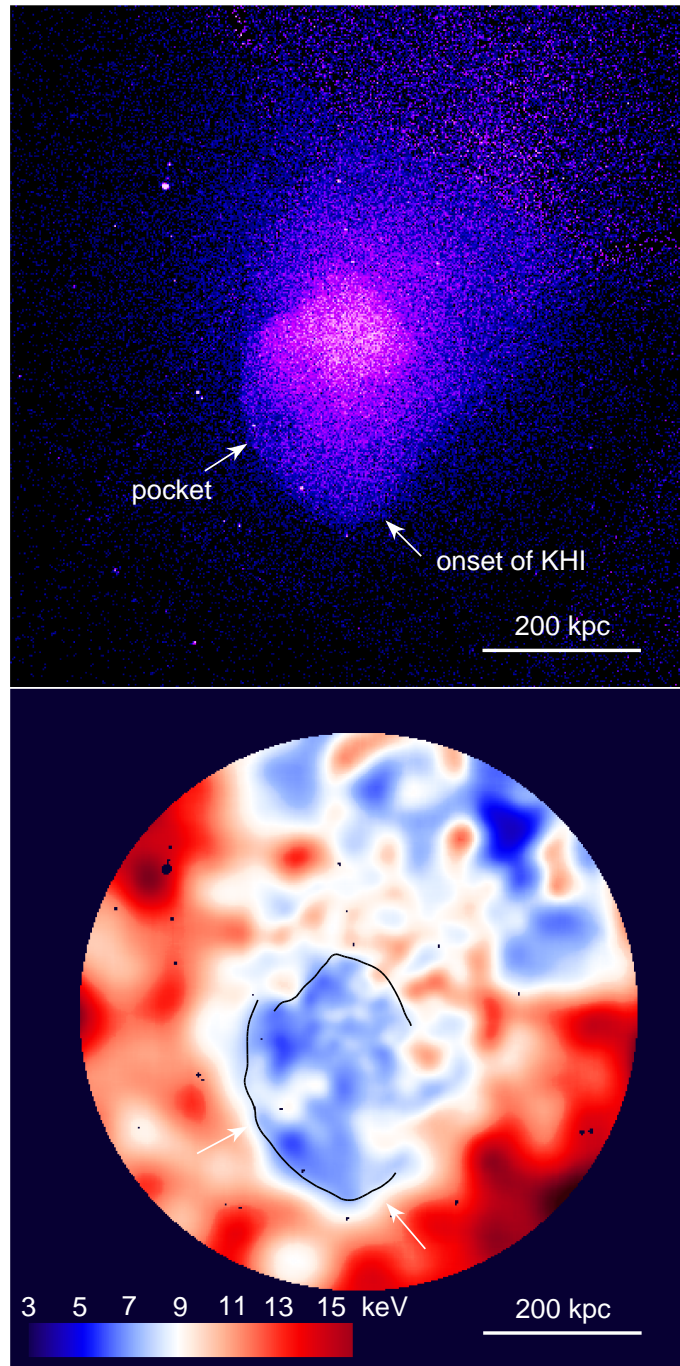


Figure 5.2: Abell 2319. (*Upper*) *Chandra* 0.5–4 keV surface brightness binned to 2'' pixels, without smoothing or source removal. (*Lower*) Variable width Gaussian smoothed temperature map. The black outlines of the two cold fronts are portions of X-ray surface brightness contours that trace them. The left arrow points to a pocket of hotter gas in the southern cold front; the right arrow points to the possible appearance of Kelvin-Helmholtz instabilities in the plane of the sky (see text).

temperature map shows a few alternating strips of hotter and cooler gas here. The signal-to-noise is insufficient to go further with a quantitative analysis, but future observations may wish to investigate this, as it is the most promising location to find KH instabilities in the plane of the sky, similar in position relative to the cold front as in A3667 and A2142. The KH instabilities in A2319 would be at a late stage, with the front going from being sharp to being completely disrupted.

### 5.3 RX J1347

RX J1347.5-1145 ( $z = 0.451$ ;  $1''$  is 5.77 kpc) is a  $T \simeq 13.3$  keV cluster with a sloshing cold front, being one of the most massive galaxy clusters known, and one of the most X-ray luminous. It has been studied extensively in the radio, from which maps of the Sunyaev-Zeldovich (SZ) effect suggested an excess of overpressured hot gas coinciding with the X-ray overbrightness to the southeast of the cluster core (e.g., [Komatsu et al. 2001](#); [Pointecouteau et al. 2001](#); [Kitayama et al. 2004](#); [Mason et al. 2010](#); [Korngut et al. 2011](#)). This X-ray excess can be seen through the X-ray contours in [Fig. 5.3](#). The eastern cD galaxy, which has no X-ray counter part, is believed to have lost most of its gas from ram pressure stripping, and this is supported by the X-ray image after a spherical model has been subtracted showing a trail of cool gas south of the X-ray overbrightness (e.g., [Johnson et al. 2012](#); [Kreisch et al. 2016](#)). Strong lensing mass map is consistent with the main cluster halo centered on the western cD galaxy, and the second subcluster halo centered on the eastern cD galaxy ([Ueda et al. 2018](#)). [Di Mascolo et al. \(2018\)](#) showed that the southeastern X-ray excess is predominantly an isobaric perturbation, but with an

adiabatically compressed region at the leading part of the stripped gas — where the higher X-ray brightness extension is located. They also found that the overpressured region seen in the SZ map goes away if the global pressure profile is allowed to be ellipsoidal (rather than spherically symmetric in previous studies) and the center of the model is allowed to be offset from the X-ray center. In this case, the presence of shock-heated gas suggested by previous interpretations of the SZ feature would be unnecessary.

We analyzed four archival *Chandra* data sets (ObsIDs 3592, PI: van Speybroeck; 13516, PI: Murray; 13999, 14407, PI: Jones) with a total exposure of 215 ks after filtering for background flare (99% useful). We show the soft band X-ray image, temperature map, and a false-color composite HST image in [Fig. 5.3](#). There is only one apparent X-ray point source in the field of view shown (to the southeast of the cluster, excised from the temperature map). Our temperature map shows that the sloshing cold front coincides with a cool edge along its entire outline. At the southeastern X-ray excess, there are both hot and cool blobs (relative to the average temperature). This suggests that the higher X-ray brightness in this region may be explained by the presence of clumps of cool gas that has higher X-ray emissivity (hinted by the two quasi-linear structures) coexisting with heated gas. This excess emission region appears to be a remnant of a disrupted subcluster, with its cool, dense pieces mixed with a shock-heated gas.

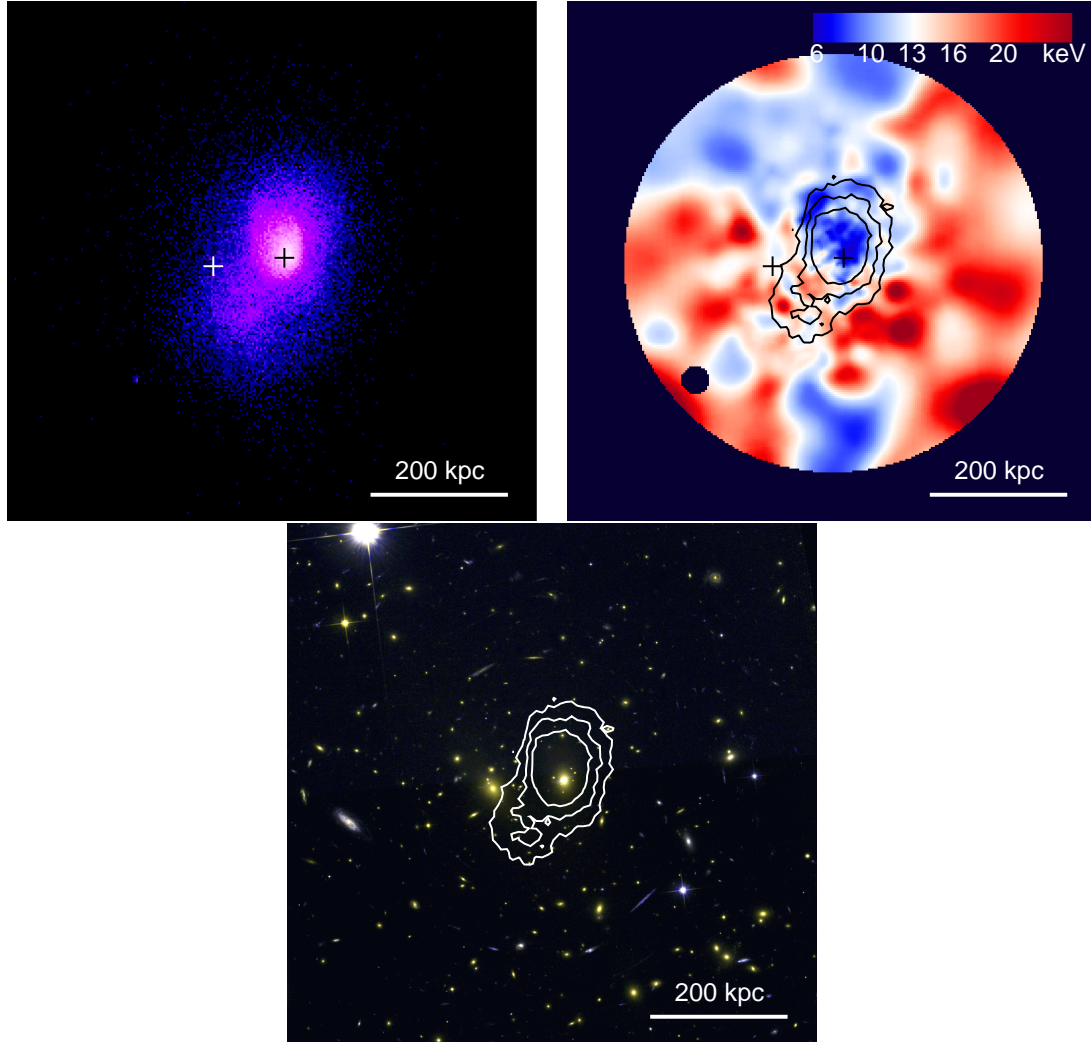


Figure 5.3: RX J1347. (*Upper left*) *Chandra* 0.8–4 keV surface brightness image (0.5'' per pixel), without smoothing or source removal. (*Upper right*) Variable width Gaussian smoothed temperature map. The black contours based on X-ray surface brightness trace the outline of the extended structure to the southeast of the X-ray center. The two crosses mark the positions of the cD galaxies as proxies for the center of mass of their subclusters. (*Lower*) False color image of HST images using the f475w and f814w filters (PI: Erben). X-ray contours are overlaid.

## CHAPTER 6

---

### Summary

In the preceding chapters, we have seen a demonstration of using galaxy clusters as an astrophysical laboratory to study the microphysical properties of the ICM.

In A520, we saw a unique evolutionary stage in a merger, just as the ram pressure stripped cool core remnant breaks from the shuttlecock shape that is seen in the Bullet cluster. We derived the specific entropy of the coolest part of the remnant and verified that it was a cool core. The twisted and elongated cool gas situated among hotter, shocked gas raises interesting questions about thermal conduction between the hot and cool regions. We showed that the structure appears to be insulated along the edge parallel to the elongation, as might be expected as a result of magnetic field being aligned with the edge and inhibiting conduction perpendicular to the field. However, conduction is possibly suppressed even along the stretch of cool core gas, based on an estimate of how long adjacent warm and cool pockets of gas have survived since the cool gas originated from the tip of the cool structure.

About 1.3 Mpc to the northeast of A520, we found what we believe to be a subcluster halo that had lost much of its original gas content after travelling through the central

region of A520. It then accreted gas near its present location in the outskirts. With only 1.5–3% X-ray measured gas mass to total (hydrostatic) mass, much lower than typical cluster average value, this clump is a “dark subcluster”. The presence of these low surface brightness subclusters in the outskirts affects the X-ray radial profile of the main cluster, but as we find, may also signal underestimated total mass when using X-ray surface brightness.

We then studied the bow shock of A520 in detail. It is one of only a handful of merger shocks with simple and unambiguous geometry, and a relatively high Mach number ( $M = 2.4_{-0.3}^{+0.4}$  at the nose). It shows the expected decline in Mach number away from the nose, as expected, where the shock front becomes oblique. Using the strongest segment of the shock at the nose, we performed a test to profile the thermal equilibration between protons that are heated at the shock, and electrons that are only adiabatically compressed at the shock. By calculating the downstream velocity, we could observe the time evolution of electron temperature unfurled spatially as the gas moves away from the shock. It appears that the electron temperature immediately jumps to the equilibrium post-shock temperature, at 95% confidence that it is above the expected temperature it would have from only adiabatic compression. This tantalizing result is similar to the one from the Bullet cluster, where the adiabatic compression only scenario was ruled out at 95% confidence. This suggests that other plasma interactions are prevalent and act on timescales much shorter than for Coulomb collisions.

A520 has a radio relic coincident with the shock surface in X-ray, powered by a population of synchrotron electrons that are believed to have been energized by the shock. It offers a test for the effectiveness of particle acceleration at cluster merger shocks.

Using VLA 1.4 GHz data, we tried to place an upper limit on the amount of pre-shock radio emission to see if the step jump in radio emissivity could be accounted for by the adiabatic compression of electrons and magnetic field. If the increase in radio emissivity could not be attributed to compression alone, then it would demonstrate the presence of particle acceleration at the shock, which is not yet well known. But for instrument artifacts, we were close to ruling out the scenario with only adiabatic compression. Our analysis showed that this interesting test is within reach, but requires observing it with better interferometric coverage and at lower frequencies, e.g., with GMRT or LOFAR.

In A2142, we focused on examining KHIs on its sloshing cold fronts. Both the northwest and southern cold fronts have features that are likely KHIs, but the southern cold front has two particularly striking KH eddies separated by 55 kpc with an amplitude of 6–7 kpc. We compared their appearance with KH eddies in simulations of interfaces with very similar properties, under isotropic Spitzer viscosity, and estimated that they match if the effective viscosity is no more than 1/5 Spitzer. This amount of suppressed effective isotropic viscosity is consistent with full Braginskii anisotropic viscosity. Our results here are in line with several recent results for other clusters also based on KHI at cold fronts.

We found curious X-ray channels in both A520 and A2142. In both cases, the depth of the dip in X-ray brightness, as well as the narrow and long shape, suggest a sheet geometry being seen on its side. An intriguing explanation for them is that they are plasma depletion sheets, where the magnetic field energy density is significantly increased and gas is squeezed out to maintain overall pressure balance. In A2142 in particular, the channel is found to the side of the southern cold front, but still within the sloshing gas of a

large cold front — these are conditions where magnetic field amplification has been seen in simulations. These channels may provide an additional tool to study the intracluster magnetic fields, if we can find more of them and demonstrate they are indeed PDLs.

In both A520 and A2142, we saw the displacement of cool gas from the center of the cluster gravitational potential and the BCG. In the context of AGN activity from the BCG, this may be showing us two different ways — ram pressure stripping and sloshing — mergers can deprive the AGN of cool gas.

All of the studies in this work require X-ray observing facilities with high spatial resolution, and large effective area for good counting statistics. Enlarging the samples of clusters will involve increasing the depth of already observed clusters, and most likely searching at higher redshifts. Future X-ray observatories with similar or better spatial resolution, and order of magnitude increase in collecting area, would no doubt lead to a step up in the number of high signal-to-noise observations, and expand the collection of intriguing but idiosyncratic objects to statistical samples.

---

## Bibliography

- Anders, E., & Grevesse, N. 1989, *Geochim. Cosmochim. Acta*, 53, 197
- Ascasibar, Y., & Markevitch, M. 2006, *ApJ*, 650, 102
- Bahcall, J. N., & Sarazin, C. L. 1977, *ApJ*, 213, L99
- Blandford, R., & Eichler, D. 1987, *Phys. Rep.*, 154, 1
- Bonafede, A., Feretti, L., Murgia, M., et al. 2010, *A&A*, 513, A30
- Bourdin, H., Mazzotta, P., Markevitch, M., Giacintucci, S., & Brunetti, G. 2013, *ApJ*, 764, 82
- Brunetti, G., & Jones, T. W. 2014, *International Journal of Modern Physics D*, 23, 30007
- Brunetti, G., Giacintucci, S., Cassano, R., et al. 2008, *Nature*, 455, 944
- Buote, D. A., Humphrey, P. J., & Stocke, J. T. 2005, *ApJ*, 630, 750
- Cassano, R., Ettori, S., Brunetti, G., et al. 2013, *ApJ*, 777, 141
- Cavagnolo, K. W., Donahue, M., Voit, G. M., & Sun, M. 2009, *ApJS*, 182, 12
- Churazov, E., Forman, W., Jones, C., & Böhringer, H. 2003, *ApJ*, 590, 225
- Clarke, T. E., Blanton, E. L., & Sarazin, C. L. 2004, *ApJ*, 616, 178
- Clarke, T. E., & Ensslin, T. A. 2006, *AJ*, 131, 2900
- Clowe, D., Bradač, M., Gonzalez, A. H., et al. 2006, *ApJ*, 648, L109
- Clowe, D., Markevitch, M., Bradač, M., et al. 2012, *ApJ*, 758, 128
- Dasadia, S., Sun, M., Sarazin, C., et al. 2016a, *ApJ*, 820, L20
- Dasadia, S., Sun, M., Morandi, A., et al. 2016b, *MNRAS*, 458, 681
- Di Mascolo, L., Churazov, E., & Mroczkowski, T. 2018, arXiv e-prints, arXiv:1812.01034
- Dupke, R., White, III, R. E., & Bregman, J. N. 2007, *ApJ*, 671, 181
- Dursi, L. J., & Pfrommer, C. 2008, *ApJ*, 677, 993
- Eckert, D., Vazza, F., Ettori, S., et al. 2012, *A&A*, 541, A57
- Ettori, S., & Fabian, A. C. 2000, *MNRAS*, 317, L57
- Ettori, S., Gastaldello, F., Gitti, M., et al. 2013, *A&A*, 555, A93
- Fabian, A. C., Celotti, A., Blundell, K. M., Kassim, N. E., & Perley, R. A. 2002, *MNRAS*, 331, 369
- Fabian, A. C., & Daines, S. J. 1991, *MNRAS*, 252, 17P
- Farnsworth, D., Rudnick, L., Brown, S., & Brunetti, G. 2013, *ApJ*, 779, 189
- Feretti, L., Giovannini, G., & Böhringer, H. 1997, *New A*, 2, 501
- Feretti, L., Giovannini, G., Govoni, F., & Murgia, M. 2012, *A&A Rev.*, 20, 54

Ferrari, C., Arnaud, M., Etori, S., Maurogordato, S., & Rho, J. 2006, *A&A*, 446, 417  
 Ferrari, C., Maurogordato, S., Cappi, A., & Benoist, C. 2003, *A&A*, 399, 813  
 Forman, W., Kellogg, E., Gursky, H., Tananbaum, H., & Giacconi, R. 1972, *ApJ*, 178, 309  
 Fox, D. C., & Loeb, A. 1997, *ApJ*, 491, 459  
 Gaspari, M., & Churazov, E. 2013, *A&A*, 559, A78  
 Ghavamian, P., Laming, J. M., & Rakowski, C. E. 2007, *ApJ*, 654, L69  
 Ghizzardi, S., Rossetti, M., & Molendi, S. 2010, *A&A*, 516, A32  
 Giacintucci, S., Markevitch, M., Brunetti, G., et al. 2014, *ApJ*, 795, 73  
 Giacintucci, S., Markevitch, M., Cassano, R., et al. 2017, *ApJ*, 841, 71  
 Giacintucci, S., Venturi, T., Macario, G., et al. 2008, *A&A*, 486, 347  
 Ginzburg, V. L., & Syrovatskii, S. I. 1964, *The Origin of Cosmic Rays*  
 Govoni, F., Feretti, L., Giovannini, G., et al. 2001, *A&A*, 376, 803  
 Govoni, F., Markevitch, M., Vikhlinin, A., et al. 2004, *ApJ*, 605, 695  
 Grebenev, S. A., Forman, W., Jones, C., & Murray, S. 1995, *ApJ*, 445, 607  
 Gursky, H., Kellogg, E., Murray, S., et al. 1971, *ApJ*, 167, L81  
 Hallman, E. J., & Markevitch, M. 2004, *ApJ*, 610, L81  
 Hamer, S. L., Edge, A. C., Swinbank, A. M., et al. 2012, *MNRAS*, 421, 3409  
 Hickox, R. C., & Markevitch, M. 2006, *ApJ*, 645, 95  
 Hitomi Collaboration, Aharonian, F., Akamatsu, H., et al. 2018, *PASJ*, 70, 9  
 Hull, A. J., Scudder, J. D., Larson, D. E., & Lin, R. 2001, *J. Geophys. Res.*, 106, 15711  
 Ichinohe, Y., Simionescu, A., Werner, N., & Takahashi, T. 2017, *MNRAS*, 467, 3662  
 Jee, M. J., Hoekstra, H., Mahdavi, A., & Babul, A. 2014, *ApJ*, 783, 78  
 Jee, M. J., Mahdavi, A., Hoekstra, H., et al. 2012, *ApJ*, 747, 96  
 Johnson, R. 2011, PhD thesis, Dartmouth College  
 Johnson, R. E., Zuhone, J., Jones, C., Forman, W. R., & Markevitch, M. 2012, *ApJ*, 751, 95  
 Kalberla, P. M. W., Burton, W. B., Hartmann, D., et al. 2005, *A&A*, 440, 775  
 Kellogg, E., Gursky, H., Tananbaum, H., Giacconi, R., & Pounds, K. 1972, *ApJ*, 174, L65  
 Keshet, U., Markevitch, M., Birnboim, Y., & Loeb, A. 2010, *ApJ*, 719, L74  
 Kitayama, T., Komatsu, E., Ota, N., et al. 2004, *PASJ*, 56, 17  
 Komatsu, E., Matsuo, H., Kitayama, T., et al. 2001, *PASJ*, 53, 57  
 Korngut, P. M., Dicker, S. R., Reese, E. D., et al. 2011, *ApJ*, 734, 10  
 Kraft, R. P., Roediger, E., Machacek, M., et al. 2017, *ApJ*, 848, 27  
 Kreisch, C. D., Machacek, M. E., Jones, C., & Randall, S. W. 2016, *ApJ*, 830, 39  
 Landau, L. D., & Lifshitz, E. M. 1959, *Fluid mechanics*  
 Lyutikov, M. 2006, *MNRAS*, 373, 73  
 Macario, G., Markevitch, M., Giacintucci, S., et al. 2011, *ApJ*, 728, 82  
 Machacek, M., Dosaj, A., Forman, W., et al. 2005, *ApJ*, 621, 663  
 Mahdavi, A., Hoekstra, H., Babul, A., Balam, D. D., & Capak, P. L. 2007, *ApJ*, 668, 806  
 Markevitch, M. 2006, in *ESA Special Publication*, Vol. 604, *The X-ray Universe 2005*,

- ed. A. Wilson, 723
- Markevitch, M. 2012, in Twelfth Marcel Grossmann Meeting on General Relativity, ed. A. H. Chamseddine, 397–410 (arXiv:1010.3660)
- Markevitch, M., Gonzalez, A. H., David, L., et al. 2002, *ApJ*, 567, L27
- Markevitch, M., Govoni, F., Brunetti, G., & Jerius, D. 2005, *ApJ*, 627, 733
- Markevitch, M., Mushotzky, R., Inoue, H., et al. 1996, *ApJ*, 456, 437
- Markevitch, M., & Vikhlinin, A. 2007, *Phys. Rep.*, 443, 1
- Markevitch, M., Vikhlinin, A., & Mazzotta, P. 2001, *ApJ*, 562, L153
- Markevitch, M., Ponman, T. J., Nulsen, P. E. J., et al. 2000, *ApJ*, 541, 542
- Markevitch, M., Bautz, M. W., Biller, B., et al. 2003a, *ApJ*, 583, 70
- Markevitch, M., Mazzotta, P., Vikhlinin, A., et al. 2003b, *ApJ*, 586, L19
- Mason, B. S., Dicker, S. R., Korngut, P. M., et al. 2010, *ApJ*, 716, 739
- Mazzotta, P., Fusco-Femiano, R., & Vikhlinin, A. 2002, *ApJ*, 569, L31
- Mazzotta, P., Markevitch, M., Vikhlinin, A., et al. 2001, *ApJ*, 555, 205
- Mazzotta, P., Rasia, E., Moscardini, L., & Tormen, G. 2004, *MNRAS*, 354, 10
- McNamara, B. R., Wise, M., Nulsen, P. E. J., et al. 2000, *ApJ*, 534, L135
- Million, E. T., Allen, S. W., Werner, N., & Taylor, G. B. 2010, *MNRAS*, 405, 1624
- Oegerle, W. R., Hill, J. M., & Fitchett, M. J. 1995, *AJ*, 110, 32
- O’Hara, T. B., Mohr, J. J., & Guerrero, M. A. 2004, *ApJ*, 604, 604
- Øieroset, M., Mitchell, D. L., Phan, T. D., et al. 2004, *Space Sci. Rev.*, 111, 185
- Okabe, N., & Umetsu, K. 2008, *PASJ*, 60, 345
- Owers, M. S., Nulsen, P. E. J., Couch, W. J., & Markevitch, M. 2009, *ApJ*, 704, 1349
- Owers, M. S., Nulsen, P. E. J., Couch, W. J., et al. 2014, *ApJ*, 780, 163
- Perley, R. A., & Butler, B. J. 2013, *ApJS*, 204, 19
- Planck Collaboration, Ade, P. A. R., Aghanim, N., et al. 2013, *A&A*, 554, A140
- Pointecouteau, E., Giard, M., Benoit, A., et al. 2001, *ApJ*, 552, 42
- Press, W. H., & Schechter, P. 1974, *ApJ*, 187, 425
- Rees, M. J., Begelman, M. C., Blandford, R. D., & Phinney, E. S. 1982, *Nature*, 295, 17
- Roediger, E., Brüggem, M., Simionescu, A., et al. 2011, *MNRAS*, 413, 2057
- Roediger, E., Kraft, R. P., Forman, W. R., Nulsen, P. E. J., & Churazov, E. 2013a, *ApJ*, 764, 60
- Roediger, E., Kraft, R. P., Nulsen, P., et al. 2013b, *MNRAS*, 436, 1721
- Roediger, E., Lovisari, L., Dupke, R., et al. 2012, *MNRAS*, 420, 3632
- Rossetti, M., Eckert, D., De Grandi, S., et al. 2013, *A&A*, 556, A44
- Russell, H. R., Sanders, J. S., Fabian, A. C., et al. 2010, *MNRAS*, 406, 1721
- Russell, H. R., McNamara, B. R., Sanders, J. S., et al. 2012, *MNRAS*, 423, 236
- Russell, H. R., Fabian, A. C., McNamara, B. R., et al. 2014, *MNRAS*, 444, 629
- Sarazin, C. L. 1988, *X-ray emission from clusters of galaxies* (Cambridge: Cambridge University Press)
- Sarazin, C. L., Finoguenov, A., Wik, D. R., & Clarke, T. E. 2016, ArXiv e-prints, arXiv:1606.07433
- Sasaki, T., Matsushita, K., Sato, K., & Okabe, N. 2015, *ApJ*, 806, 123

- Schekochihin, A. A., Cowley, S. C., Kulsrud, R. M., Rosin, M. S., & Heinemann, T. 2008, *Physical Review Letters*, 100, 081301
- Shimwell, T. W., Brown, S., Feain, I. J., et al. 2014, *MNRAS*, 440, 2901
- Shimwell, T. W., Markevitch, M., Brown, S., et al. 2015, *MNRAS*, 449, 1486
- Simionescu, A., Werner, N., Forman, W. R., et al. 2010, *MNRAS*, 405, 91
- Simionescu, A., Werner, N., Urban, O., et al. 2012, *ApJ*, 757, 182
- Slezak, E., Durret, F., & Gerbal, D. 1994, *AJ*, 108, 1996
- Spitzer, L. 1956, *Physics of Fully Ionized Gases*
- . 1962, *Physics of Fully Ionized Gases*
- Springel, V., Frenk, C. S., & White, S. D. M. 2006, *Nature*, 440, 1137
- Starck, J.-L., & Murtagh, F. 1994, *A&A*, 288, 342
- Storm, E., Jeltema, T. E., & Rudnick, L. 2015, *MNRAS*, 448, 2495
- Su, Y., Kraft, R. P., Roediger, E., et al. 2017, *ApJ*, 834, 74
- Sugawara, C., Takizawa, M., & Nakazawa, K. 2009, *PASJ*, 61, 1293
- Takizawa, M. 1999, *ApJ*, 520, 514
- Tittley, E. R., & Henriksen, M. 2005, *ApJ*, 618, 227
- Ueda, S., Kitayama, T., Oguri, M., et al. 2018, *ApJ*, 866, 48
- Vacca, V., Feretti, L., Giovannini, G., et al. 2014, *A&A*, 561, A52
- van Weeren, R. J., Röttgering, H. J. A., Brüggén, M., & Hoeft, M. 2010, *Science*, 330, 347
- Venturi, T., Rossetti, M., Brunetti, G., et al. 2017, *A&A*, 603, A125
- Vikhlinin, A. 2011, in *Structure in Clusters and Groups of Galaxies in the Chandra Era*, ed. J. Vrtilik & P. J. Green, 53
- Vikhlinin, A., Forman, W., & Jones, C. 1994, *ApJ*, 435, 162
- Vikhlinin, A., Kravtsov, A., Forman, W., et al. 2006, *ApJ*, 640, 691
- Vikhlinin, A., Markevitch, M., & Murray, S. S. 2001a, *ApJ*, 551, 160
- . 2001b, *ApJ*, 549, L47
- Vikhlinin, A., Markevitch, M., Murray, S. S., et al. 2005, *ApJ*, 628, 655
- Vikhlinin, A., McNamara, B. R., Forman, W., et al. 1998, *ApJ*, 502, 558
- Walker, S. A., Hlavacek-Larrondo, J., Gendron-Marsolais, M., et al. 2017, *MNRAS*, 468, 2506
- Walker, S. A., Sanders, J. S., & Fabian, A. C. 2016, *MNRAS*, 461, 684
- Wang, Q. H. S., Giacintucci, S., & Markevitch, M. 2018, *ApJ*, 856, 162
- Wang, Q. H. S., & Markevitch, M. 2018, *ApJ*, 868, 45
- Wang, Q. H. S., Markevitch, M., & Giacintucci, S. 2016, *ApJ*, 833, 99
- Werner, N., ZuHone, J. A., Zhuravleva, I., et al. 2016a, *MNRAS*, 455, 846
- Werner, N., Zhuravleva, I., Canning, R. E. A., et al. 2016b, *MNRAS*, 460, 2752
- Westphal, J. A., Kristian, J., & Sandage, A. 1975, *ApJ*, 197, L95
- Willingale, R., Starling, R. L. C., Beardmore, A. P., Tanvir, N. R., & O'Brien, P. T. 2013, *MNRAS*, 431, 394
- Wong, K.-W., & Sarazin, C. L. 2009, *ApJ*, 707, 1141
- Yan, P.-F., Yuan, Q.-R., Zhang, L., & Zhou, X. 2014, *AJ*, 147, 106

- Zeldovich, Y. B., & Raizer, Y. P. 1966, Elements of gasdynamics and the classical theory of shock waves
- ZuHone, J. A., Kunz, M. W., Markevitch, M., Stone, J. M., & Biffi, V. 2015, ApJ, 798, 90
- ZuHone, J. A., Markevitch, M., Brunetti, G., & Giacintucci, S. 2013, ApJ, 762, 78
- ZuHone, J. A., Markevitch, M., & Johnson, R. E. 2010, ApJ, 717, 908
- ZuHone, J. A., Markevitch, M., & Lee, D. 2011, ApJ, 743, 16